UCRL-16274

University of California

Ernest O. Lawrence Radiation Laboratory

K^--PROTON ELASTIC SCATTERING IN THE MOMENTUM RANGE 700 TO 1400 MeV/c

Berkeley, California

DISCLAIMER

Special Thesis

UCRL-16274

UNIVERSITY OF CALIFORNIA

Lawrence Radiation Laboratory
Berkeley, California

AEC Contract No. W-7405-eng-48

K^--PROTON ELASTIC SCATTERING IN THE MOMENTUM RANGE 700 TO 1400 MeV/c

William R. Holley
(Thesis)

October 22, 1965

K^--PROTON ELASTIC SCATTERING IN THE MOMENTUM RANGE 700 TO 1400 MeV/c

Contents

K^--PROTON ELASTIC SCATTERING IN THE MOMENTUM RANGE 700 TO 1400 MeV/c

William R. Holley

Lawrence Radiation Laboratory
University of California
Berkeley, California

October 22, 1965

ABSTRACT

Differential cross sections for elastic K^--p scattering have been measured at incident-kaon momenta from 700 to 1400 MeV/c. A total of 17 000 elastic events were observed with narrow-gap cylindrical and parallel-plate spark chambers.

Least-squares fits of Legendre-polynomial power series to the differential cross sections require fifth-order terms in the region of the suggested 1765- and 1815-MeV resonances. Sixth-order coefficients are not required.

The behavior of the coefficients requires a highly elastic resonance near 1815 MeV and is consistent with the existence of an additional enhancement near 1765 MeV. The latter resonance, if it exists, is rather inelastic.

Least-squares fits of one or more Breit-Wigner resonance terms with constant backgrounds to the total elastic and total cross sections and a qualitative analysis of the Legendre-polynomial coefficients favor a $J = 5/2$ assignment for the 1815-MeV resonance, although $J = 3/2$ cannot be completely excluded.

I. INTRODUCTION

Early K^--p total-cross-section measurements gave little evidence of structure in the $\bar{K}$-N interaction.[1] At low momenta (below a few hundred MeV/c) the total cross section appears to follow a 1/v law. Dalitz and Tuan have described this dependence, using S-wave complex scattering lengths.[2] Later measurements at higher energies, however, have indicated the presence of several resonances in the $\bar{K}$-N system. Tripp, Ferro-Luzzi, and Watson have discussed rather completely an isotopic spin $T = 0$, $D_{3/2}$ resonance of low elasticity at 394 MeV/c (corresponding to 1520 MeV total energy in the center-of-mass system).[3] Another highly inelastic resonance, at 740 MeV/c (1660 MeV), has been observed in the $T = 1$ channel and also appears to have total angular momentum $J = 3/2$.[4] The parity of this resonance is not clear at present.

More extensive and accurate total-cross-section measurements have indicated the presence of a rather large enhancement in the K^--p total cross section (a 15-mb bump on top of a 35-mb background) at an incident K^- momentum of 1050 MeV/c.[5] No appreciable corresponding peak in the K^--n total cross section is evident, leading to a $T = 0$ assignment for the bump. Unitarity arguments based on the size of the resonant peak in the K^--p total cross section indicate $J \geq 3/2$.[5b]

From a study of enhancements in the K^-p mass spectrum in the reaction $K^-n \rightarrow K^-p\pi^-$, the behavior of the K^-p and K^-n total cross sections,[5] and the results of elastic[4a, 6] and charge-exchange[6a, 7] scattering experiments, Barbaro-Galtieri, Hussain, and Tripp have concluded that the $\bar{K}$-N reaction in this neighborhood should be described in terms of two resonances, one with $T = 1$ at 1765 MeV, the other with $T = 0$ at 1815 MeV.[8] Tentative spin and parity assignments of $D_{5/2}$ for the 1765-MeV state and $F_{5/2}$ for the 1815-MeV state have been suggested.[8, 9]

The $F_{5/2}$ assignment for the $Y_0^*(1815)$ suggests that it is the Regge recurrence of the Λ. In this case it would fit in the "excited" spin-5/2 baryon octet of SU_3 symmetry.[10]

Ball and Frazer, using partial-wave dispersion relations,

have shown that inelastic threshold effects under certain conditions can produce large bumps in the elastic channels.[11] In an analysis of π-N scattering data, Auvil et al. have found enhancements in the elastic-scattering amplitude which seem to confirm the validity of the Ball-Frazer mechanism.[12] The threshold for production of $\bar{K}^*$ (888) in the reaction $\bar{K} + N \rightarrow \bar{K}^* + N$ is near the energy of the Y_0^* (1815), and Ball and Frazer have shown that their model could yield a substantial peak in the elastic $D_{3/2}$, $T = 0$ amplitude.

The purpose of the experiment described in this thesis was to explore in detail the elastic-scattering angular distributions of K^- mesons on protons in the momentum range 700 to 1400 MeV/c. Preliminary results were reported at the 1962 International Conference on High Energy Physics at CERN.[6c] In the experiment a liquid-hydrogen target and an array of spark chambers were used. The equipment and experimental procedures are described in the following Section II. In Section III data analysis and corrections to the data are discussed. Results of the experiment are presented in Section IV. Section V contains a discussion of the results and their relation to the various proposed resonances in the energy region covered by the experiment.

II. EXPERIMENTAL PROCEDURE AND EQUIPMENT

A. K^- Beam

Figure 1 shows the layout of the beam. Negative particles produced in the forward direction by collisions of the circulating proton beam of the Bevatron with an internal target were deflected by the Bevatron's magnetic field through a thin (0.020-in.) aluminum window in the vacuum tank at the upstream end of the west straight section. The "C" magnets M_1 and M_2 were placed close to the thin window of the Bevatron in order to subtend a solid angle as large as possible at the internal target. The combined effect of the Bevatron's magnetic field and M_1 and M_2 bent the beam through an angle of approximately 45 deg and served to define the primary-beam momentum. The beam was then focused by the 8-in. quadrupole doublet, Q_1, at B_1 located between the two high-pressure methane-gas Cerenkov counters. The effect of multiple Coulomb scattering in the Cerenkov counters on the final beam size at the hydrogen target was thus minimized. The second quadrupole, Q_2, focused the beam vertically at the hydrogen target and horizontally at infinity. The final bending magnet, M_3, served to define the final momentum of the beam, bending the central-momentum particles through an angle of 28 deg.

To achieve a high trigger rate the beam was designed to accept a rather wide momentum band ($\Delta P/P \approx \pm 6\%$); however, spark chambers B, placed on each side of M_3, allowed for the a posteriori determination of the momentum of an interacting beam particle to better than $\pm 1.0\%$. A helium-gas-filled bag occupying as much of the beam path as possible reduced beam loss and kept the final vertical beam size as small as possible by reducing multiple Coulomb scattering. The total path length of the beam from production target to hydrogen target was about 45 ft.

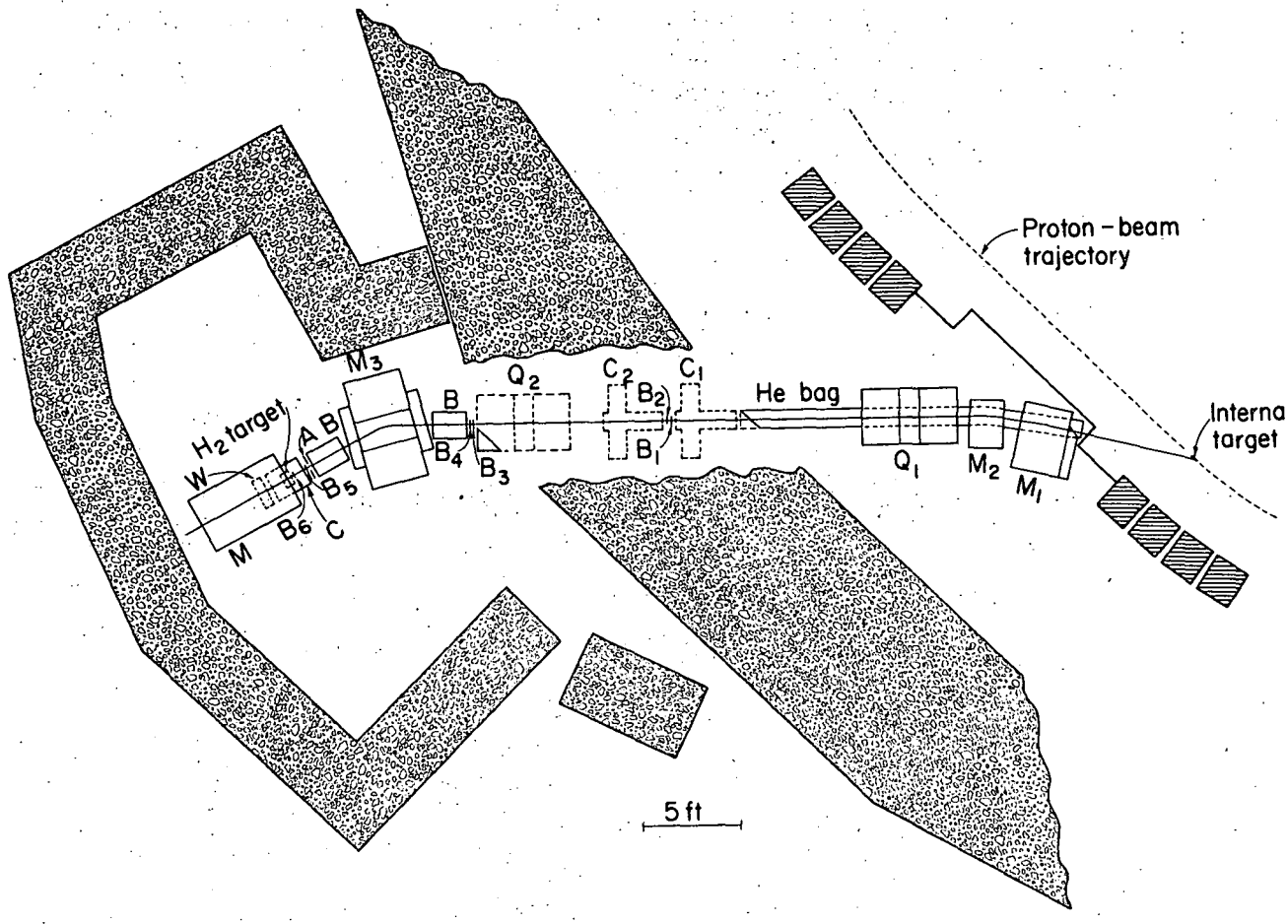

Fig. 1. Plan view of beam layout. M_1, M_2, and M_3 are analyzing magnets; Q_1 and Q_2 are quadrupole doublets; C_1 and C_2 are gas Cerenkov counters; W is a water Cerenkov counter; B_1 through B_6 and A are scintillation counters; and B, C, and M are spark chambers. MUB-4337

B. Hydrogen Target

A specially designed liquid-hydrogen target, shown in Fig. 2, was used to minimize the amount of hydrogen traversed by the elastic-scattered particles. The liquid-hydrogen flask was almost parallelopipedal in shape, with dimensions approximately 6 in. along the beam direction, 3 in. vertically and 15 in. transverse to the beam. This flask was enclosed in a cylindrical flask which was connected to the liquid-hydrogen boil-off vent line by four stainless steel tubes. The liquid-hydrogen inner flask was thus surrounded by hydrogen gas at essentially the same pressure as that of the liquid hydrogen. In this way the stress on the liquid-hydrogen flask was kept to a minimum, allowing it to retain its shape. The liquid-hydrogen flask was supported by one of the stainless steel hydrogen-gas feed tubes which ran along the bottom of the flask and connected to a stainless steel end plate. The inner flask was constructed of 0.003-in. mylar with stainless steel end plates and the outer flask of 0.010-in. mylar. A cylindrical aluminum vacuum jacket with 0.051-in. -thick walls surrounded the two hydrogen flasks.

C. Spark Chambers

The system for detecting elastic scatters in this experiment consisted of two momentum-defining parallel-plate spark chambers, a 10-gap cylindrical spark chamber surrounding the hydrogen target for observing the incoming K^- and the outgoing scattered particles, and a large semicylindrical spark chamber with carbon- and steel-plate absorbers between the plates for range and polarization measurements.[13] A picture of the momentum-analyzing magnet, M_3, and the spark-chamber arrangement is shown in Fig. 3. A detailed diagram of the elevation view of the spark chamber setup following M_3 is shown in Fig. 4.

The momentum-defining chambers consisted of two small

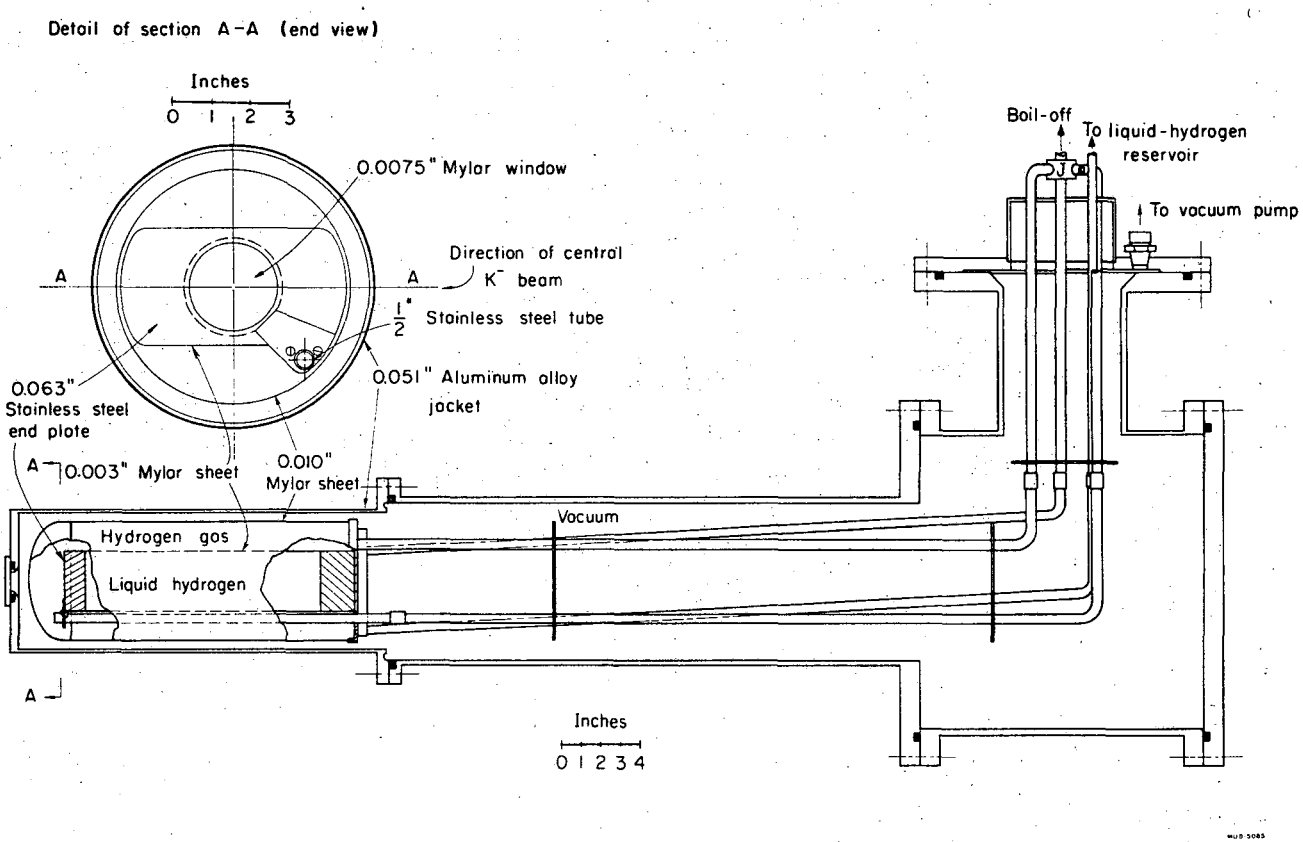

Fig. 2. Details of liquid-hydrogen target assembly.

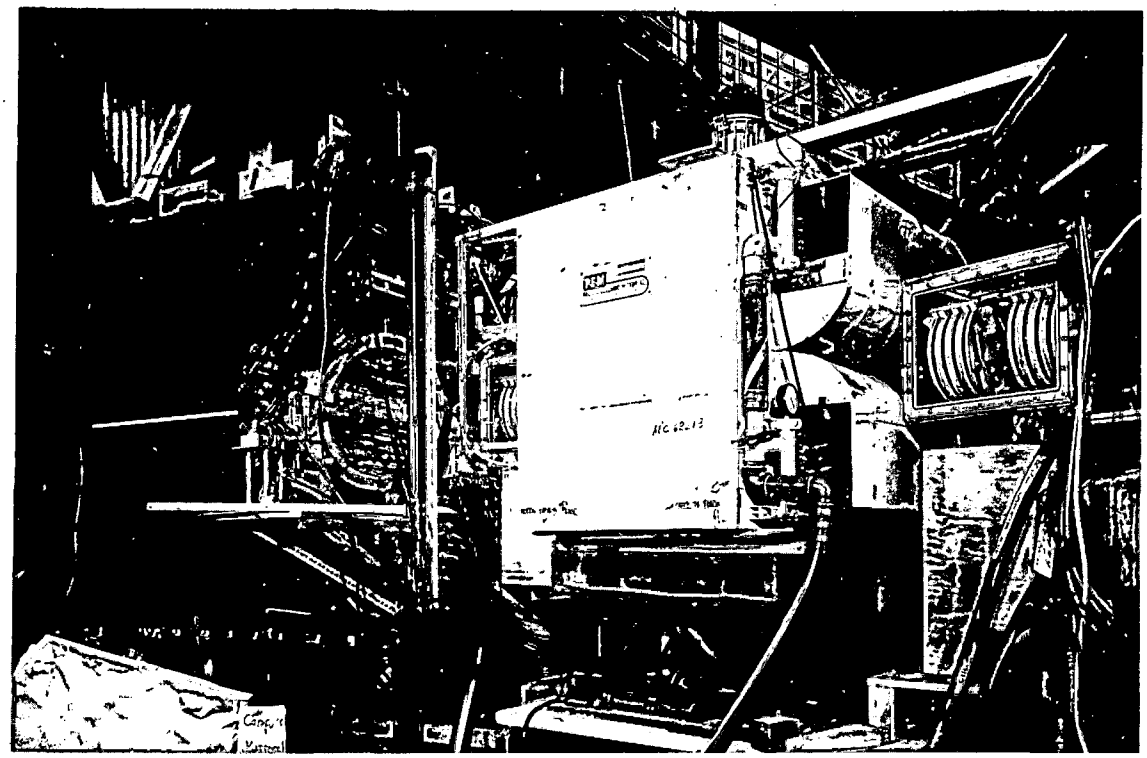

ZN-4894

Fig. 3. Nearly completed setup of the detection apparatus. The cylindrical chamber has been removed and a scintillation counter inserted for preliminary beam measurements.

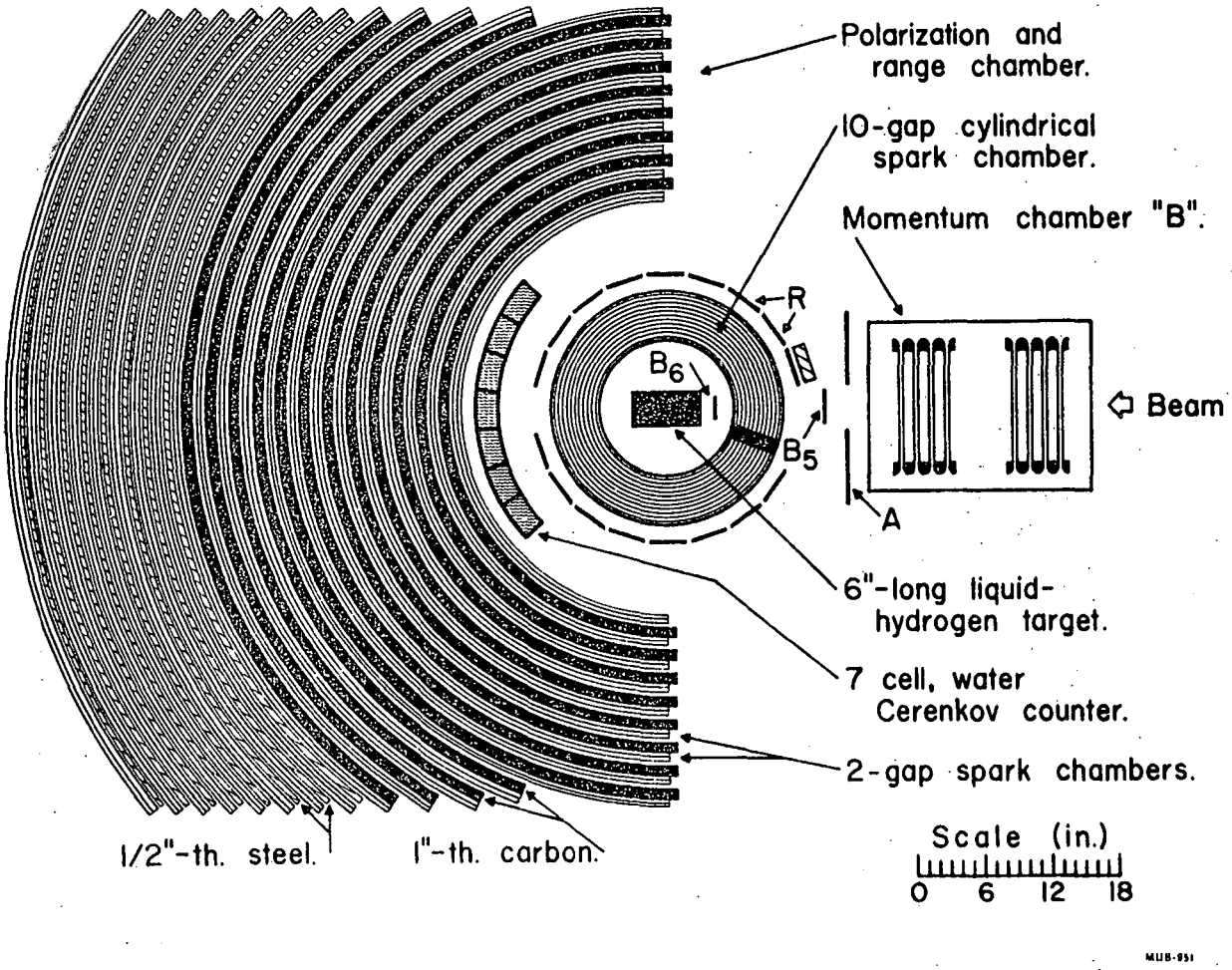

Fig. 4. Elevation view of the apparatus. The upstream momentum-defining chamber and the final bending magnet, M_3, are not shown.

8-gap parallel-plate spark chambers. The plates, of 0.003-in. aluminum, were 12-in.-diam discs with a gap spacing of 0.375 in. and were grouped into two 4-gap sections, 8 in. apart. An air-tight aluminum box with transparent Lucite viewing windows on the top and one side enclosed the plates. The entrance and exit windows of the box were constructed of 0.003-in. aluminum foil to minimize the amount of material in the beam.

The 10-gap cylindrical spark chamber[13] (Fig. 5) surrounding the hydrogen target was used to detect elastic scatters. The cylindrical construction of the spark chamber has several advantages. Since the interactions in the target occur near the center of the chamber, outgoing tracks tend to be radial and therefore traverse the gaps normal to the plates, yielding higher angular accuracy. This is true, of course, for angles in the elevation view (projections of track onto a plane normal to the cylinder axis). However, due to the stereo system used, depth and dip-angle resolution is about seven times worse (see Appendix) than resolution in the direct (elevation) view. Since most observed elastic scatters lie in planes having small dip angles, the poorer depth resolution does not seriously affect scattering-angle determination (see Section III. B. 3. d). Cylindrical geometry also makes it possible to obtain a large detection solid angle while using spark chambers of relatively small physical dimensions. In addition, the short flight paths for scattered K^- mesons from the target to the trigger counters surrounding the cylindrical chamber reduce the decay-in-flight correction.

The electrodes were constructed of 0.010-in. aluminum sheets rolled into cylinders 18 in. long and varying in diameter from 10 to 20 in. The ends of the cylinders were imbedded in concentric circular grooves machined in two polished Lucite end plates. The gap spacing was 0.375 in. The straight edges of the electrodes were imbedded in a grooved Lucite post stretching the length of the chamber. Electrical and gas connections to the chamber were made through this post.

In order to obtain range and polarization information on the recoil protons a large semicylindrical spark chamber was placed

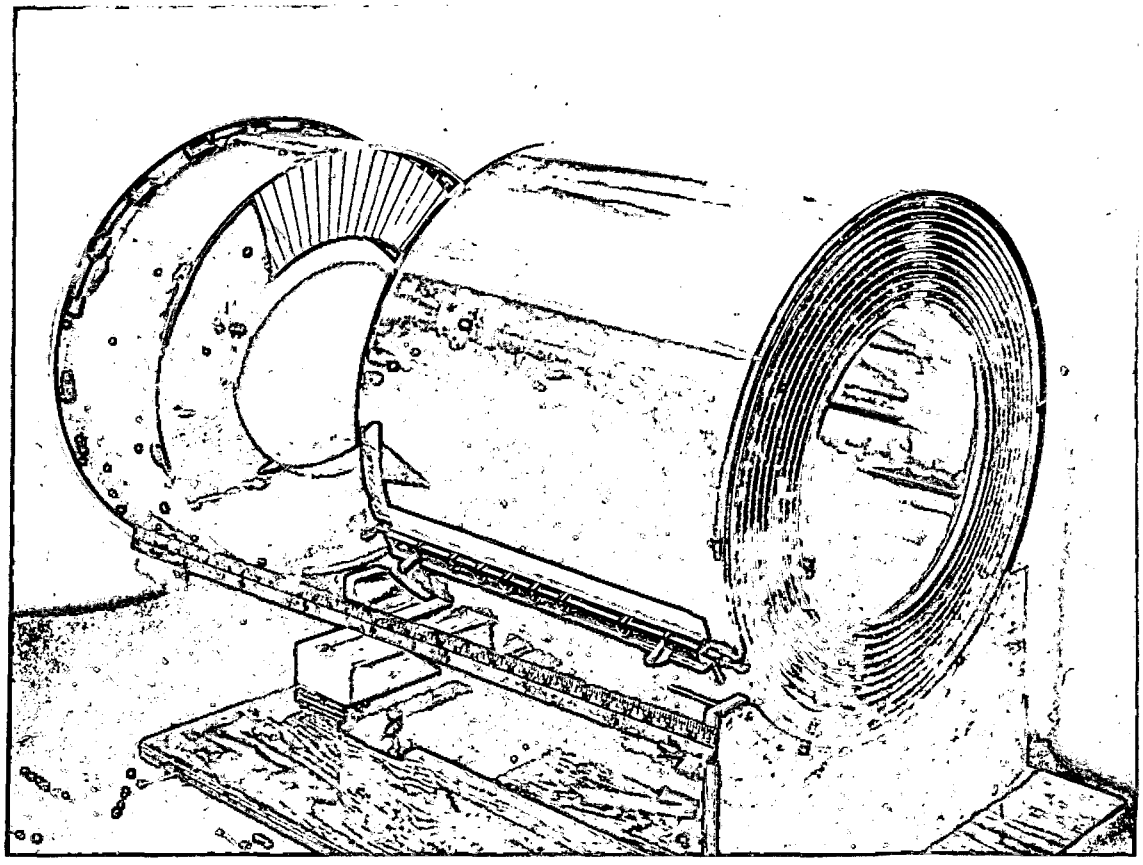

ZN-4895

Fig. 5. Cylindrical spark chamber and segmented stereo mirror

downstream of the cylindrical chamber. The spark chamber consisted of 21 concentric 2-gap chambers interleaved with absorbers - twelve 1-in. carbon absorbers at radii of 18 to 40 in. followed by nine curved 0.5-in. steel plates extending to a radius of 60 in. The transparent curved insulating edge supports for each spark-chamber cell were made from an annulus of polished Lucite in which three grooves were machined 0.375 in. apart. The whole range and polarization spark-chamber assembly measured 5 ft wide by 6 ft high by 3 ft deep and weighed about 6 tons.

The interelectrode gas used in the spark chambers was a mixture of 90% neon and 10% helium. Because of the presence of small gas leaks in the spark chambers, it was necessary to circulate continually the gas mixture through the chambers at a slight positive pressure.

Stereo information for the two beam chambers was provided by plane front-surfaced mirrors attached to the tops of the chambers. These mirrors were tipped at an angle of 45 deg to the horizontal and afforded a plan view of the chambers in addition to the direct side (elevation) view. Depth and dip-angle information for tracks in the cylindrical chamber was obtained by using an array of 72 tilted mirrors placed behind the chamber (see Fig. 5). The mirror segments were arranged almost radially on a circular 2-in.-thick Lucite backing plate. A series of slanting planes was carefully machined into the Lucite plate. The mirrors were then attached to the plate with double-sided masking tape. The backing plate was machined so that each mirror makes an angle of 5.7 deg to the plane normal to the axis of the cylinder. The mirrors are tipped in such a way that the reflected image is displaced counter clockwise from the actual spark. Details of the depth and dip-angle calculations are given in Sec. III. B. 2 and the Appendix. A similar segmented mirror system with elements tilted through an angle of 2.85 deg was used to give stereo information for tracks in the range-polarization semicylindrical chamber.

Photographing all spark chambers on a single frame of film required a rather complicated system of plane front-surfaced mirrors,

arranged as shown in Fig. 6. Hyperboloidal field lenses, machined from Lucite, with a focal length of 28 ft, were placed in front of each spark chamber. The full length of each gap could then be viewed with a camera positioned at the focal point of each lens.

Two stages of mirrors for each chamber were required in order to place the effective focal point of each lens at the same point in space and also to have the virtual images of the chambers, as seen by the camera, arranged to fit efficiently onto a single frame of film. Because of limitations on the size of Lucite blocks and lathes available, two lenses, and hence two separate mirror systems, were used on the large semicylindrical chamber.

Fiducial lines were scribed in 1/8-in.-thick Lucite sheets placed in front of each chamber and illuminated by xenon flash lamps. The xenon lamps were flashed by discharges from 8-μF capacitors at 14 kV, triggered by a spark gap.

Identification numbers (run number and Bevatron pulse number) and the cumulative number of incident kaons for that run were recorded on each picture by using "Nixie" lights.

A segmented seven-cell water Cerenkov counter running the length of the cylindrical chamber was used to detect particles with velocity $\gtrsim 0.75c$ entering the range polarization chamber. Neon lights placed adjacent to the water Cerenkov counter were used to identify on the film the particular compartment of the counter through which the high-velocity particle passed.

The camera used was a 35-mm Flight Research Model IV with a recovery (film-advance) time of approximately 40 msec. Thus as many as 10 pictures per beam pulse could be taken under optimum beam conditions (beam spill as long as 400 to 500 msec). Background-X film was used at a lens setting of f/14.

D. Electronics

The electronic flow diagram is shown in Fig. 7. The kaons in

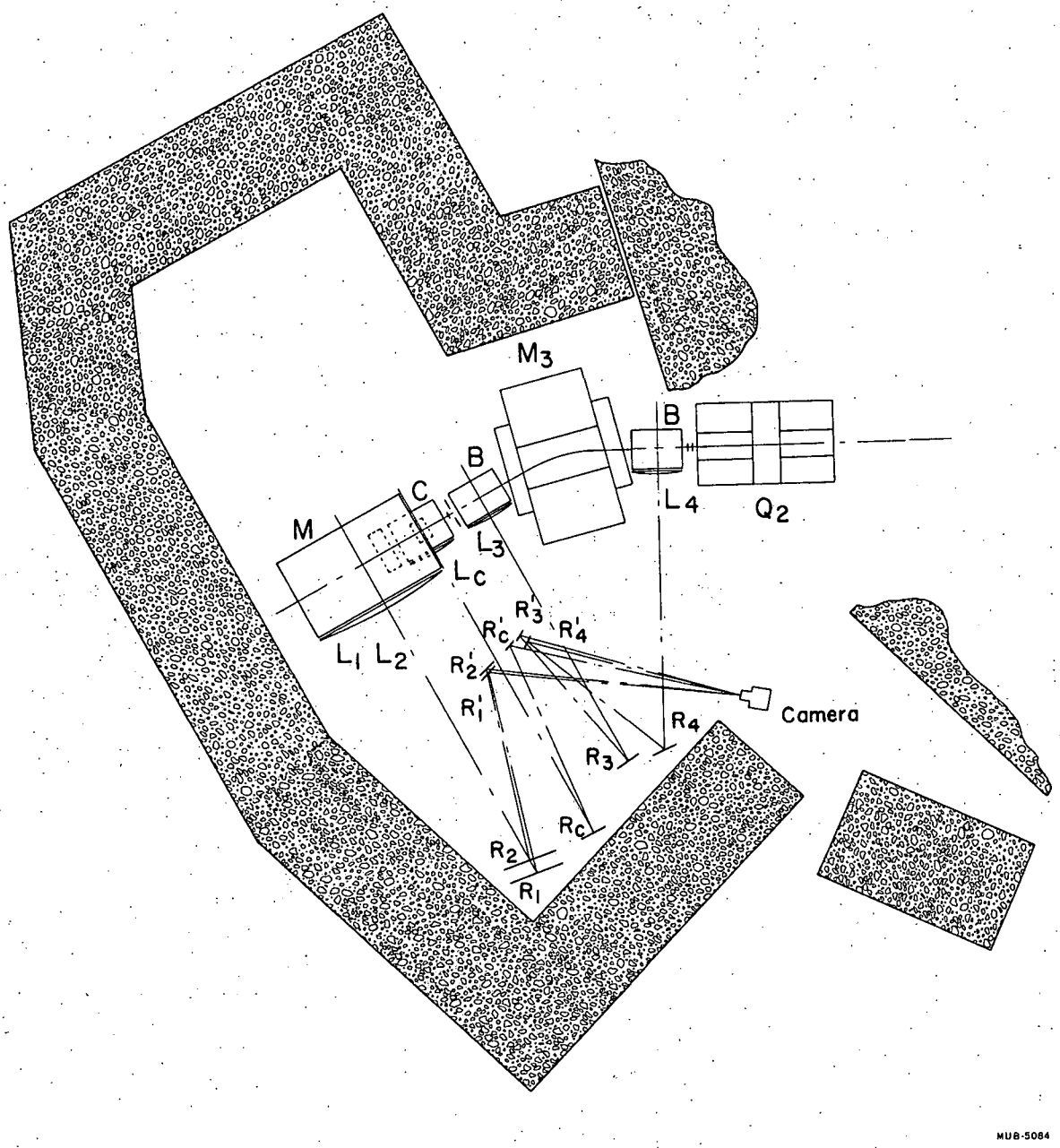

Fig. 6. Diagram of optical system used to photograph the events. Two stages of mirror reflections were used (R_1, R'_1, etc.); L_1, L_2, L_3, L_4, and L_c are field lenses

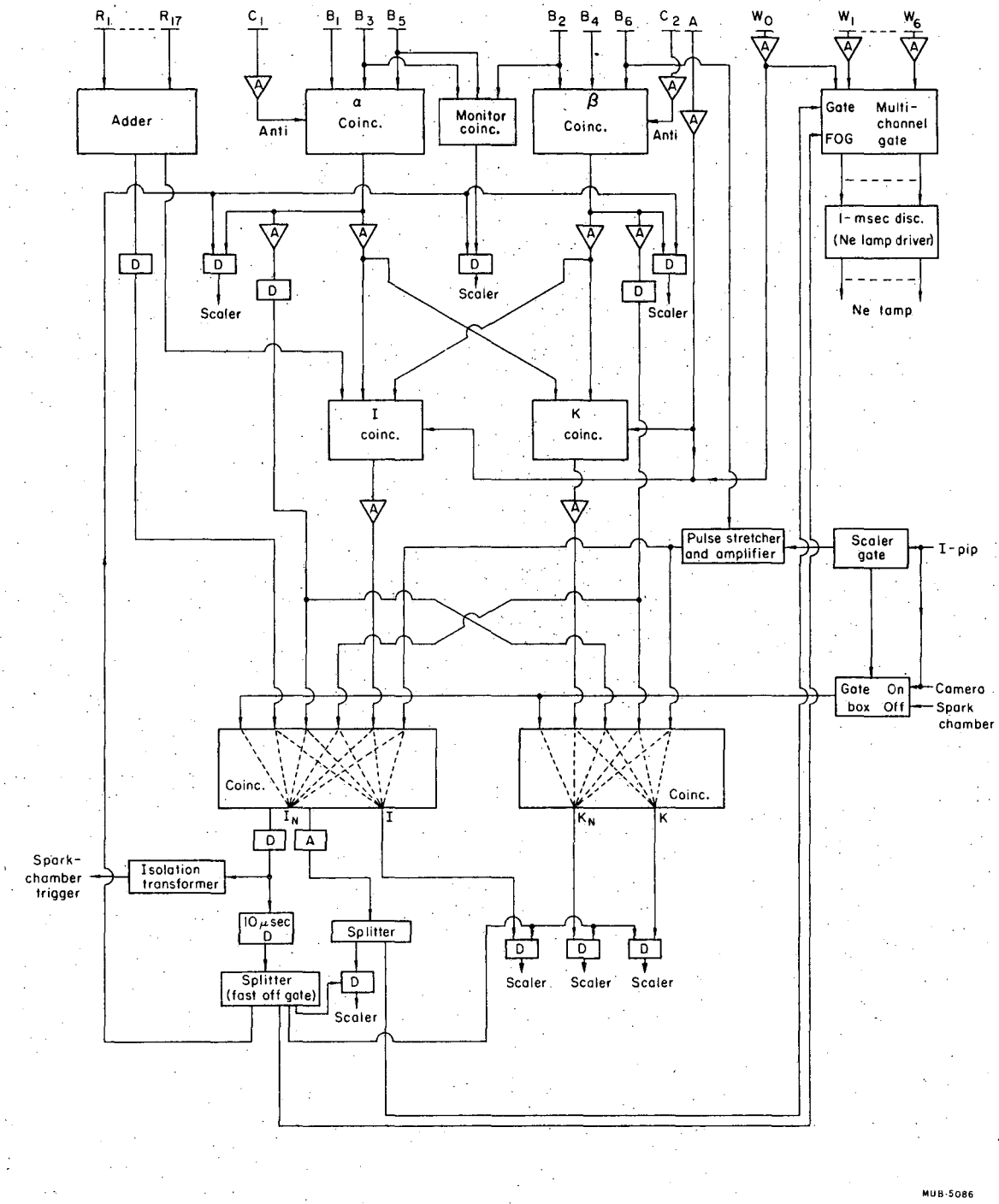

Fig. 7. Simplified block diagram of electronics.

the beam were selected by means of time-of-flight beam counters B_1 to B_6 (see Table I for counter details) and methane-gas Cerenkov counters C_1 and C_2. The Cerenkov counters produced signals only for particles of mass equal to or less than that of a pion and therefore were used in anticoincidence to reject particles lighter than kaons. For details of the construction and operation of the high-pressure gas Cerenkov counters, see references 14 and 5a.

As indicated in the block diagram, counters B_1, B_3, and B_5 with C_1 in anticoincidence formed the α coincidence. The β-coincidence signal similarly consisted of B_2, B_4, B_6, and $\bar{C}_2$. The K-coincidence signal then consisted of α and β in coincidence and counter A, used to reject off-axis beam particles, in anticoincidence. An "interaction" required counts in two or more of the 17 "barrel-stave" scintillators (Fig. 8) surrounding the cylindrical spark chamber (detected by means of a linear adder-discriminator[15]) in coincidence with a K signal, thereby forming the I-coincidence signal. If, in addition, the camera gate indicated that the camera was ready to take a picture, the signal I_N was used to trigger the spark chambers. Scalars recorded I, I_N, K, and K_N (number of kaons passing down the beam during the time the camera was capable of taking pictures). In addition, other quantities of interest were recorded such as α, β, and a monitor coincidence made up of B_2, B_3, and B_5 (essentially the total number of particles, mainly pions, in the beam).

The spark-chamber trigger pulse (I_N) was first amplified by a 4PR60A vacuum-tube pulser.[15] The 15-kV output pulse from the hard-tube pulser then triggered a spark gap, which in turn triggered 11 additional spark gaps supplying approximately -13 kV to the various spark chambers and xenon flash lamps. Specially designed low-inductance, fast-rise-time spark gaps and capacitor banks were used for the spark-chamber pulses. A picture of the smaller of two spark-gap arrays containing three spark gaps and their associated capacitor banks is shown in Fig. 9. These spark gaps were used for the beam chambers and the cylindrical chamber.

Table I. Details of counters

Counter	Type	Dimensions (in.)	Function
B_1	Scintillator	2×2×1/4	Time-of-flight counters for detecting K^- particles.
B_2		2×2×1/4	
B_3		6×6×1/4	
B_4		6×6×1/4	
B_5		8×5×1/4	
B_6		8×2×1/4	
A	Scintillator	16×16×1/2 with 8×4 rectangular hole	Rejects particles that are out of beam line
C_1	CH_4 Cerenkov	5 diameter	Detect particles lighter than K^- meson for the purpose of anticoincidence
C_2		26 long	
$W_0 - W_6$	H_2O Cerenkov	2×3 - 1/4×24	Detect particles with velocity $\beta > 0.75$
$R_1 - R_{17}$	Scintillator	20×3 - 3/4×1/2	Detect K^--p reaction products

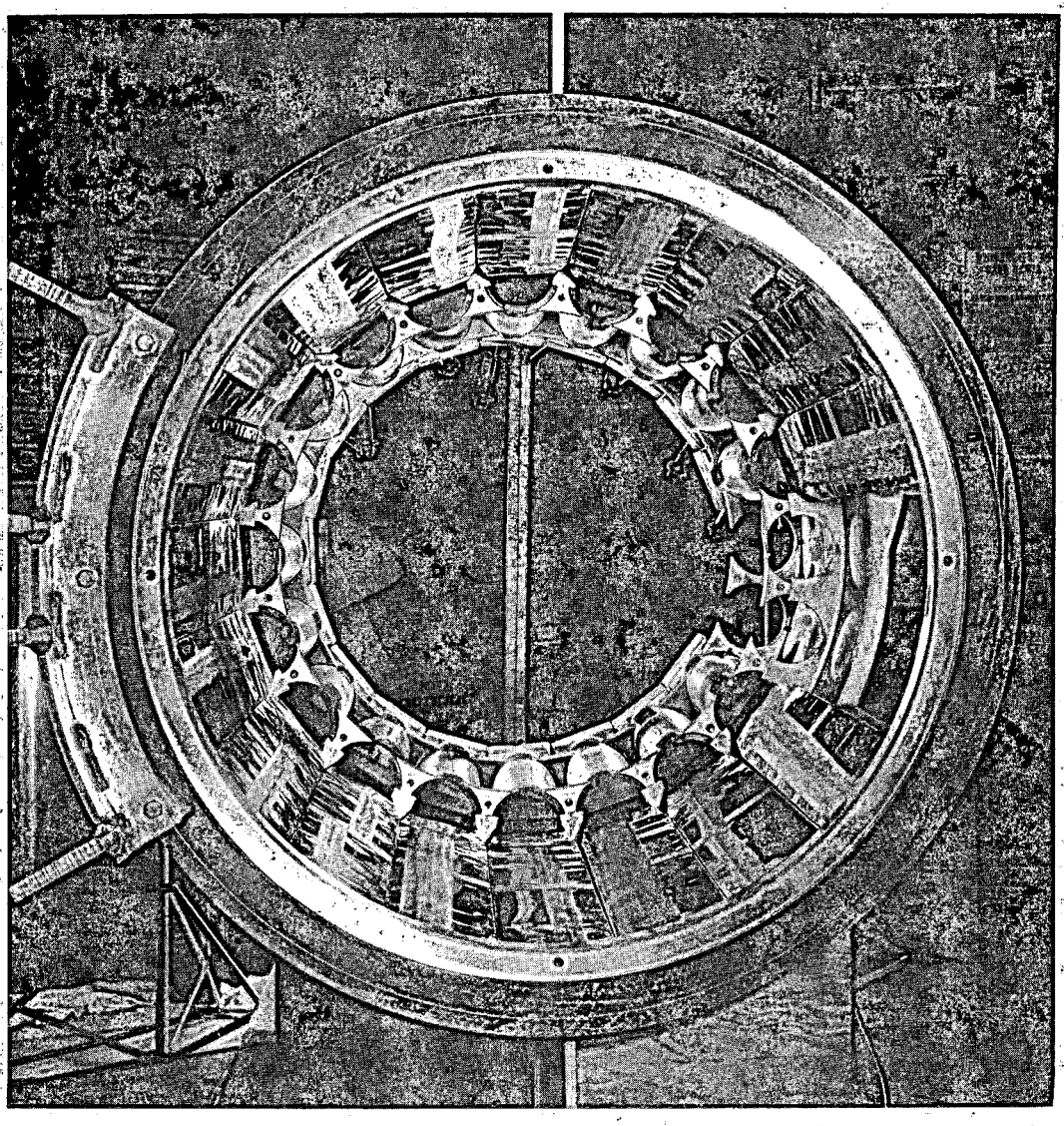

ZN-5265

Fig. 8. Ring assembly holding "barrel-stave" trigger scintillators.

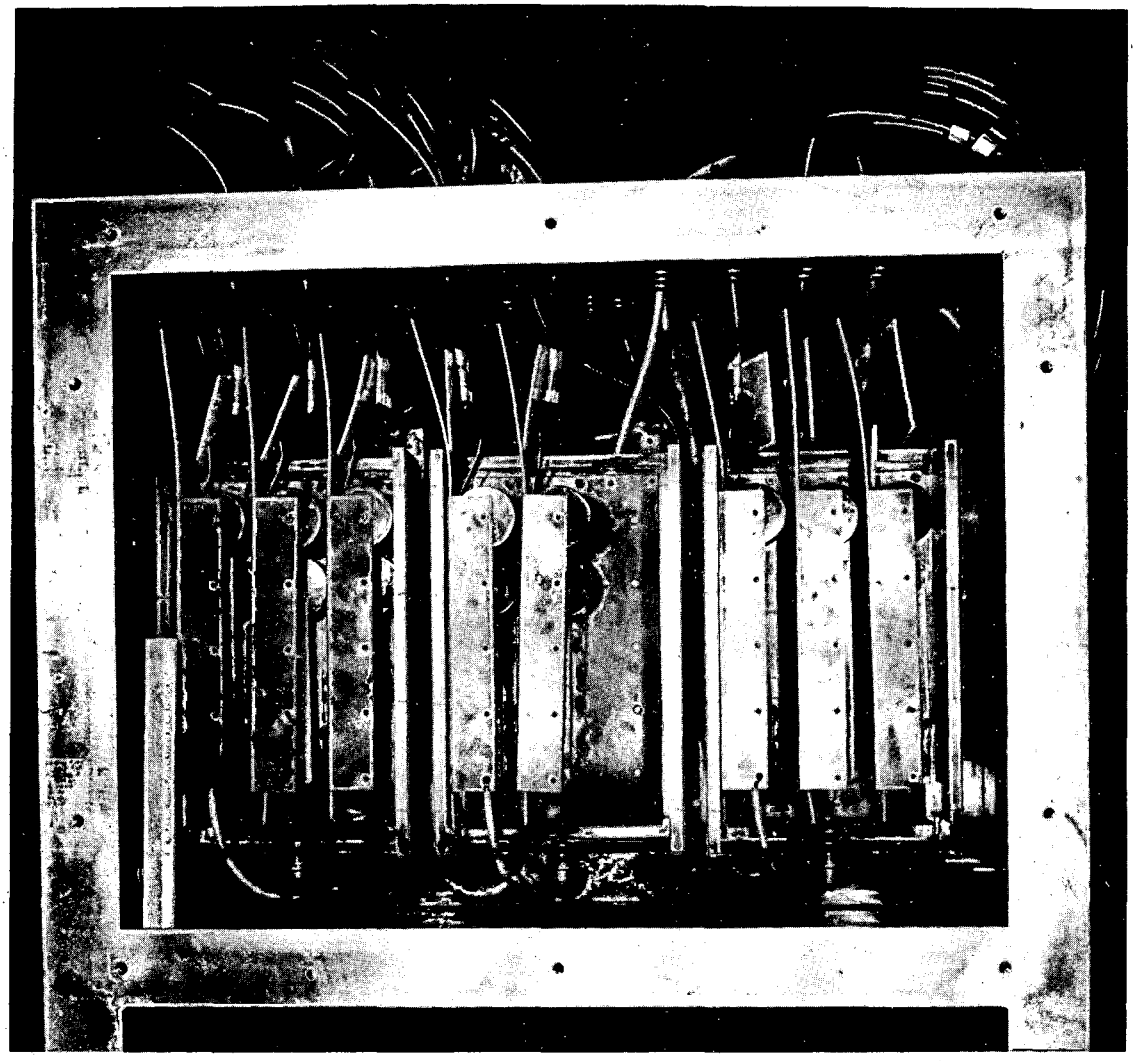

ZN-5006

Fig. 9. Three-spark-gap capacitor bank.

A similar seven-spark-gap array was used to furnish the high-voltage pulses to the large range-polarization chamber. Each capacitor bank consisted of three decoupled sets of up to ten 4000-pF 30-kV barium titanate capacitors (Sprague No. 6134).

The trigger pulse I_N also generated a fast off-gate (FOG) signal which was used to off-gate all discriminators to prevent pickup from the spark-chamber pulses.

The total delay between occurrence of an interaction in the target and application of the high-voltage pulses to the spark chambers was about 400 nsec. A clearing field of 35 V (of polarity opposite to that of the high-voltage pulses) was found to achieve the best compromise between high gap efficiency and removal of unwanted background tracks. At high beam rates, however, the number of background tracks, mainly pions, and consequently the number of unmeasurable frames became appreciable. To obviate partially this difficulty, a long (550 nsec) anticoincidence pulse derived from beam scintillator B_6 was used to reject events which follow too closely the passage of a previous beam particle. Thus when a desirable event occurred, any "old" accidental tracks were at least 0.5 μsec old and rarely resulted in background-track formation. No discrimination against accidental tracks younger than the triggering kaon was used. At large beam rates the high duty cycle of the long anticoincidence circuit resulted in a suppression of the rate of useful events. The maximum rate of accumulation of usable pictures, i.e., those without extra background tracks, occurred for a flux of 4×10^5 particles/sec.

III. DATA ANALYSIS

A. Scanning and Measuring

A total of 360 000 pictures of K^--p interactions were scanned, and about 60 000 were measured on "SCAMP", a digitized scanning and measuring projector.[16] Figure 10 shows a typical event. All pictures with a single incident track visible in each view of the beam chambers and in the incoming portion of the cylindrical chamber were considered "measurable" frames. A "track" was defined as four or more collinear sparks. Events with more than one incident track in any view of the beam chambers or in the cylindrical chamber were considered "unmeasurable". The number of unmeasurable events was recorded for normalization purposes. Measurable frames with two outgoing tracks in the cylindrical chamber which did not obviously come from an interaction in the spark-chamber plates were considered "acceptable" and were then measured.

In measuring an event the scanner first recorded parameter information such as run number, event number, scanner number, etc., on paper tape. Then position (x, y) coordinates and an angular (θ) coordinate for each track and stereo image in the beam chambers and the cylindrical chamber were punched on the tape. Measurements are made by aligning the projected image of a track with a line scribed in the translucent viewing screen. The (x, y) position was obtained by digitizing the position of the film on a microscope stage. The θ coordinate was obtained by digitizing the position of the translucent screen, which rotated in an accurately aligned mounting. In addition, for each event, fiducial measurements were made of two grid lines, roughly parallel and normal, respectively, to the incident-beam direction.

The paper tape containing the parameter information and the digitized track measurements was then processed through an IBM 1401 computer which made a few simple checks, such as testing for the correct number of measurements and throwing out all measurements

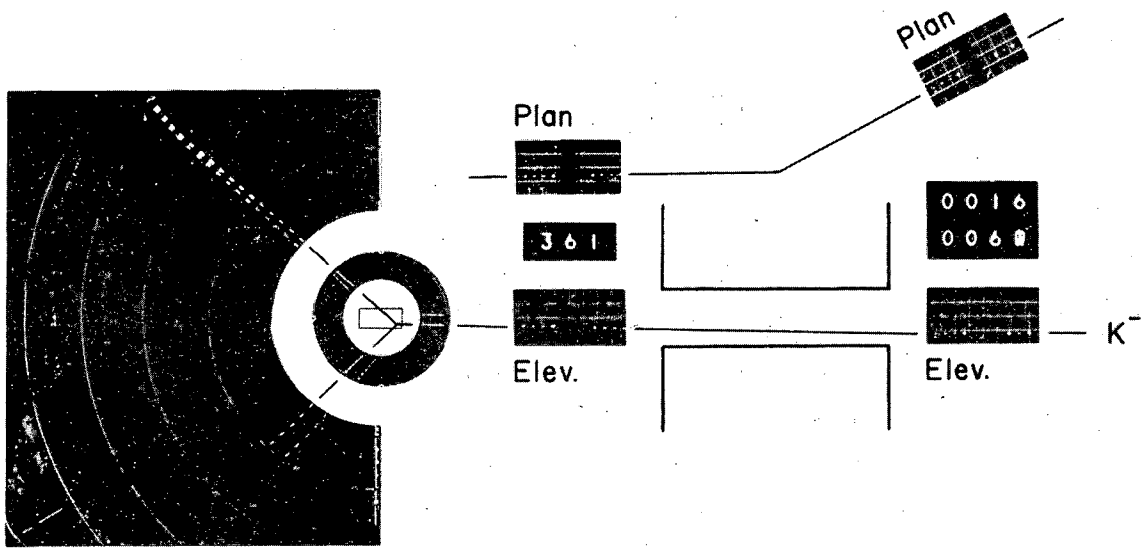

ZN-5264

Fig. 10. Example of K^--proton elastic scattering. The views of the beam-defining spark chambers have been rearranged for clarity.

and events rejected by the scanner, and produced a magnetic tape containing the corrected events.

B. Analysis

A Fortran program for use on the IBM 7094 computers at the Lawrence Radiation Laboratory computer center was written to carry out the geometrical reconstruction of events from the track and grid measurements and to fit the events to elastic-scattering kinematics.

1. Incident Momentum

The incident particle momentum for each event was determined from the bending angle of the track in magnet M_3. This bending angle was obtained from the angles made by the tracks in the plan views of the two beam spark chambers measured with respect to the beam-chamber grid lines. The magnets and grids were calibrated by removing the beam spark chambers from their positions, passing a current-carrying wire down the beam path, and photographing the wire orbits with the optical system and camera used in the experiment. Several sets of pictures were taken before, during, and after the experimental run for different magnet currents and wire currents.

2. Spatial Reconstruction of Tracks

The two fiducial measurements were used to define a coordinate system with the origin at the center of the cylindrical chamber and with the positive x axis pointing upstream (antiparallel to the incident-beam direction). The computer program converted all measurements of tracks and stereo images to this coordinate system for further analysis. The angle and separation of a track in the cylindrical chamber from its stereo image were used to obtain the dip angle and Z coordinate (height above stereo mirrors) of the track. In practice, values of Z were calculated at two points on each track (approximately the centers of gaps 3 and 7 in the cylindrical chamber) using the expression

$$Z = \frac{d}{\cos\beta \tan 2\theta}, \qquad (1)$$

where d is separation of track and image measured normal to the image, β is the angle between the axis of the reflecting mirror and the image, and θ is the tilt angle between the plane of the mirror and the $Z = 0$ plane. (See Appendix for derivation and details.) Because we have $\cos\beta \approx 1$ ($\beta \lesssim 10$ deg) and $\tan 2\theta \approx 0.2$ ($\theta \approx 5.7$ deg), the height Z above the segmented mirror is given approximately by

$$Z \approx 5d.$$

The dip angle, i.e., the angle the track makes with the x-y plane, is approximately given by a similar expression

$$\lambda \approx 5\,\alpha,$$

where λ is the dip angle, and α is the angle in the x-y plane between the track and its image.

3. Elastic Criteria

To be accepted as an elastic scatter, an event had to satisfy copunctuality, coplanarity, and kinematic criteria, and in addition, the scattering vertex had to lie inside the hydrogen-target fiducial volume.

a. Copunctuality. Because of the small angle of the cylindrical-chamber stereo mirrors, uncertainties in the Z coordinates are much larger than corresponding errors in the x-y plane. Therefore the copunctuality requirement was only applied in the x-y plane. The x-y vertex was chosen as the point which minimizes the sum of the squares of the perpendicular distances to the three cylindrical chamber tracks. The method is equivalent to a standard χ^2 vertex fit if one assumes position and angle errors are the same for each track. The minimized quantity, δV, is calculated and used as a fitting parameter, representing the deviation of the event from exact copunctuality.

b. Coplanarity. Since the dip angle of the incident track can be obtained from the downstream beam chamber by utilizing the 90-deg stereo view, errors on this dip angle are at least an order of

magnitude (factor of ~2 from better angular measurements of beam chamber tracks and another factor of $\gtrsim 7$ due to the 90-deg stereo angle) smaller than other cylindrical chamber tracks. For this reason the fitted scattering plane is required to be parallel to the incident track and is adjusted to minimize the sum of the squares of the distances in the Z direction of the centers of each track from the plane. The "center" of the track is defined as the point between the fifth and sixth gap in the cylindrical chamber. Two fitting parameters, representing deviation from coplanarity, are calculated: δZ, the minimized quantity described above, and δCOP, the sum of the squares of the angles between the outgoing tracks and the fitted scattering plane. This additional coplanarity parameter is necessary because the centers of the three cylindrical chamber tracks can be coplanar, although the tracks themselves are not. This situation could arise from events in which the outgoing tracks are decay products of particles produced in the initial reaction.

c. Elastic Kinematics. Momentum conservation at the elastic vertex requires that the scattering angle θ_K of the kaon be a unique and monotonically decreasing function of the recoil angle θ_p of the proton. This relationship, for a typical value of incident momentum, is shown in Fig. 11. The following procedure was used to compare angles θ_1 and θ_2 (angles between the incident track and the two outgoing tracks) with the elastic kinematics curve. First, θ_1 and θ_2 were assumed to be, respectively, θ_K and θ_p, and a fitting parameter, $\delta\theta$, was calculated. This fitting parameter, representing the "deviation from kinematics", is defined as the normal distance from the point θ_K and θ_p to the kinematics curve. The assignment of θ_K and θ_p was then reversed and a new "deviation from kinematics" parameter calculated. The assignment yielding the smaller $\delta\theta$ was assumed to be the correct one. The center-of-mass (c.m.) scattering angle is obtained from the intersection of the kinematics curve with the normal from the assigned θ_K and θ_p.

d. Selection of Elastic Events. Cutoffs for the fitting parameters δV, δZ, δCOP, and $\delta\theta$ for acceptable elastic events

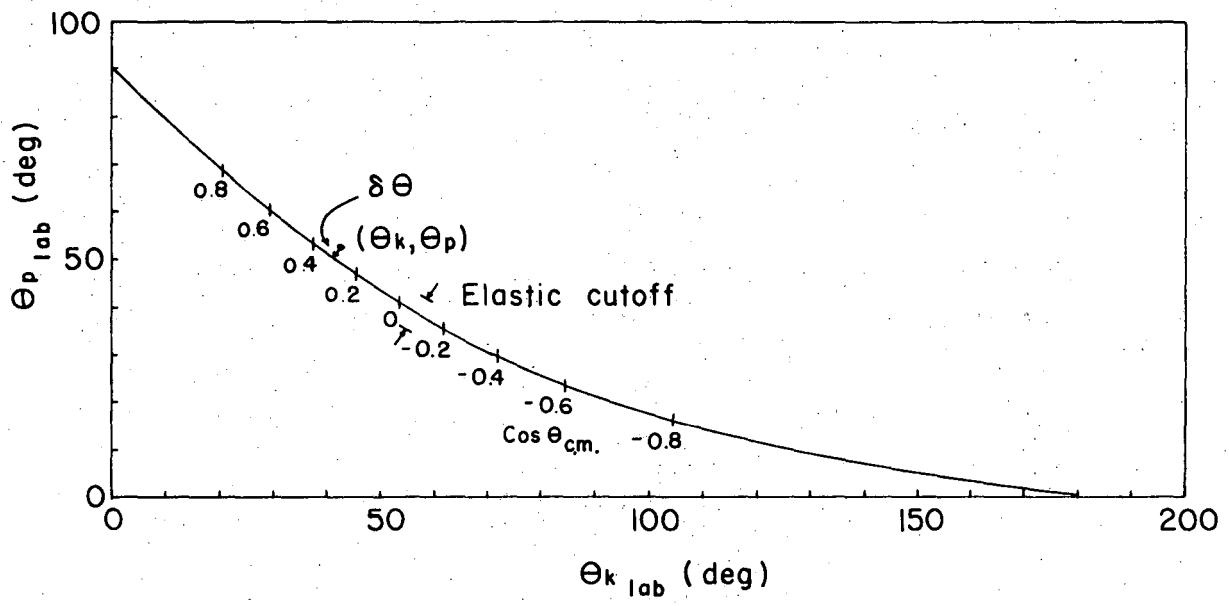

Fig. 11. Plot of θ_k against θ_p (in the laboratory system) for elastic scattering at 1000 MeV/c.

were obtained by examining the distributions of the parameters and setting the cutoffs at the points where the distributions (which in general peak up sharply for small values of the fitting parameters) fall to the background level. These distributions were examined carefully for changes as a function of beam momentum, c.m. scattering angle, dip angle of the scattering plane, etc., but were found to be essentially independent of these variables. Rough calculations indicate that the elastic cutoffs used are consistent with the uncertainties expected due to measuring errors and multiple Coulomb scattering in the hydrogen target and spark-chamber plates. Figures 12 through 15 show typical distributions and cutoffs used for the elastic fitting parameters.

Elastic events were accepted only if they originated inside a fiducial volume which was chosen to be slightly smaller than the actual liquid-hydrogen target to eliminate contamination by events that scatter in the target walls. Finally, each scattered track was required to have enough energy and be scattered in such a direction as to pass through one of the trigger scintillators.

C. Differential Cross Section

The c.m. elastic differential cross section averaged over an interval (bin) of $\cos\theta$ is given by

$$\frac{d\sigma}{d\Omega_i} = \frac{N_i \; e_i}{N_K \; n_p \; L \; \Delta\phi_i \; (\Delta\cos\theta)_i} .$$

Here N_i is the number of elastic scatters in the ith interval and e_i is a miscellaneous correction factor involving secondary interactions of scattered particles, scanning and measuring efficiency, inelastic contamination, decay in flight both of incident and scattered kaons, etc. In the denominator N_K is the effective number of incident kaons, n_p is the density of protons in the target, L is the

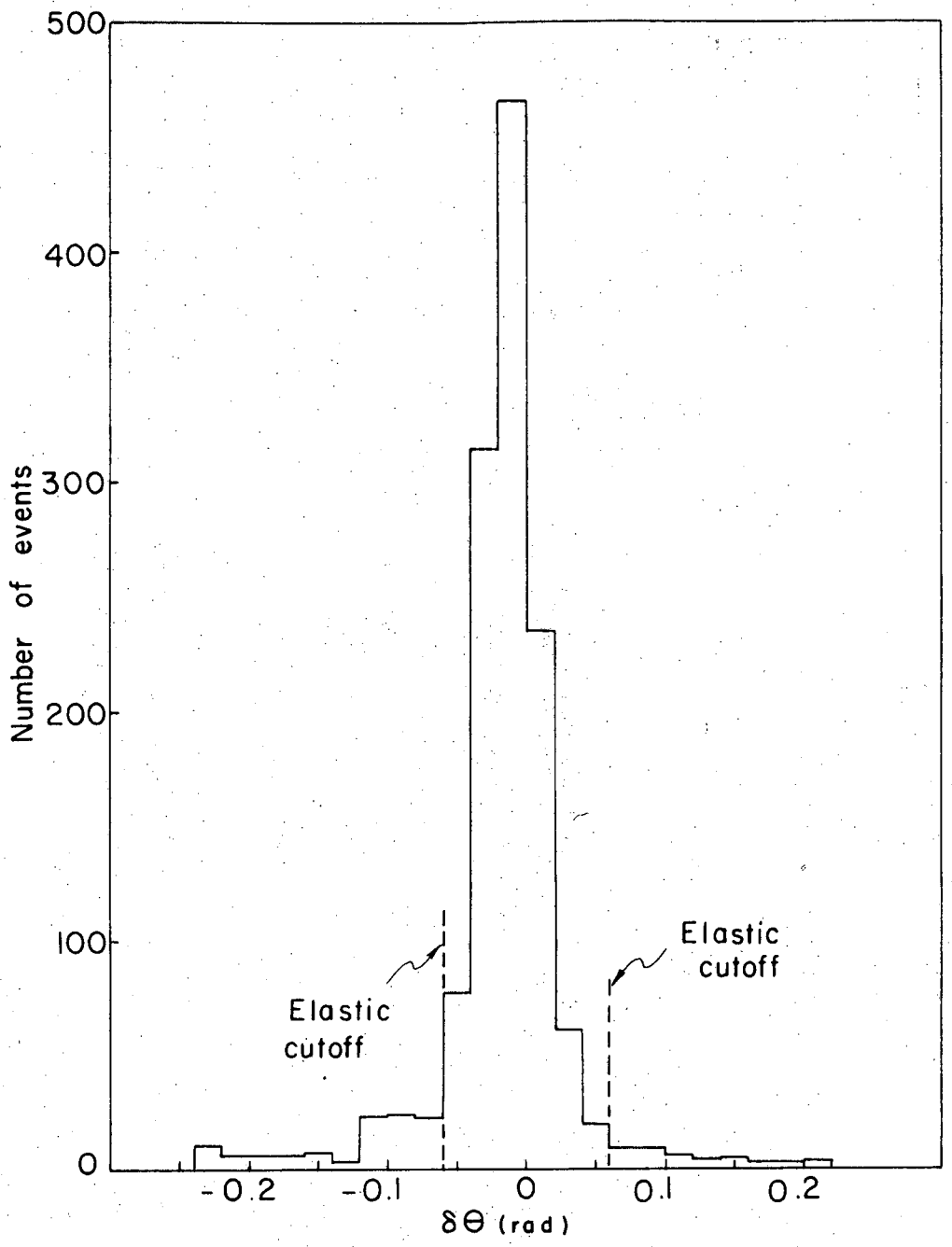

Fig. 12. Typical distribution of the "deviation from kinematics" fitting parameter, $\delta\theta$.

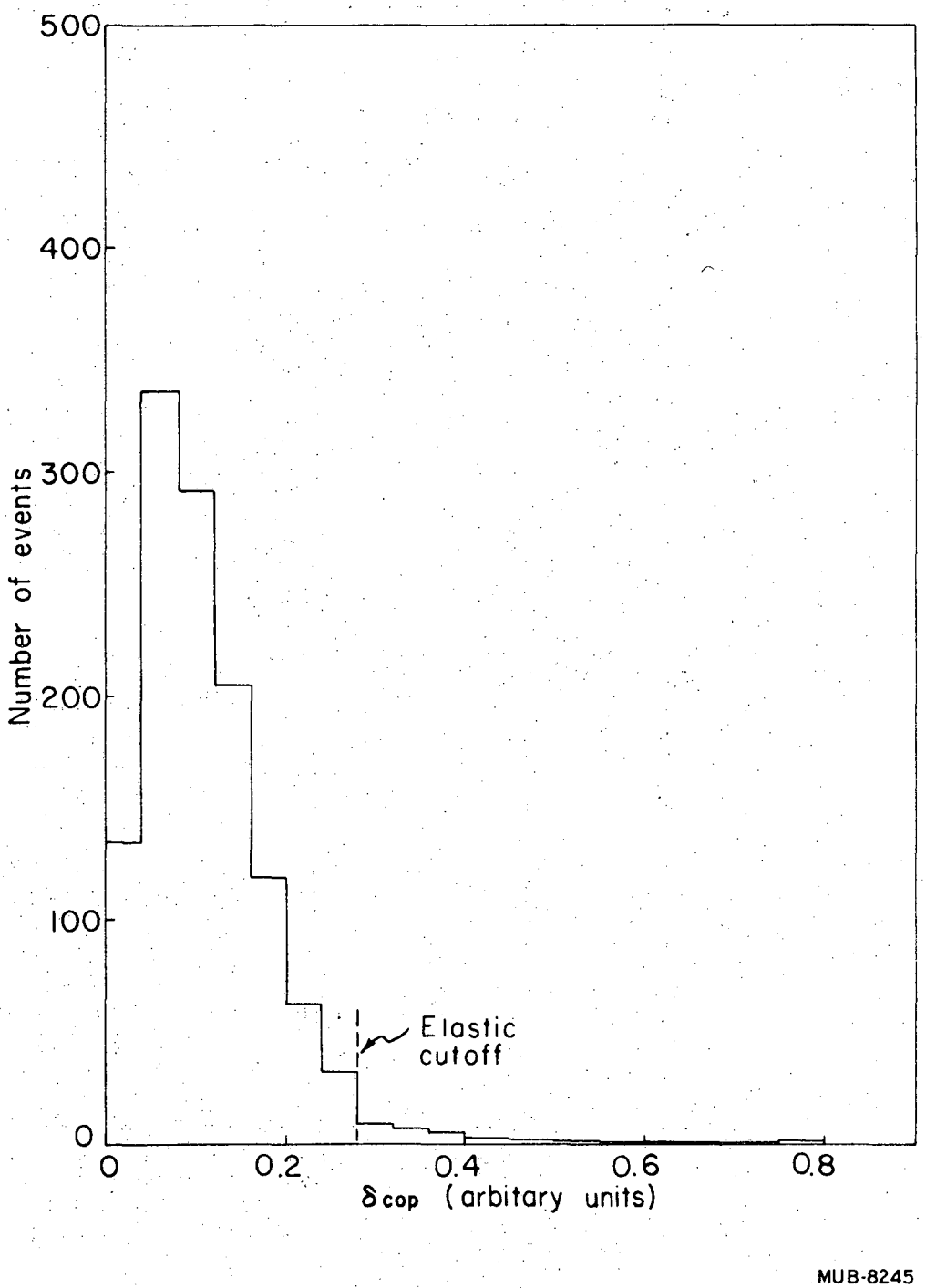

Fig. 13. Typical distribution of the coplanarity fitting parameter δ COP.

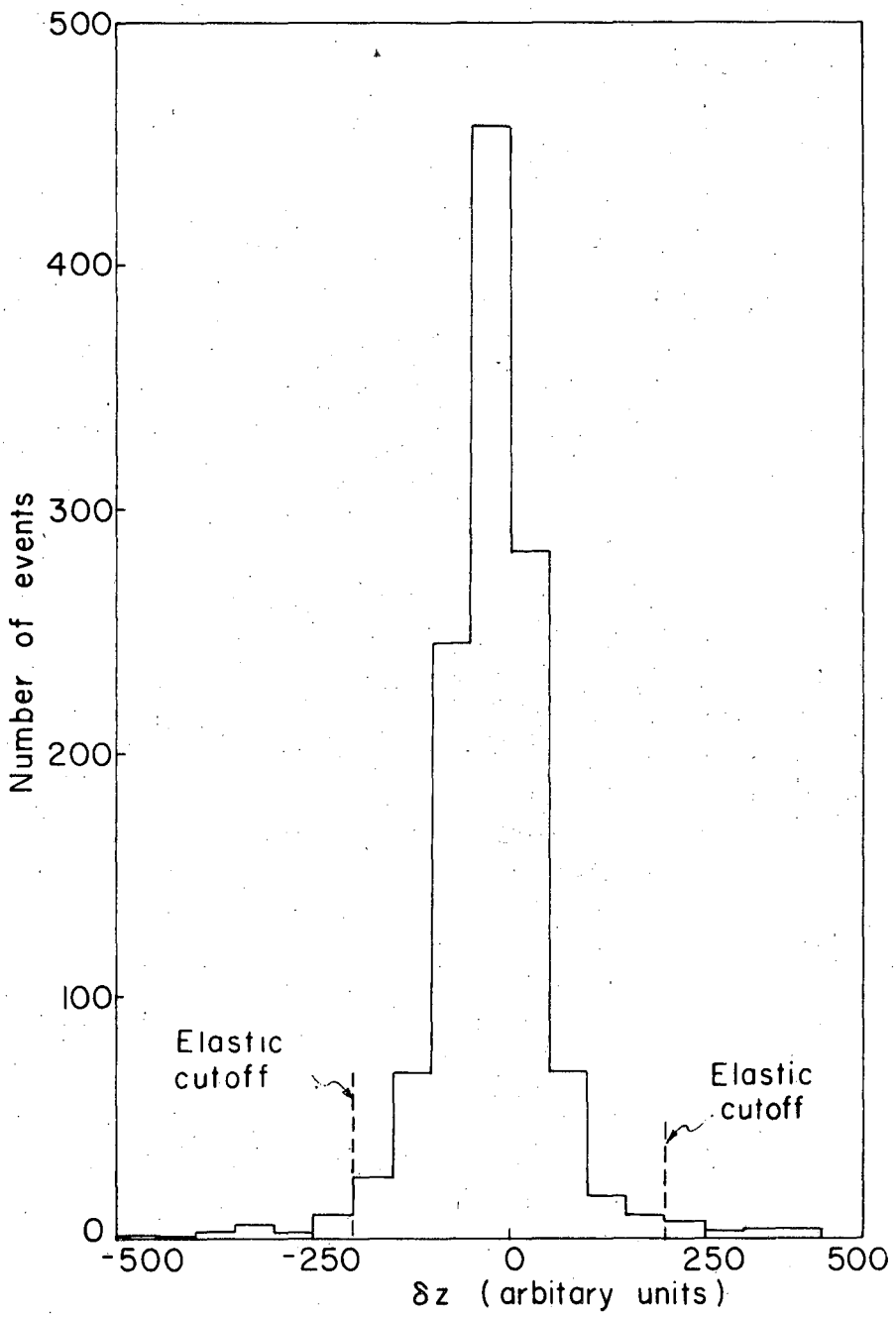

Fig. 14. Typical distribution of the fitting parameter δZ.

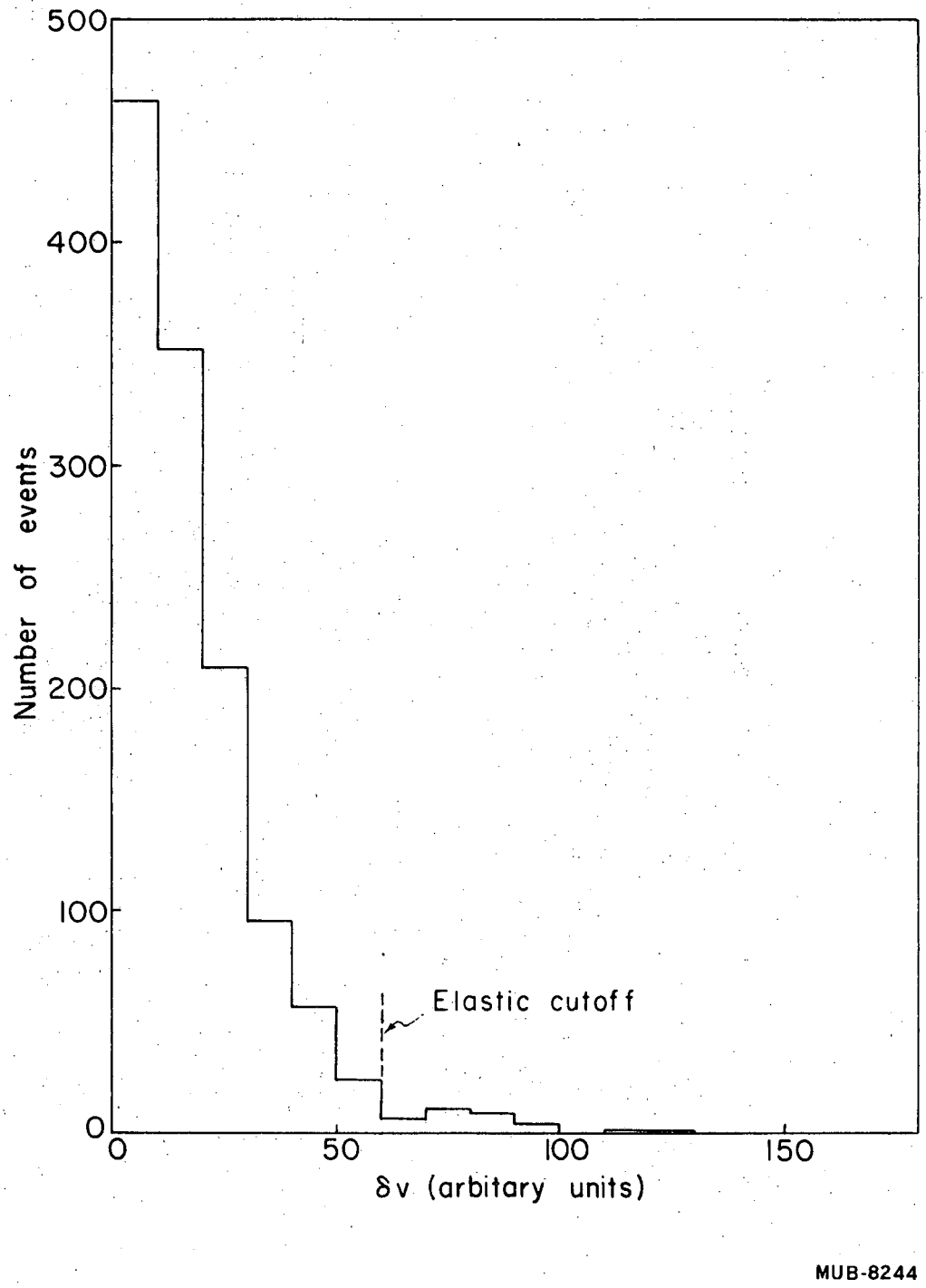

Fig. 15. Typical distribution of the copunctuality fitting parameter δV.

effective target length, $\Delta\phi_i$ is the range of azimuthal angle of the scattering plane for which elastic events trigger the spark chamber and produce acceptable pictures, $(\Delta\cos\theta)_i$ is the ith interval of $\cos\theta$, and θ is the scattering angle of the kaon in the c.m. system.

As discussed in Section III.A on scanning criteria, elastic events were selected only from the fraction of frames that contained a single incident track in the spark chambers, i.e., only from "measurable" frames. Therefore, the effective number of incident kaons that should be used for normalization purposes is

$$N_K = \frac{M}{F} \times \text{(total number of incident kaons)},$$

where M is the number of measurable frames and F is the total number of frames.

The target length, L, is the average length along the beam direction of the fiducial volume weighted by the spatial distribution of the incident beam. Periodically during the experiment, short runs were taken relaxing the requirement that at least two outgoing charged particles pass through the trigger counters. Thus every kaon incident while the system was capable of being triggered produced a picture. Since almost all of these events were simply kaons that passed through the cylindrical chamber without interacting, these runs were called "straight-through" runs. The straight-through pictures were used to obtain unbiased spatial and momentum distributions of the incident beam.

The effective azimuthal angular range, $\Delta\phi$, is a function of interaction point in the target, incident momentum, and c.m. scattering angle and was calculated from the known geometry of the system and the elastic-scattering kinematics. The correction factors associated with the loss of elastic scatters due to decay in flight of the scattered kaon, second interactions of the kaon or recoil proton in the hydrogen target, target walls, or spark chamber plates, and absorption of low-energy protons or kaons in the material were calculated and averaged over the azimuthal range. These calculations were made for a total of 240 different vertex locations, weighted by

the spatial beam distributions, and averaged over the values of $\cos\theta$ in a given bin. These weighted averages were then averaged over the momentum distribution of the beam at each momentum setting. Typical curves of $\Delta\phi/2\pi$ are shown in Fig. 16 both with and without corrections due to decay in flight, second interactions, etc.

Other correction factors applied to the data were essentially independent of the scattering angle.

Approximately half of the film was rescanned by a few specially selected scanners (and the author) to determine the scanning efficiency. The problem of determining the scanning efficiency was complicated by the fact that scanners not only could miss legitimate elastic candidates but could also incorrectly assign events to the "unmeasurable" category. The scanning efficiencies ranged from 84 ± 8% to 92 ± 4% depending on beam intensity and the general quality of the spark-chamber pictures.

The loss of events due to bad measurements by the scanners was estimated by carefully remeasuring samples of events. The average measuring efficiency was found to be approximately 93 ± 3%.

Contamination by inelastic events in the selected elastic sample was estimated to be 5 ± 3% by interpolating, through the elastic region, the flat background of inelastic events lying outside the elastic cutoffs in the $\delta\theta$ distribution. Similar procedures applied to the coplanarity-parameter distributions give approximately the same value.

Because of the discrimination against pions and lighter-mass particles in the beam provided by the gas Cerenkov counters, beam contamination mainly arose from beam kaons decaying after passing through the Cerenkov counters. The beam contamination (mostly muons) was estimated to range from 4 ± 2% at low beam momentum (700 MeV/c) to 3 ± 1.5% at high momentum.

Taking into account the errors in the correction factors and assuming a 5% uncertainty in the $\Delta\phi$ calculation, we estimate the total systematic normalization error to be approximately ± 10%.

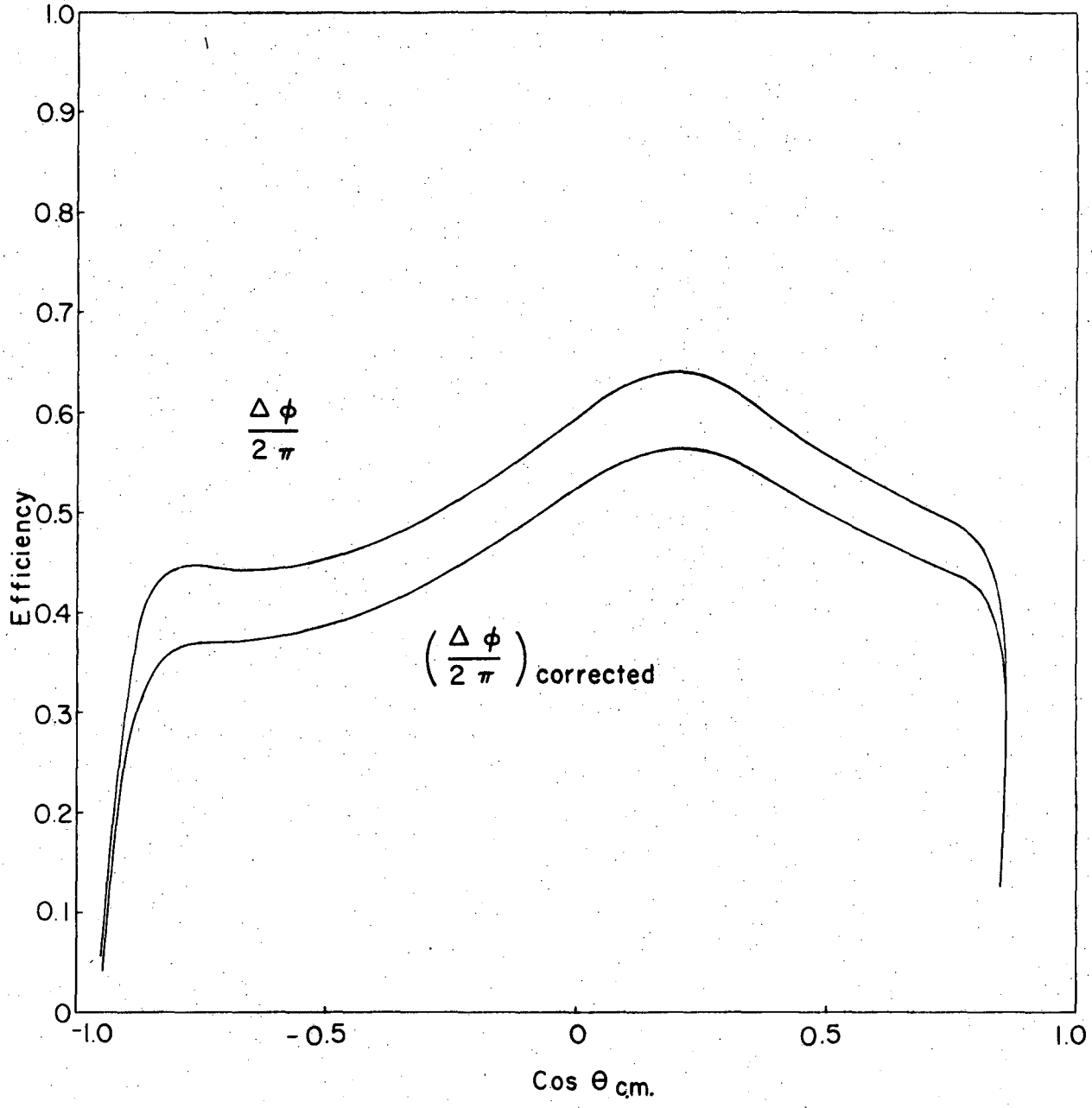

Fig. 16. Plot of cylindrical-chamber elastic-scattering detection efficiency for an incident-kaon momentum of 1000 MeV/c. The curve labeled $\Delta\phi/2\pi$ is the geometrical efficiency. The curve, $(\Delta\phi/2\pi)$ corrected, includes corrections for decay-in-flight and secondary interactions of the scattered particles.

D. Momentum Distribution

Since the incident kaon momentum for each observed elastic event is known with an accuracy of ± 1%, we were able to separate the events into momentum intervals much narrower than the ± 6% spread in the incident beam. In order to maintain reasonable statistics the events were divided into 19 momentum intervals, each 40 MeV/c wide, ranging from 660 ± 20 to 1380 ± 20 MeV/c.

The number of incident kaons appropriate for each momentum interval was obtained from the measured beam-momentum distributions (from straight-through events) and the number (N_K) of incident kaons at each nominal momentum setting. The correction and efficiency factors, e and $\Delta\phi$, needed to normalize the cross sections were also calculated for the 40-MeV/c momentum intervals.

Uncertainty in the momentum distributions of the incident beam leads to an additional normalization error for the differential cross sections in the 40-MeV/c intervals. This additional error was estimated to be ± 10% and leads to an overall uncertainty in absolute normalization of approximately ± 14%.

IV. RESULTS

The elastic differential cross sections obtained in this experiment for the 16 nominal incident momenta are given in Tables II through VII. Errors on all but the forward points are purely statistical and do not reflect the ± 10% normalization uncertainty at each momentum.

The forward differential cross section was calculated from the expression

$$\left.\frac{d\sigma}{d\Omega}\right|_{\theta = 0} = A^2 + D^2,$$

where the imaginary part of the forward-scattering amplitude is given by the optical theorem,

$$A = \frac{p^* \sigma_t}{4\pi\hbar},$$

and the real part D was obtained from the forward dispersion relations.[17] Here p^* is the c.m. momentum, and σ_t is the K^-p total cross section. The error on the forward point includes the 10% normalization error in addition to the uncertainty due to the error in the total cross section.[5] No accurate error estimate for D^2 is available; therefore an uncertainty of ± 25% is arbitrarily assumed and combined with the other errors to give the final error estimate on the forward point.

The 19 differential cross sections in 40-MeV/c momentum intervals are given in Tables VIII through XIV. The forward points were calculated as above except that the normalization uncertainty was taken to be ± 14% rather than ± 10%. Values and errors of σ_t, A^2, D^2, and $d\sigma/d\Omega|_0$ are given in Table XV.

Although the remainder of the discussion refers specifically to the 40-MeV/c angular distributions, the general behavior described applies equally well to the results at the 16 incident momenta.

For each momentum interval the c.m. differential cross section, including the forward point, has been fit by using a

least-squares fitting program DJINN[18] to a curve of the form

$$\frac{d\sigma}{d\Omega} = \sum_{0}^{N} b_n P_n(\cos\theta),$$

where $P_n(\cos\theta)$ is the Legendre polynomial of order n.

Table XVI shows the χ^2 probability $[p(\chi^2)]$ for fits of order $N=0$ through $N=6$ for each momentum. In a few cases the order necessary and sufficient to fit the data is ambiguous; however, the general trend is clear. Inspection of the table indicates that second-order fits are satisfactory up to 860 MeV/c. The 900- and 940-MeV/c distributions require third or fourth order. Fifth order appears necessary from 980 to about 1140 MeV/c. Above 1140 MeV/c only fourth-order terms are required.

The experimental differential cross sections and the fitted curves (for the order fits underlined in Table XVI) are plotted in Figs. 17 through 35. The values of the fitted coefficients and errors (for the same order fits) are given in Table XVII and plotted as a function of momentum in Figs. 36 and 37. In addition, the coefficients b_4, b_5, and b_6 from a sixth-order fit are shown in Fig. 38.

The total elastic cross sections obtained from the integral of the fitted angular distributions (simply equal to $4\pi b_0$) are given in Table XVIII and plotted in Fig. 36. It should be noted that the errors assigned to both b_0 and the total elastic cross sections include, in addition to the statistical errors obtained from the fitting program, the 14% normalization errors.

Results of other measurements[4a, 6a, 6b, 19] of the total elastic cross section in the momentum region covered by this experiment are also shown in Fig. 36. Sodickson et al.[6b] have analyzed their differential cross-section measurements in terms of Legendre-polynomial power series and, for comparison purposes, their coefficients are plotted in Figs. 36 and 37. The total elastic cross sections measured in this experiment agree quite well with the values obtained

by other groups. The higher-order coefficients are also in reasonable agreement with the results of Sodickson et al.[6b]

Fits were also made to the data using only the optical-theorem contribution to the forward point and using no forward point at all. At each momentum the three fits of the selected order were quite consistent with each other, and in most cases almost identical.

TABLE II.

KMINUS-PROTON ELASTIC DIFFERENTIAL CROSS-SECTION IN MB/SR IN C.M. SYSTEM

NOMINAL KAON LAB. MOMENTUM

701.0 MEV/C			745.0 MEV/C			775.0 MEV/C		
COS THETA	SIGMA	ERROR	COS THETA	SIGMA	ERROR	COS THETA	SIGMA	ERROR
-0.95 TO -0.90	0.453	0.277	-0.95 TO -0.90	2.096	0.784	-0.95 TO -0.90	1.095	0.445
-0.90 TO -0.80	0.622	0.136	-0.90 TO -0.80	0.461	0.146	-0.90 TO -0.80	1.003	0.180
-0.80 TO -0.70	0.350	0.097	-0.80 TO -0.70	0.543	0.151	-0.80 TO -0.70	0.760	0.149
-0.70 TO -0.60	0.402	0.104	-0.70 TO -0.60	0.374	0.125	-0.70 TO -0.60	0.349	0.101
-0.60 TO -0.50	0.290	0.087	-0.60 TO -0.50	0.367	0.122	-0.60 TO -0.50	0.285	0.090
-0.50 TO -0.40	0.484	0.111	-0.50 TO -0.40	0.355	0.118	-0.50 TO -0.40	0.468	0.114
-0.40 TO -0.30	0.315	0.087	-0.40 TO -0.30	0.717	0.164	-0.40 TO -0.30	0.369	0.098
-0.30 TO -0.20	0.361	0.092	-0.30 TO -0.20	0.359	0.114	-0.30 TO -0.20	0.325	0.090
-0.20 TO -0.10	0.651	0.120	-0.20 TO -0.10	0.306	0.102	-0.20 TO -0.10	0.355	0.092
-0.10 TO -0.	0.836	0.132	-0.10 TO -0.	0.611	0.140	-0.10 TO -0.	0.649	0.120
0. TO 0.30	0.805	0.072	0. TO 0.30	0.689	0.083	0. TO 0.30	0.750	0.072
0.30 TO 0.40	1.176	0.151	0.30 TO 0.40	1.069	0.178	0.30 TO 0.40	1.388	0.170
0.40 TO 0.50	1.570	0.177	0.40 TO 0.50	1.444	0.211	0.40 TO 0.50	1.886	0.201
0.50 TO 0.60	1.832	0.195	0.50 TO 0.60	1.802	0.241	0.50 TO 0.60	2.113	0.218
0.60 TO 0.70	2.285	0.227	0.60 TO 0.70	2.185	0.273	0.60 TO 0.70	2.487	0.243
0.70 TO 0.75	3.314	0.615	0.70 TO 0.75	3.186	0.531	0.70 TO 0.75	2.264	0.345
0.99 TO 1.00	3.678	0.672	0.75 TO 0.80	3.733	1.426	0.75 TO 0.80	2.868	0.717
			0.99 TO 1.00	4.250	0.680	0.99 TO 1.00	4.640	0.737

TABLE III.

KMINUS-PROTON ELASTIC DIFFERENTIAL CROSS-SECTION IN MB/SR IN C.M. SYSTEM

NOMINAL KAON LAB. MOMENTUM								
810.0 MEV/C			835.0 MEV/C			870.0 MEV/C		
COS THETA	SIGMA	ERROR	COS THETA	SIGMA	ERROR	COS THETA	SIGMA	ERROR
-0.95 TO -0.90	1.868	0.587	-0.95 TO -0.90	1.331	0.455	-0.95 TO -0.90	1.343	0.459
-0.90 TO -0.80	1.118	0.173	-0.90 TO -0.80	1.303	0.181	-0.90 TO -0.80	1.450	0.192
-0.80 TO -0.70	1.008	0.155	-0.80 TO -0.70	1.016	0.151	-0.80 TO -0.70	1.029	0.153
-0.70 TO -0.60	0.690	0.128	-0.70 TO -0.60	1.016	0.151	-0.70 TO -0.60	1.040	0.153
-0.60 TO -0.50	0.606	0.119	-0.60 TO -0.50	0.328	0.085	-0.60 TO -0.50	0.618	0.117
-0.50 TO -0.40	0.338	0.087	-0.50 TO -0.40	0.423	0.095	-0.50 TO -0.40	0.470	0.100
-0.40 TO -0.30	0.322	0.083	-0.40 TO -0.30	0.514	0.102	-0.40 TO -0.30	0.691	0.118
-0.30 TO -0.20	0.327	0.082	-0.30 TO -0.20	0.374	0.085	-0.30 TO -0.20	0.482	0.096
-0.20 TO -0.10	0.289	0.075	-0.20 TO -0.10	0.380	0.083	-0.20 TO -0.10	0.528	0.098
-0.10 TO -0.	0.584	0.103	-0.10 TO -0.	0.478	0.090	-0.10 TO -0.	0.566	0.098
0. TO 0.30	0.752	0.065	0. TO 0.30	0.790	0.065	0. TO 0.30	0.735	0.063
0.30 TO 0.40	1.164	0.140	0.30 TO 0.40	1.408	0.149	0.30 TO 0.40	1.753	0.167
0.40 TO 0.50	1.590	0.167	0.40 TO 0.50	1.971	0.180	0.40 TO 0.50	1.985	0.181
0.50 TO 0.60	1.802	0.182	0.50 TO 0.60	2.446	0.206	0.50 TO 0.60	2.079	0.190
0.60 TO 0.70	2.698	0.229	0.60 TO 0.70	2.903	0.230	0.60 TO 0.70	3.136	0.240
0.70 TO 0.75	2.578	0.325	0.70 TO 0.75	3.411	0.360	0.70 TO 0.80	3.511	0.268
0.75 TO 0.80	2.965	0.528	0.75 TO 0.80	3.386	0.530	0.80 TO 0.85	6.635	1.662
0.99 TO 1.00	5.051	0.799	0.99 TO 1.00	5.380	0.721	0.99 TO 1.00	6.775	0.966

TABLE IV.

KMINUS-PROTON ELASTIC DIFFERENTIAL CROSS-SECTION IN MB/SR IN C.M. SYSTEM

NOMINAL KAON LAB. MOMENTUM

905.0 MEV/C			941.0 MEV/C			985.0 MEV/C		
COS THETA	SIGMA	ERROR	COS THETA	SIGMA	ERROR	COS THETA	SIGMA	ERROR
-0.95 TO -0.90	1.981	0.586	-0.95 TO -0.90	2.154	0.666	-0.95 TO -0.90	1.843	0.570
-0.90 TO -0.80	1.361	0.177	-0.90 TO -0.80	1.909	0.235	-0.90 TO -0.80	1.696	0.204
-0.80 TO -0.70	1.241	0.160	-0.80 TO -0.70	1.582	0.202	-0.80 TO -0.70	1.538	0.184
-0.70 TO -0.60	0.696	0.119	-0.70 TO -0.60	1.381	0.188	-0.70 TO -0.60	1.214	0.162
-0.60 TO -0.50	0.678	0.116	-0.60 TO -0.50	0.696	0.131	-0.60 TO -0.50	0.714	0.123
-0.50 TO -0.40	0.791	0.122	-0.50 TO -0.40	0.765	0.135	-0.50 TO -0.40	0.847	0.131
-0.40 TO -0.30	0.458	0.092	-0.40 TO -0.30	0.455	0.102	-0.40 TO -0.30	0.575	0.105
-0.30 TO -0.20	0.504	0.094	-0.30 TO -0.20	0.453	0.099	-0.30 TO -0.20	0.254	0.068
-0.20 TO -0.10	0.409	0.082	-0.20 TO -0.10	0.345	0.084	-0.20 TO -0.10	0.512	0.093
-0.10 TO -0.	0.602	0.096	-0.10 TO -0.	0.287	0.074	-0.10 TO -0.	0.417	0.082
0. TO 0.30	0.684	0.057	0. TO 0.30	0.623	0.061	0. TO 0.30	0.557	0.053
0.30 TO 0.40	1.263	0.135	0.30 TO 0.40	0.980	0.132	0.30 TO 0.40	0.959	0.120
0.40 TO 0.50	1.521	0.151	0.40 TO 0.50	1.280	0.154	0.40 TO 0.50	0.798	0.112
0.50 TO 0.60	2.106	0.182	0.50 TO 0.60	1.645	0.180	0.50 TO 0.60	1.436	0.154
0.60 TO 0.70	2.608	0.208	0.60 TO 0.70	2.151	0.211	0.60 TO 0.70	2.061	0.190
0.70 TO 0.80	3.083	0.234	0.70 TO 0.80	3.881	0.292	0.70 TO 0.80	3.305	0.247
0.80 TO 0.85	4.685	0.949	0.80 TO 0.85	4.699	0.767	0.80 TO 0.85	3.059	0.502
0.99 TO 1.00	8.252	1.137	0.99 TO 1.00	8.863	1.186	0.99 TO 1.00	9.486	1.267

TABLE V.

KMINUS-PROTON ELASTIC DIFFERENTIAL CROSS-SECTION IN MB/SR IN C.M. SYSTEM

NOMINAL KAON LAB. MOMENTUM

1035.0 MEV/C			1085.0 MEV/C			1125.0 MEV/C		
COS THETA	SIGMA	ERROR	COS THETA	SIGMA	ERROR	COS THETA	SIGMA	ERROR
-0.95 TO -0.90	1.598	0.521	-0.95 TO -0.90	1.740	0.522	-0.95 TO -0.90	2.430	0.695
-0.90 TO -0.80	1.702	0.208	-0.90 TO -0.80	1.505	0.176	-0.90 TO -0.80	0.887	0.146
-0.80 TO -0.70	1.242	0.167	-0.80 TO -0.70	1.035	0.137	-0.80 TO -0.70	1.151	0.155
-0.70 TO -0.60	1.063	0.153	-0.70 TO -0.60	1.117	0.141	-0.70 TO -0.60	0.818	0.129
-0.60 TO -0.50	1.095	0.153	-0.60 TO -0.50	0.584	0.100	-0.60 TO -0.50	0.892	0.133
-0.50 TO -0.40	0.740	0.123	-0.50 TO -0.40	0.560	0.096	-0.50 TO -0.40	0.491	0.096
-0.40 TO -0.30	0.546	0.103	-0.40 TO -0.30	0.562	0.094	-0.40 TO -0.30	0.556	0.100
-0.30 TO -0.20	0.635	0.108	-0.30 TO -0.20	0.551	0.090	-0.30 TO -0.20	0.472	0.089
-0.20 TO -0.10	0.648	0.106	-0.20 TO -0.10	0.447	0.078	-0.20 TO -0.10	0.410	0.080
-0.10 TO -0.	0.349	0.075	-0.10 TO -0.	0.490	0.079	-0.10 TO -0.	0.251	0.061
0. TO 0.30	0.533	0.052	0. TO 0.30	0.438	0.042	0. TO 0.30	0.496	0.047
0.30 TO 0.40	0.980	0.122	0.30 TO 0.40	0.485	0.077	0.30 TO 0.40	0.751	0.102
0.40 TO 0.50	0.707	0.106	0.40 TO 0.50	0.687	0.093	0.40 TO 0.50	0.729	0.103
0.50 TO 0.60	1.388	0.153	0.50 TO 0.60	1.117	0.123	0.50 TO 0.60	1.410	0.148
0.60 TO 0.70	2.336	0.204	0.60 TO 0.70	2.129	0.174	0.60 TO 0.70	1.690	0.167
0.70 TO 0.80	3.994	0.274	0.70 TO 0.80	3.275	0.222	0.70 TO 0.80	2.959	0.227
0.80 TO 0.85	5.012	0.476	0.80 TO 0.85	4.010	0.366	0.80 TO 0.85	4.210	0.397
0.85 TO 0.90	9.112	2.763	0.85 TO 0.90	7.098	1.680	0.85 TO 0.90	5.305	1.064
0.99 TO 1.00	1.183	1.385	0.99 TO 1.00	1.103	1.457	0.99 TO 1.00	9.311	1.285

TABLE VI.

KMINUS-PROTON ELASTIC DIFFERENTIAL CROSS-SECTION IN MB/SR IN C.M. SYSTEM

NOMINAL KAON LAB. MOMENTUM

1175.0 MEV/C			1225.0 MEV/C			1290.0 MEV/C		
COS THETA	SIGMA	ERROR	COS THETA	SIGMA	ERROR	COS THETA	SIGMA	ERROR
-0.95 TO -0.90	1.017	0.348	-0.95 TO -0.90	0.918	0.373	-0.95 TO -0.90	0.562	0.219
-0.90 TO -0.80	1.141	0.145	-0.90 TO -0.80	0.935	0.158	-0.90 TO -0.80	0.842	0.111
-0.80 TO -0.70	0.990	0.126	-0.80 TO -0.70	0.601	0.118	-0.80 TO -0.70	0.930	0.107
-0.70 TO -0.60	0.901	0.118	-0.70 TO -0.60	0.492	0.105	-0.70 TO -0.60	0.587	0.084
-0.60 TO -0.50	0.631	0.097	-0.60 TO -0.50	0.260	0.075	-0.60 TO -0.50	0.300	0.059
-0.50 TO -0.40	0.573	0.091	-0.50 TO -0.40	0.350	0.085	-0.50 TO -0.40	0.362	0.063
-0.40 TO -0.30	0.596	0.090	-0.40 TO -0.30	0.273	0.073	-0.40 TO -0.30	0.394	0.064
-0.30 TO -0.20	0.407	0.072	-0.30 TO -0.20	0.292	0.073	-0.30 TO -0.20	0.358	0.059
-0.20 TO -0.10	0.428	0.071	-0.20 TO -0.10	0.392	0.082	-0.20 TO -0.10	0.297	0.052
-0.10 TO -0.	0.411	0.067	-0.10 TO -0.	0.365	0.076	-0.10 TO -0.	0.276	0.048
0. TO 0.30	0.455	0.039	0. TO 0.30	0.328	0.040	0. TO 0.30	0.378	0.031
0.30 TO 0.40	0.851	0.095	0.30 TO 0.40	0.603	0.095	0.30 TO 0.40	0.569	0.067
0.40 TO 0.50	0.916	0.100	0.40 TO 0.50	0.890	0.119	0.40 TO 0.50	0.803	0.082
0.50 TO 0.60	1.174	0.117	0.50 TO 0.60	1.132	0.138	0.50 TO 0.60	1.233	0.105
0.60 TO 0.70	1.782	0.149	0.60 TO 0.70	1.778	0.179	0.60 TO 0.70	1.731	0.129
0.70 TO 0.80	3.085	0.202	0.70 TO 0.80	3.092	0.243	0.70 TO 0.80	2.666	0.165
0.80 TO 0.85	3.744	0.325	0.80 TO 0.85	3.273	0.366	0.80 TO 0.85	3.264	0.267
0.85 TO 0.90	3.109	0.627	0.85 TO 0.90	3.244	0.675	0.85 TO 0.90	2.966	0.539
0.99 TO 1.00	8.183	1.184	0.99 TO 1.00	7.029	0.813	0.99 TO 1.00	6.786	0.796

TABLE VII.

KMINUS-PROTON ELASTIC DIFFERENTIAL CROSS-SECTION IN MB/SR IN C.M. SYSTEM

NOMINAL KAON LAB. MOMENTUM

1350.0 MEV/C

COS THETA	SIGMA	ERROR
-0.95 TO -0.90	0.889	0.543
-0.90 TO -0.80	0.687	0.217
-0.80 TO -0.70	0.813	0.217
-0.70 TO -0.60	0.560	0.177
-0.60 TO -0.50	0.537	0.170
-0.50 TO -0.40	0.306	0.125
-0.40 TO -0.30	0.288	0.118
-0.30 TO -0.20	0.224	0.100
-0.20 TO -0.10	0.291	0.110
-0.10 TO -0.	0.348	0.116
0. TO 0.30	0.287	0.059
0.30 TO 0.40	0.408	0.123
0.40 TO 0.50	0.707	0.167
0.50 TO 0.60	1.296	0.233
0.60 TO 0.70	1.424	0.252
0.70 TO 0.80	2.657	0.355
0.80 TO 0.85	3.582	0.605
0.85 TO 0.90	3.955	0.935
0.99 TO 1.00	7.095	0.834

TABLE VIII.

KMINUS-PROTON ELASTIC DIFFERENTIAL CROSS-SECTION IN MB/SR IN C.M. SYSTEM

KAON LAB. MOMENTUM (40 MEV/C INTERVAL)

660.0 MEV/C			700.0 MEV/C			740.0 MEV/C		
COS THETA	SIGMA	ERROR	COS THETA	SIGMA	ERROR	COS THETA	SIGMA	ERROR
-0.95 TO -0.90	0.	0.546	-0.95 TO -0.90	0.746	0.456	-0.95 TO -0.90	1.254	0.510
-0.90 TO -0.80	0.298	0.172	-0.90 TO -0.80	0.634	0.176	-0.90 TO -0.80	0.629	0.144
-0.80 TO -0.70	0.361	0.181	-0.80 TO -0.70	0.443	0.140	-0.80 TO -0.70	0.629	0.137
-0.70 TO -0.60	0.542	0.221	-0.70 TO -0.60	0.486	0.147	-0.70 TO -0.60	0.209	0.079
-0.60 TO -0.50	0.177	0.125	-0.60 TO -0.50	0.390	0.130	-0.60 TO -0.50	0.205	0.077
-0.50 TO -0.40	0.688	0.243	-0.50 TO -0.40	0.504	0.145	-0.50 TO -0.40	0.311	0.094
-0.40 TO -0.30	0.740	0.247	-0.40 TO -0.30	0.201	0.090	-0.40 TO -0.30	0.216	0.076
-0.30 TO -0.20	0.629	0.223	-0.30 TO -0.20	0.498	0.138	-0.30 TO -0.20	0.142	0.060
-0.20 TO -0.10	0.970	0.269	-0.20 TO -0.10	0.472	0.131	-0.20 TO -0.10	0.256	0.079
-0.10 TO -0.	0.992	0.265	-0.10 TO -0.	0.895	0.176	-0.10 TO -0.	0.623	0.120
-0. TO 0.30	0.791	0.132	-0. TO 0.30	0.748	0.089	-0. TO 0.30	0.667	0.069
0.30 TO 0.40	1.306	0.292	0.30 TO 0.40	1.238	0.198	0.30 TO 0.40	1.001	0.146
0.40 TO 0.50	0.805	0.232	0.40 TO 0.50	1.833	0.245	0.40 TO 0.50	1.565	0.186
0.50 TO 0.60	1.686	0.344	0.50 TO 0.60	1.680	0.240	0.50 TO 0.60	1.730	0.200
0.60 TO 0.70	2.199	0.423	0.60 TO 0.70	1.947	0.267	0.60 TO 0.70	2.534	0.248
0.70 TO 0.75	2.710	1.328	0.70 TO 0.75	3.328	0.744	0.70 TO 0.75	2.910	0.420
0.99 TO 1.00	3.157	0.672	0.99 TO 1.00	3.670	0.765	0.75 TO 0.80	3.647	1.311
						0.99 TO 1.00	4.200	0.793

TABLE IX.

KMINUS-PROTON ELASTIC DIFFERENTIAL CROSS-SECTION IN MB/SR IN C.M. SYSTEM

KAON LAB. MOMENTUM (40 MEV/C INTERVAL)

780.0 MEV/C			820.0 MEV/C			860.0 MEV/C		
COS THETA	SIGMA	ERROR	COS THETA	SIGMA	ERROR	COS THETA	SIGMA	ERROR
-0.95 TO -0.90	1.423	0.500	-0.95 TO -0.90	1.395	0.456	-0.95 TO -0.90	1.780	0.534
-0.90 TO -0.80	1.078	0.168	-0.90 TO -0.80	1.201	0.162	-0.90 TO -0.80	1.271	0.167
-0.80 TO -0.70	0.758	0.134	-0.80 TO -0.70	1.101	0.147	-0.80 TO -0.70	1.162	0.151
-0.70 TO -0.60	0.613	0.120	-0.70 TO -0.60	0.917	0.134	-0.70 TO -0.60	0.896	0.132
-0.60 TO -0.50	0.461	0.103	-0.60 TO -0.50	0.458	0.094	-0.60 TO -0.50	0.685	0.114
-0.50 TO -0.40	0.424	0.097	-0.50 TO -0.40	0.387	0.085	-0.50 TO -0.40	0.533	0.099
-0.40 TO -0.30	0.555	0.109	-0.40 TO -0.30	0.501	0.094	-0.40 TO -0.30	0.491	0.093
-0.30 TO -0.20	0.426	0.093	-0.30 TO -0.20	0.326	0.074	-0.30 TO -0.20	0.382	0.080
-0.20 TO -0.10	0.365	0.084	-0.20 TO -0.10	0.363	0.076	-0.20 TO -0.10	0.313	0.070
-0.10 TO -0.	0.599	0.104	-0.10 TO -0.	0.389	0.076	-0.10 TO -0.	0.635	0.097
-0. TO 0.30	0.841	0.069	-0. TO 0.30	0.779	0.060	-0. TO 0.30	0.846	0.062
0.30 TO 0.40	1.277	0.146	0.30 TO 0.40	1.686	0.153	0.30 TO 0.40	1.524	0.145
0.40 TO 0.50	1.876	0.181	0.40 TO 0.50	1.890	0.164	0.40 TO 0.50	1.938	0.166
0.50 TO 0.60	2.587	0.217	0.50 TO 0.60	2.231	0.183	0.50 TO 0.60	2.133	0.179
0.60 TO 0.70	2.713	0.228	0.60 TO 0.70	2.944	0.216	0.60 TO 0.70	2.916	0.215
0.70 TO 0.75	2.714	0.337	0.70 TO 0.75	3.397	0.336	0.70 TO 0.80	3.169	0.235
0.75 TO 0.80	3.926	0.845	0.75 TO 0.80	3.605	0.559	0.80 TO 0.85	5.878	1.755
0.99 TO 1.00	4.690	0.880	0.99 TO 1.00	5.168	0.967	0.99 TO 1.00	6.331	1.111

TABLE X.

KMINUS-PROTON ELASTIC DIFFERENTIAL CROSS-SECTION IN MB/SR IN C.M. SYSTEM

KAON LAB. MOMENTUM (40 MEV/C INTERVAL)

900.0 MEV/C			940.0 MEV/C			980.0 MEV/C		
COS THETA	SIGMA	ERROR	COS THETA	SIGMA	ERROR	COS THETA	SIGMA	ERROR
-0.95 TO -0.90	1.769	0.547	-0.95 TO -0.90	2.980	0.813	-0.95 TO -0.90	2.278	0.693
-0.90 TO -0.80	1.298	0.177	-0.90 TO -0.80	1.937	0.219	-0.90 TO -0.80	2.044	0.242
-0.80 TO -0.70	1.250	0.164	-0.80 TO -0.70	1.247	0.167	-0.80 TO -0.70	1.698	0.209
-0.70 TO -0.60	0.981	0.145	-0.70 TO -0.60	0.988	0.147	-0.70 TO -0.60	1.295	0.181
-0.60 TO -0.50	0.602	0.112	-0.60 TO -0.50	0.661	0.119	-0.60 TO -0.50	0.664	0.128
-0.50 TO -0.40	0.783	0.125	-0.50 TO -0.40	0.780	0.126	-0.50 TO -0.40	0.803	0.138
-0.40 TO -0.30	0.611	0.108	-0.40 TO -0.30	0.606	0.109	-0.40 TO -0.30	0.539	0.110
-0.30 TO -0.20	0.471	0.092	-0.30 TO -0.20	0.463	0.093	-0.30 TO -0.20	0.436	0.096
-0.20 TO -0.10	0.511	0.093	-0.20 TO -0.10	0.540	0.097	-0.20 TO -0.10	0.429	0.093
-0.10 TO -0.	0.627	0.100	-0.10 TO -0.	0.361	0.077	-0.10 TO -0.	0.460	0.093
-0. TO 0.30	0.729	0.060	-0. TO 0.30	0.667	0.058	-0. TO 0.30	0.556	0.057
0.30 TO 0.40	1.450	0.147	0.30 TO 0.40	1.071	0.128	0.30 TO 0.40	1.035	0.135
0.40 TO 0.50	1.756	0.165	0.40 TO 0.50	1.306	0.144	0.40 TO 0.50	0.879	0.127
0.50 TO 0.60	2.129	0.187	0.50 TO 0.60	1.883	0.178	0.50 TO 0.60	1.546	0.173
0.60 TO 0.70	2.942	0.226	0.60 TO 0.70	2.558	0.213	0.60 TO 0.70	2.209	0.213
0.70 TO 0.80	3.585	0.257	0.70 TO 0.80	3.821	0.268	0.70 TO 0.80	3.957	0.292
0.80 TO 0.85	6.385	1.235	0.80 TO 0.85	4.289	0.690	0.80 TO 0.85	4.366	0.678
0.99 TO 1.00	8.160	1.390	0.99 TO 1.00	8.850	1.478	0.99 TO 1.00	9.409	1.570

TABLE XI.

KMINUS-PROTON ELASTIC DIFFERENTIAL CROSS-SECTION IN MB/SR IN C.M. SYSTEM

KAON LAB. MOMENTUM (40 MEV/C INTERVAL)

1020.0 MEV/C			1060.0 MEV/C			1100.0 MEV/C		
COS THETA	SIGMA	ERROR	COS THETA	SIGMA	ERROR	COS THETA	SIGMA	ERROR
-0.95 TO -0.90	1.538	0.526	-0.95 TO -0.90	2.181	0.674	-0.95 TO -0.90	1.768	0.556
-0.90 TO -0.80	2.082	0.242	-0.90 TO -0.80	1.780	0.226	-0.90 TO -0.80	1.187	0.171
-0.80 TO -0.70	1.680	0.205	-0.80 TO -0.70	1.145	0.171	-0.80 TO -0.70	1.259	0.165
-0.70 TO -0.60	1.255	0.176	-0.70 TO -0.60	1.498	0.193	-0.70 TO -0.60	0.975	0.144
-0.60 TO -0.50	0.978	0.153	-0.60 TO -0.50	1.016	0.157	-0.60 TO -0.50	0.822	0.130
-0.50 TO -0.40	0.641	0.121	-0.50 TO -0.40	0.833	0.139	-0.50 TO -0.40	0.628	0.111
-0.40 TO -0.30	0.609	0.115	-0.40 TO -0.30	0.682	0.122	-0.40 TO -0.30	0.652	0.110
-0.30 TO -0.20	0.535	0.105	-0.30 TO -0.20	0.601	0.112	-0.30 TO -0.20	0.508	0.094
-0.20 TO -0.10	0.579	0.106	-0.20 TO -0.10	0.642	0.112	-0.20 TO -0.10	0.509	0.091
-0.10 TO -0.	0.400	0.085	-0.10 TO -0.	0.456	0.091	-0.10 TO -0.	0.476	0.085
-0. TO 0.30	0.447	0.050	-0. TO 0.30	0.400	0.048	-0. TO 0.30	0.403	0.044
0.30 TO 0.40	0.619	0.102	0.30 TO 0.40	0.479	0.090	0.30 TO 0.40	0.766	0.105
0.40 TO 0.50	0.559	0.100	0.40 TO 0.50	0.626	0.106	0.40 TO 0.50	0.728	0.105
0.50 TO 0.60	1.116	0.145	0.50 TO 0.60	1.043	0.141	0.50 TO 0.60	1.222	0.140
0.60 TO 0.70	1.945	0.196	0.60 TO 0.70	1.725	0.186	0.60 TO 0.70	1.892	0.180
0.70 TO 0.80	3.209	0.259	0.70 TO 0.80	3.558	0.275	0.70 TO 0.80	3.193	0.240
0.80 TO 0.85	3.930	0.598	0.80 TO 0.85	4.743	0.478	0.80 TO 0.85	3.897	0.391
0.99 TO 1.00	0.732	1.776	0.85 TO 0.90	8.279	2.441	0.85 TO 0.90	4.551	1.175
			0.99 TO 1.00	1.851	1.929	0.99 TO 1.00	0.155	1.590

TABLE XII.

KMINUS-PROTON ELASTIC DIFFERENTIAL CROSS-SECTION IN MB/SR IN C.M. SYSTEM

KAON LAB. MOMENTUM (40 MEV/C INTERVAL)

1140.0 MEV/C			1180.0 MEV/C			1220.0 MEV/C		
COS THETA	SIGMA	ERROR	COS THETA	SIGMA	ERROR	COS THETA	SIGMA	ERROR
-0.95 TO -0.90	1.307	0.447	-0.95 TO -0.90	1.460	0.499	-0.95 TO -0.90	0.393	0.240
-0.90 TO -0.80	1.017	0.155	-0.90 TO -0.80	1.004	0.163	-0.90 TO -0.80	0.923	0.169
-0.80 TO -0.70	0.826	0.131	-0.80 TO -0.70	0.848	0.139	-0.80 TO -0.70	0.690	0.135
-0.70 TO -0.60	1.008	0.142	-0.70 TO -0.60	0.512	0.107	-0.70 TO -0.60	0.619	0.126
-0.60 TO -0.50	0.625	0.111	-0.60 TO -0.50	0.410	0.094	-0.60 TO -0.50	0.497	0.111
-0.50 TO -0.40	0.578	0.104	-0.50 TO -0.40	0.411	0.092	-0.50 TO -0.40	0.521	0.111
-0.40 TO -0.30	0.459	0.090	-0.40 TO -0.30	0.350	0.082	-0.40 TO -0.30	0.358	0.089
-0.30 TO -0.20	0.406	0.082	-0.30 TO -0.20	0.438	0.089	-0.30 TO -0.20	0.399	0.091
-0.20 TO -0.10	0.458	0.084	-0.20 TO -0.10	0.392	0.082	-0.20 TO -0.10	0.293	0.076
-0.10 TO -0.	0.377	0.074	-0.10 TO -0.	0.302	0.069	-0.10 TO -0.	0.420	0.087
-0. TO 0.30	0.537	0.049	-0. TO 0.30	0.520	0.051	-0. TO 0.30	0.366	0.045
0.30 TO 0.40	0.671	0.096	0.30 TO 0.40	0.768	0.108	0.30 TO 0.40	0.710	0.111
0.40 TO 0.50	0.948	0.117	0.40 TO 0.50	0.872	0.118	0.40 TO 0.50	1.004	0.135
0.50 TO 0.60	1.296	0.141	0.50 TO 0.60	1.531	0.161	0.50 TO 0.60	1.378	0.164
0.60 TO 0.70	1.975	0.179	0.60 TO 0.70	1.964	0.187	0.60 TO 0.70	1.873	0.196
0.70 TO 0.80	3.039	0.228	0.70 TO 0.80	3.026	0.240	0.70 TO 0.80	3.397	0.273
0.80 TO 0.85	3.416	0.354	0.80 TO 0.85	4.413	0.424	0.80 TO 0.85	4.158	0.442
0.85 TO 0.90	5.532	1.084	0.85 TO 0.90	4.698	0.933	0.85 TO 0.90	4.237	0.860
0.99 TO 1.00	9.141	1.567	0.99 TO 1.00	8.199	1.443	0.99 TO 1.00	7.235	1.103

TABLE XIII.

KMINUS-PROTON ELASTIC DIFFERENTIAL CROSS-SECTION IN MB/SR IN C.M. SYSTEM

KAON LAB. MOMENTUM (40 MEV/C INTERVAL)

1260.0 MEV/C			1300.0 MEV/C			1340.0 MEV/C		
COS THETA	SIGMA	ERROR	COS THETA	SIGMA	ERROR	COS THETA	SIGMA	ERROR
-0.95 TO -0.90	0.651	0.319	-0.95 TO -0.90	0.521	0.318	-0.95 TO -0.90	0.836	0.511
-0.90 TO -0.80	0.820	0.158	-0.90 TO -0.80	0.608	0.157	-0.90 TO -0.80	1.033	0.258
-0.80 TO -0.70	0.833	0.147	-0.80 TO -0.70	0.793	0.165	-0.80 TO -0.70	0.983	0.232
-0.70 TO -0.60	0.605	0.123	-0.70 TO -0.60	0.533	0.133	-0.70 TO -0.60	0.631	0.182
-0.60 TO -0.50	0.389	0.097	-0.60 TO -0.50	0.289	0.096	-0.60 TO -0.50	0.303	0.124
-0.50 TO -0.40	0.208	0.069	-0.50 TO -0.40	0.183	0.075	-0.50 TO -0.40	0.432	0.144
-0.40 TO -0.30	0.480	0.102	-0.40 TO -0.30	0.402	0.107	-0.40 TO -0.30	0.272	0.111
-0.30 TO -0.20	0.368	0.087	-0.30 TO -0.20	0.269	0.085	-0.30 TO -0.20	0.211	0.094
-0.20 TO -0.10	0.304	0.076	-0.20 TO -0.10	0.125	0.056	-0.20 TO -0.10	0.549	0.147
-0.10 TO -0.	0.248	0.066	-0.10 TO -0.	0.232	0.073	-0.10 TO -0.	0.328	0.109
-0. TO 0.30	0.432	0.049	-0. TO 0.30	0.273	0.044	-0. TO 0.30	0.372	0.065
0.30 TO 0.40	0.676	0.107	0.30 TO 0.40	0.645	0.120	0.30 TO 0.40	0.419	0.121
0.40 TO 0.50	0.872	0.125	0.40 TO 0.50	0.799	0.137	0.40 TO 0.50	0.703	0.161
0.50 TO 0.60	1.287	0.156	0.50 TO 0.60	1.124	0.168	0.50 TO 0.60	1.063	0.205
0.60 TO 0.70	1.850	0.193	0.60 TO 0.70	1.618	0.207	0.60 TO 0.70	1.631	0.261
0.70 TO 0.80	2.739	0.242	0.70 TO 0.80	2.603	0.271	0.70 TO 0.80	2.809	0.354
0.80 TO 0.85	3.631	0.409	0.80 TO 0.85	3.045	0.431	0.80 TO 0.85	3.367	0.569
0.85 TO 0.90	2.373	0.719	0.85 TO 0.90	2.113	0.676	0.85 TO 0.90	3.764	1.165
0.99 TO 1.00	6.831	1.050	0.99 TO 1.00	6.785	1.047	0.99 TO 1.00	6.757	1.046

TABLE XIV.

KMINUS-PROTON ELASTIC DIFFERENTIAL CROSS-SECTION IN MB/SR IN C.M. SYSTEM

KAON LAB. MOMENTUM (40 MEV/C INTERVAL)

1380.0 MEV/C

COS THETA	SIGMA	ERROR
-0.95 TO -0.90	0.812	0.828
-0.90 TO -0.80	0.377	0.267
-0.80 TO -0.70	1.580	0.500
-0.70 TO -0.60	0.759	0.340
-0.60 TO -0.50	1.021	0.386
-0.50 TO -0.40	0.553	0.276
-0.40 TO -0.30	0.781	0.319
-0.30 TO -0.20	0.364	0.210
-0.20 TO -0.10	0.563	0.252
-0.10 TO -0.	0.418	0.209
-0. TO 0.30	0.420	0.117
0.30 TO 0.40	0.502	0.225
0.40 TO 0.50	0.852	0.301
0.50 TO 0.60	0.907	0.321
0.60 TO 0.70	2.532	0.553
0.70 TO 0.80	4.380	0.751
0.80 TO 0.85	3.342	0.965
0.85 TO 0.90	7.267	2.411
0.99 TO 1.00	7.136	1.106

Table XV. Quantities used to calculate forward differential cross sections. Values of σ_t are obtained by interpolation of cross sections from references 5a and 5b. Errors in D^2 are assumed to be ± 25% and errors in $d\sigma/d\Omega|_o$ include ± 14% normalization uncertainty.

P_K (MeV/c)	σ_t (mb)	A^2 (mb/sr)	D^2 (mb/sr)	$\frac{d\sigma}{d\Omega}\Big\|_o$ (mb/sr)
660	35.7 ± 3.0	2.98 ± 0.65	0.18 ± 0.04	3.16 ± 0.67
700	36.0 ± 3.0	3.33 ± 0.73	0.34 ± 0.08	3.67 ± 0.76
740	36.3 ± 2.5	3.70 ± 0.73	0.50 ± 0.12	4.20 ± 0.79
780	36.3 ± 2.5	4.02 ± 0.79	0.67 ± 0.17	4.69 ± 0.88
820	36.1 ± 2.5	4.30 ± 0.85	0.87 ± 0.22	5.17 ± 0.97
860	38.5 ± 2.2	5.26 ± 0.96	1.07 ± 0.27	6.33 ± 1.11
900	42.9 ± 2.2	7.00 ± 1.22	1.16 ± 0.29	8.16 ± 1.39
940	44.3 ± 2.1	7.97 ± 1.36	0.88 ± 0.22	8.85 ± 1.48
980	45.2 ± 2.1	8.83 ± 1.49	0.58 ± 0.14	9.41 ± 1.57
1020	47.7 ± 2.1	10.43 ± 1.74	0.30 ± 0.08	10.73 ± 1.78
1060	49.2 ± 2.0	11.74 ± 1.92	0.11 ± 0.03	11.85 ± 1.93
1100	44.5 ± 1.5	10.13 ± 1.59	0.02 ± 0.01	10.15 ± 1.59
1140	41.1 ± 2.0	9.10 ± 1.56	0.04 ± 0.01	9.14 ± 1.57
1180	37.9 ± 2.0	8.13 ± 1.43	0.07 ± 0.02	8.20 ± 1.44
1220	34.8 ± 1.0	7.18 ± 1.10	0.05 ± 0.01	7.23 ± 1.10
1260	33.1 ± 1.0	6.80 ± 1.04	0.03 ± 0.01	6.83 ± 1.05
1300	32.3 ± 1.0	6.76 ± 1.04	0.02 ± 0.01	6.78 ± 1.05
1340	31.4 ± 1.0	6.67 ± 1.03	0.09 ± 0.02	6.76 ± 1.04
1380	31.5 ± 1.0	6.99 ± 1.08	0.15 ± 0.04	7.14 ± 1.10

Table XVI. Chi-square confidence levels for order of fit N = 1 through N = 6. The orders selected as necessary and sufficient to fit the data are underlined. The corresponding coefficients are listed in Table XVII and plotted in Figs. 36 and 37.

P_K (MeV/c)	Order of fit					
	1	2	3	4	5	6
660	.06	.15	.23	.26	.27	.56
700	0	.42	.36	.29	.23	.17
740	0	.28	.25	.29	.28	.23
780	0	.67	.69	.61	.71	.67
820	0	.66	.69	.65	.58	.49
860	0	.71	.69	.64	.67	.66
900	0	.02	.43	.54	.47	.43
940	0	0	.05	.77	.70	.87
980	0	0	0	.19	.40	.33
1020	0	0	0	.16	.74	.71
1060	0	0	0	.24	.71	.76
1100	0	0	0	.53	.75	.70
1140	0	0	.02	.45	.82	.78
1180	0	0	0	.88	.91	.90
1220	0	0	.16	.59	.72	.71
1260	0	0	.01	.14	.15	.14
1300	0	0	.06	.13	.14	.11
1340	0	0	.02	.78	.82	.91
1380	0	0	.40	.47	.44	.50

Table XVII. Coefficients, b_n, for Legendre polynomial power-series expansion of differential cross section in the form $\frac{d\sigma}{d\Omega} = \sum_{0}^{N} b_n P_n(\cos\theta)$. The units of b_n are mb/sr.

p_K (MeV/c)	Order of Fit	b_0	b_1	b_2	b_3	b_4	b_5	b_6
660	2	.961 ± .155	1.029 ± .151	.409 ± .189	—	—	—	—
700	2	1.126 ± .170	1.296 ± .115	1.038 ± .143	—	—	—	—
740	2	1.114 ± .165	1.487 ± .090	1.372 ± .111	—	—	—	—
780	2	1.423 ± .207	1.540 ± .092	1.644 ± .118	—	—	—	—
820	2	1.533 ± .222	1.606 ± .085	2.040 ± .110	—	—	—	—
860	2	1.553 ± .224	1.476 ± .083	1.968 ± .109	—	—	—	—
900	4	1.712 ± .251	1.862 ± .149	2.510 ± .224	.734 ± .180	.308 ± .198	—	—
	6	1.747 ± .259	1.924 ± .198	2.662 ± .295	.849 ± .305	.519 ± .329	.114 ± .221	.178 ± .241
940	4	1.739 ± .255	1.647 ± .147	3.048 ± .230	.831 ± .174	.765 ± .200	—	—
	6	1.813 ± .269	1.670 ± .202	3.376 ± .311	.872 ± .312	1.244 ± .353	.048 ± .228	.424 ± .247
980	5	1.786 ± .263	1.722 ± .210	3.524 ± .255	1.494 ± .320	1.213 ± .219	.502 ± .232	—
	6	1.772 ± .264	1.713 ± .211	3.463 ± .322	1.481 ± .322	1.121 ± .367	.490 ± .235	−.081 ± .261
1020	5	1.656 ± .244	1.563 ± .200	3.409 ± .241	1.945 ± .304	1.347 ± .204	.693 ± .226	—
	6	1.621 ± .244	1.521 ± .208	3.255 ± .322	1.875 ± .318	1.129 ± .364	.649 ± .234	−.179 ± .248
1060	5	1.685 ± .247	1.817 ± .196	3.475 ± .232	2.350 ± .305	1.415 ± .203	.633 ± .231	—
	6	1.746 ± .260	1.874 ± .202	3.752 ± .326	2.452 ± .317	1.797 ± .376	.698 ± .237	.311 ± .258
1100	5	1.457 ± .213	1.611 ± .159	2.712 ± .193	1.671 ± .251	.873 ± .176	.376 ± .195	—
	6	1.476 ± .220	1.628 ± .163	2.801 ± .263	1.701 ± .258	1.001 ± .313	.399 ± .201	.112 ± .228
1140	5	1.352 ± .198	1.663 ± .147	2.364 ± .179	1.438 ± .235	.717 ± .168	.438 ± .183	—
	6	1.369 ± .204	1.681 ± .152	2.444 ± .244	1.470 ± .245	.831 ± .291	.465 ± .192	.099 ± .207
1180	4	1.340 ± .196	1.656 ± .116	2.483 ± .176	.991 ± .140	.829 ± .157	—	—
	6	1.381 ± .206	1.788 ± .156	2.672 ± .244	1.246 ± .245	1.077 ± .287	.242 ± .190	.156 ± .204
1220	4	1.248 ± .183	1.741 ± .118	2.203 ± .164	1.208 ± .139	.427 ± .150	—	—
	6	1.253 ± .186	1.835 ± .138	2.230 ± .198	1.416 ± .213	.395 ± .229	.211 ± .169	−.157 ± .183
1260	4	1.117 ± .165	1.404 ± .110	1.951 ± .157	.767 ± .131	.464 ± .142	—	—
1300	4	.953 ± .143	1.305 ± .115	1.755 ± .161	.722 ± .132	.292 ± .144	—	—
1340	4	1.147 ± .175	1.331 ± .152	2.294 ± .215	.929 ± .174	.859 ± .197	—	—
1380	4	1.317 ± .211	1.820 ± .231	2.218 ± .297	1.688 ± .274	.440 ± .315	—	—

Table XVIII. Total elastic cross sections obtained in this experiment. Values given are integrals under the fitted curves for the order of fit underlined in Table XVI. The ± 14% normalization error is combined with the statistical error.

P_K (MeV/c)	σ_e (mb)
660	12.08 ± 1.95
700	14.15 ± 2.14
740	14.00 ± 2.07
780	17.88 ± 2.60
820	19.26 ± 2.79
860	19.52 ± 2.82
900	21.51 ± 3.15
940	21.85 ± 3.20
980	22.44 ± 3.30
1020	20.78 ± 3.06
1060	21.17 ± 3.11
1100	18.31 ± 2.68
1140	16.99 ± 2.49
1180	16.84 ± 2.47
1220	15.68 ± 2.30
1260	14.04 ± 2.07
1300	11.98 ± 1.80
1340	14.41 ± 2.20
1380	16.55 ± 2.66

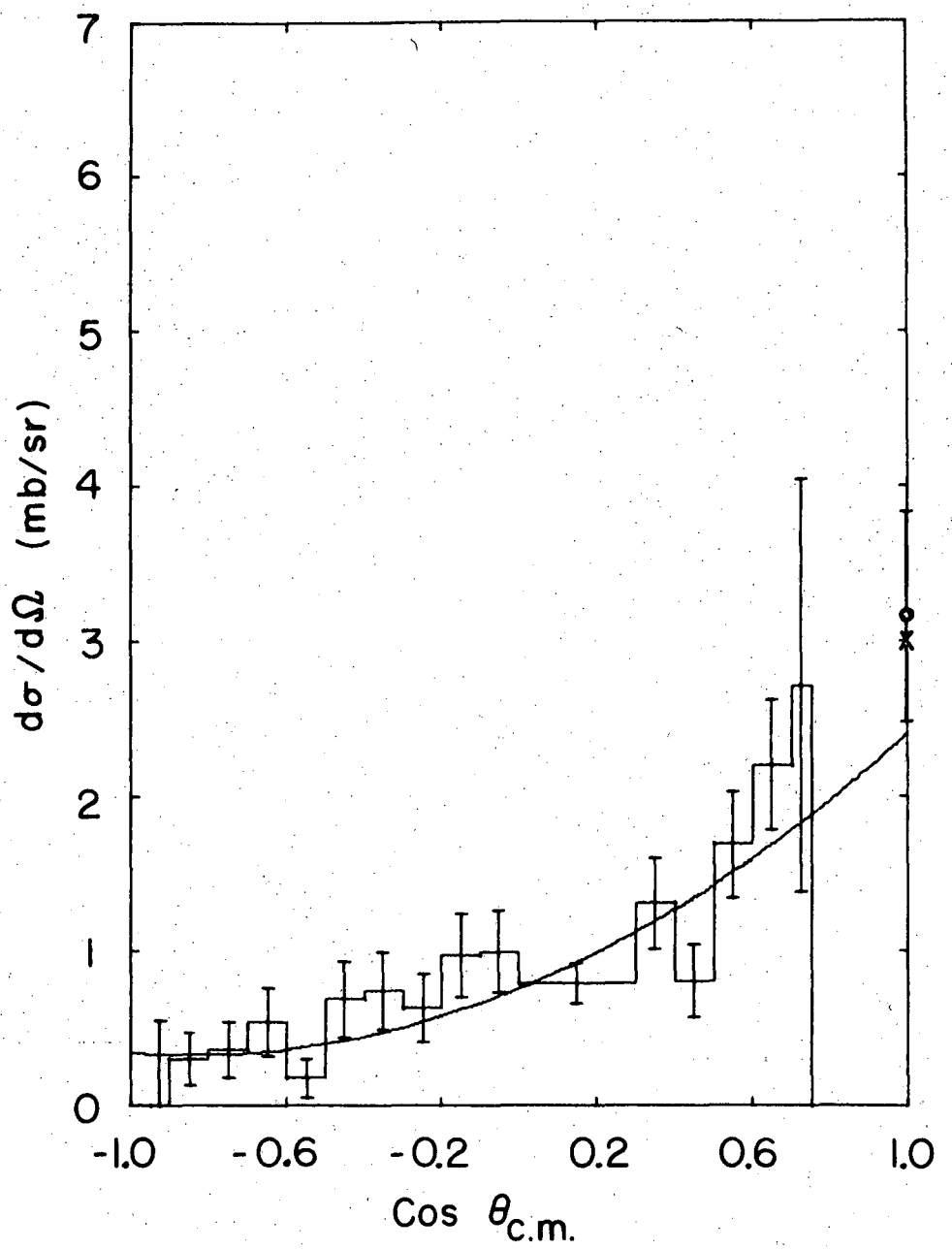

MU-36867

Fig. 17. Differential cross section for elastic K^--p scattering at $P_k = 660 \pm 20$ MeV/c. At $\cos\theta_{c.m.} = 1.0$, the optical theorem limit is indicated by x and the dispersion-relation point by o.

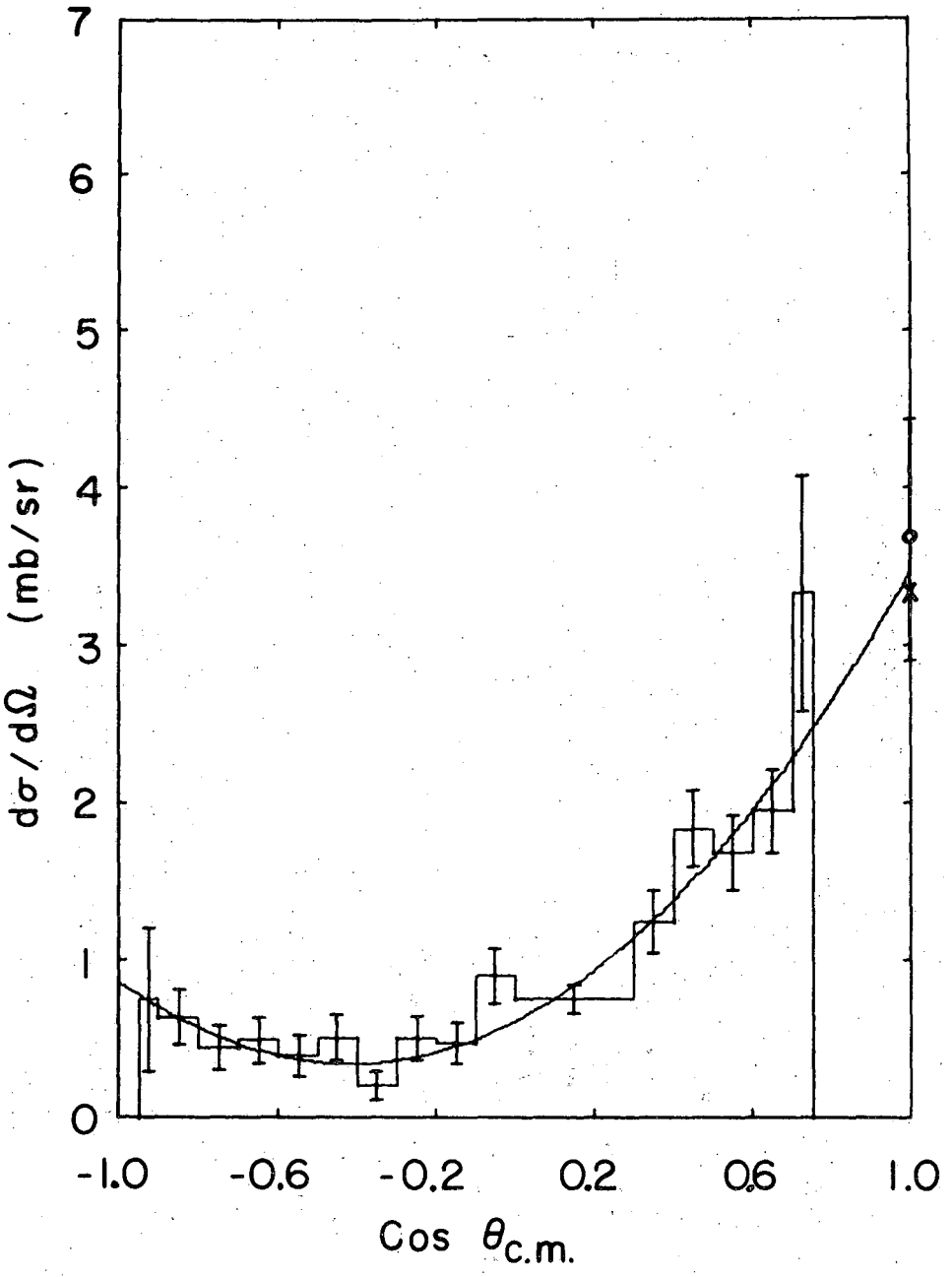

MU-36868

Fig. 18. Differential cross section for elastic K^--p scattering at $P_k = 700 \pm 20$ MeV/c. At $\cos\theta_{c.m.} = 1.0$, the optical theorem limit is indicated by x and the dispersion-relation point by o.

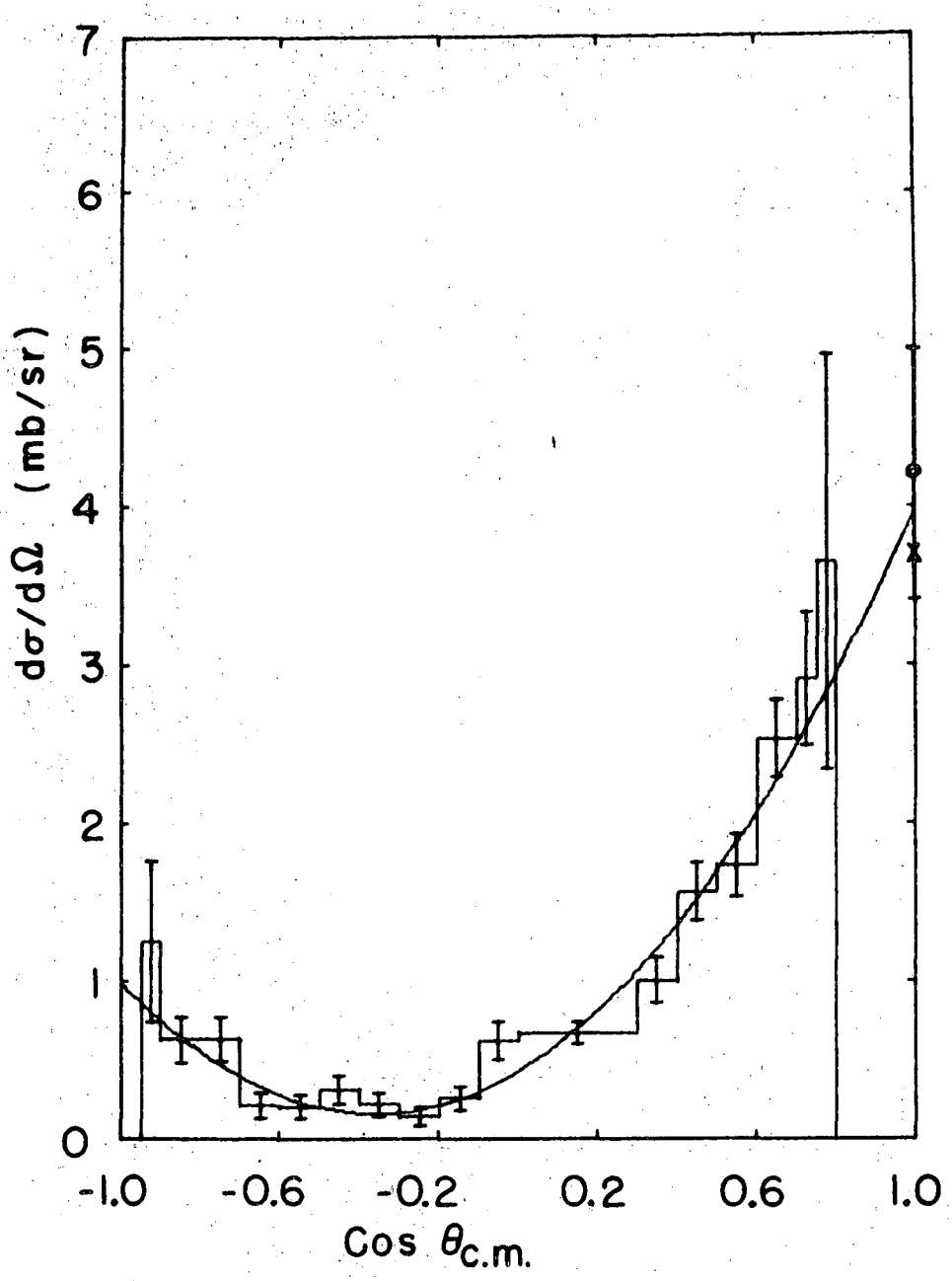

MU-36869

Fig. 19. Differential cross section for elastic K^--p scattering at $P_k = 740 \pm 20$ MeV/c. At $\cos \theta_{c.m.} = 1.0$, the optical theorem limit is indicated by x and the dispersion-relation point by o.

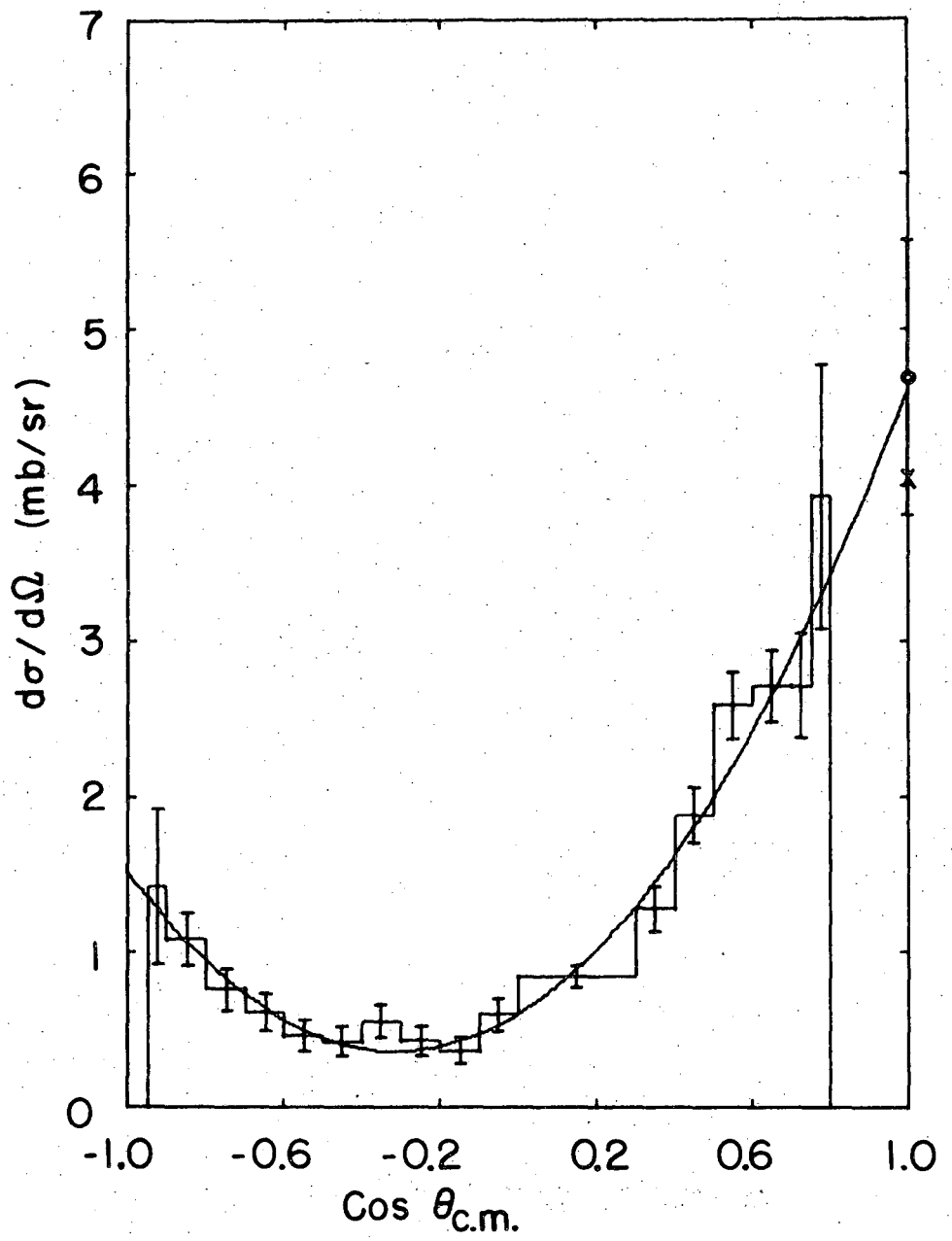

MU-36870

Fig. 20. Differential cross section for elastic K^--p scattering at $P_k = 780 \pm 20$ MeV/c. At $\cos\theta_{c.m.} = 1.0$, the optical theorem limit is indicated by x and the dispersion-relation point by o.

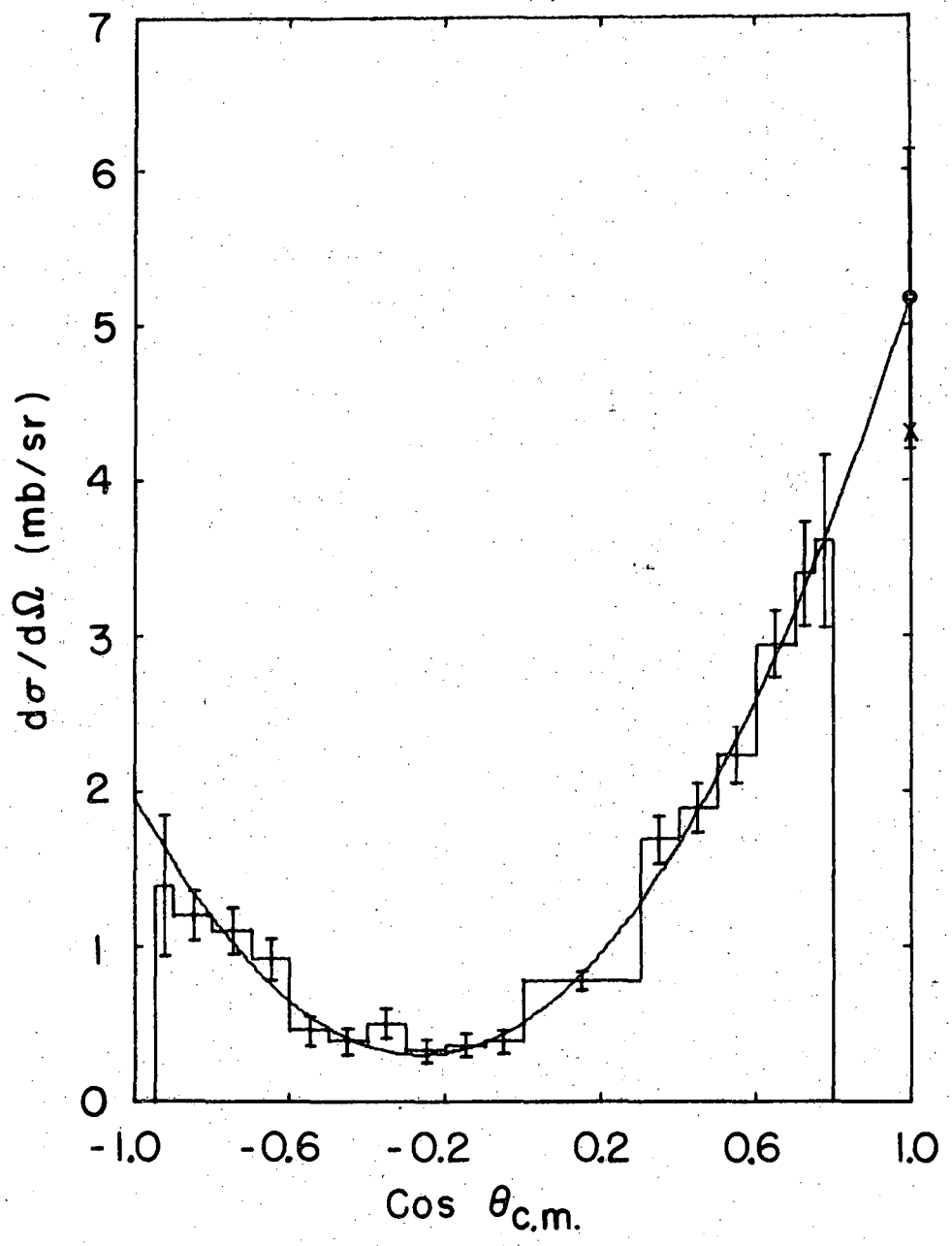

MU-36871

Fig. 21. Differential cross section for elastic K^--p scattering at $P_k = 820 \pm 20$ MeV/c. At $\cos\theta_{c.m.} = 1.0$, the optical theorem limit is indicated by x and the dispersion-relation point by o.

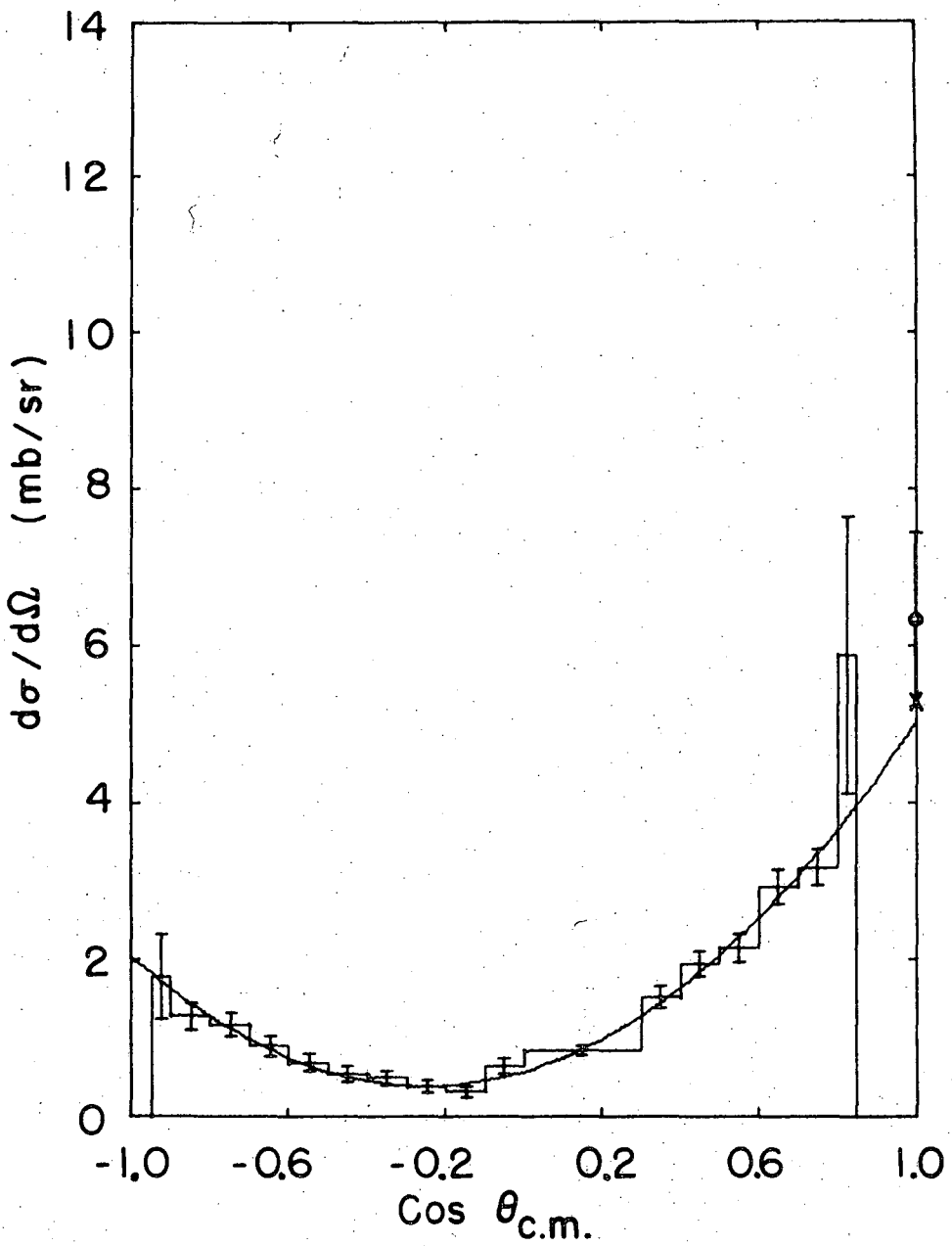

MU-36872

Fig. 22. Differential cross section for elastic K^--p scattering at $P_k = 860 \pm 20$ MeV/c. At $\cos\theta_{c.m.} = 1.0$, the optical theorem limit is indicated by x and the dispersion-relation point by o.

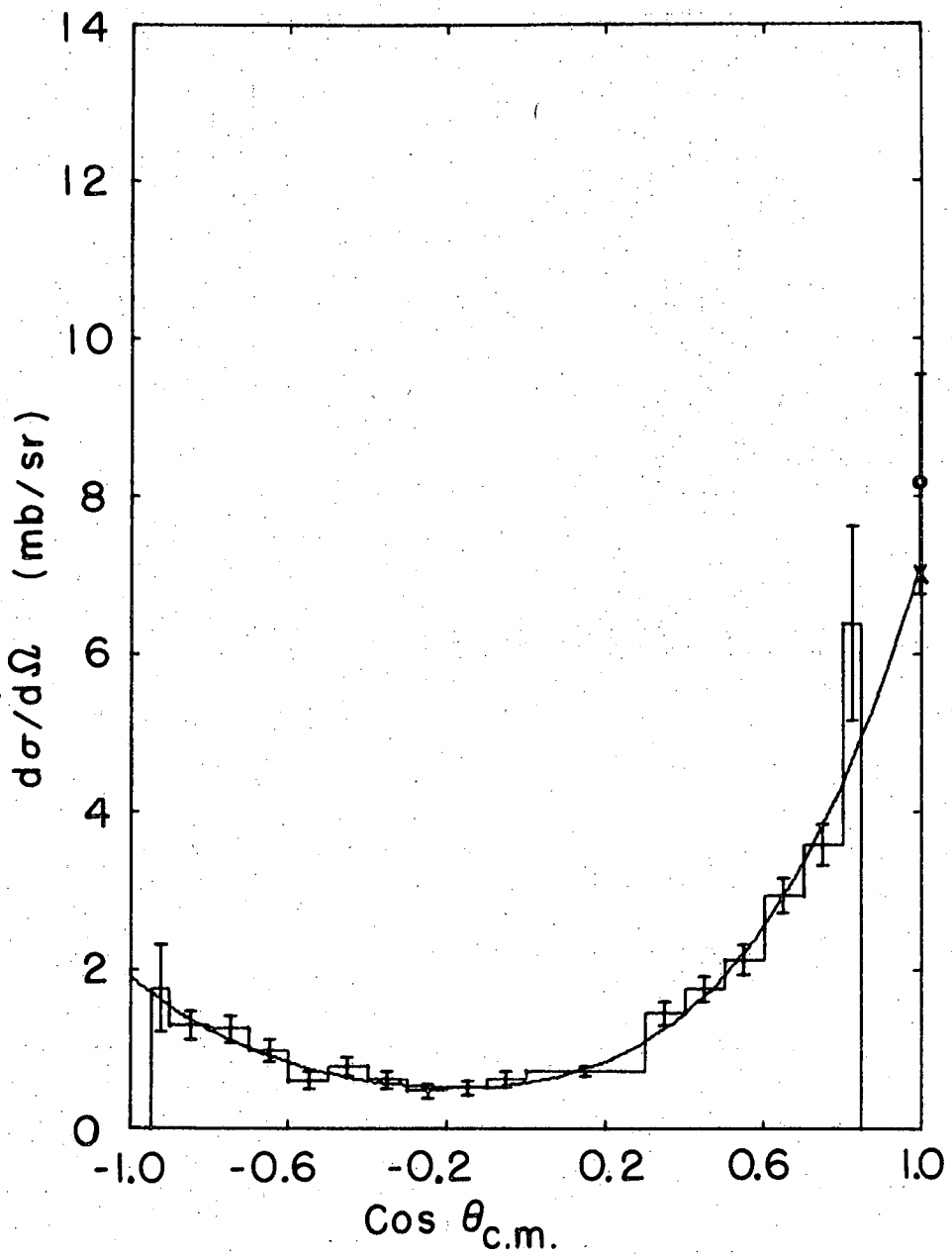

Fig. 23. Differential cross section for elastic K^--p scattering at $P_k = 900 \pm 20$ MeV/c. At $\cos\theta_{c.m.} = 1.0$, the optical theorem limit is indicated by x and the dispersion-relation point by o.

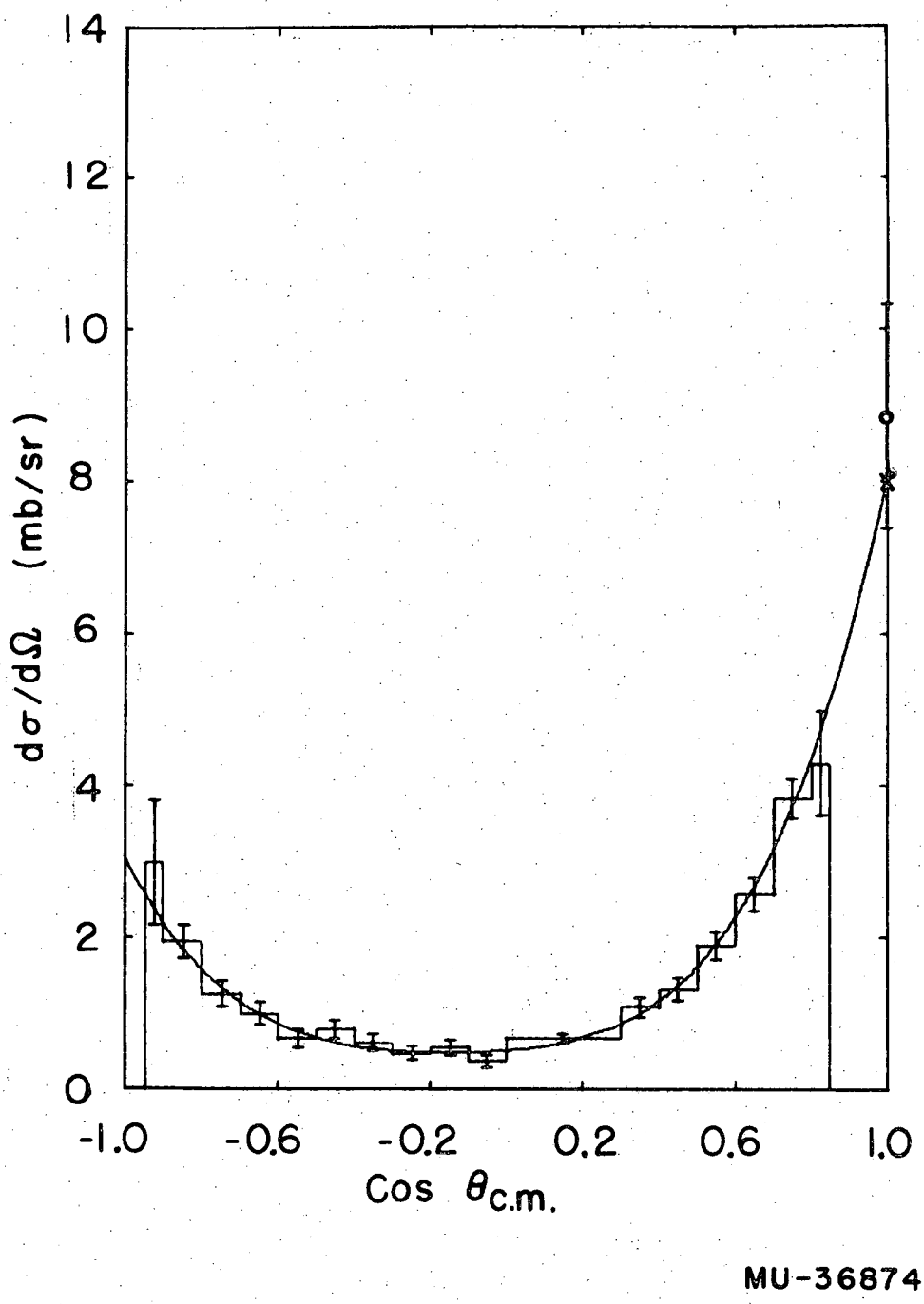

Fig. 24. Differential cross section for elastic K^--p scattering at $P_k = 940 \pm 20$ MeV/c. At $\cos\theta_{c.m.} = 1.0$, the optical theorem limit is indicated by x and the dispersion-relation point by o.

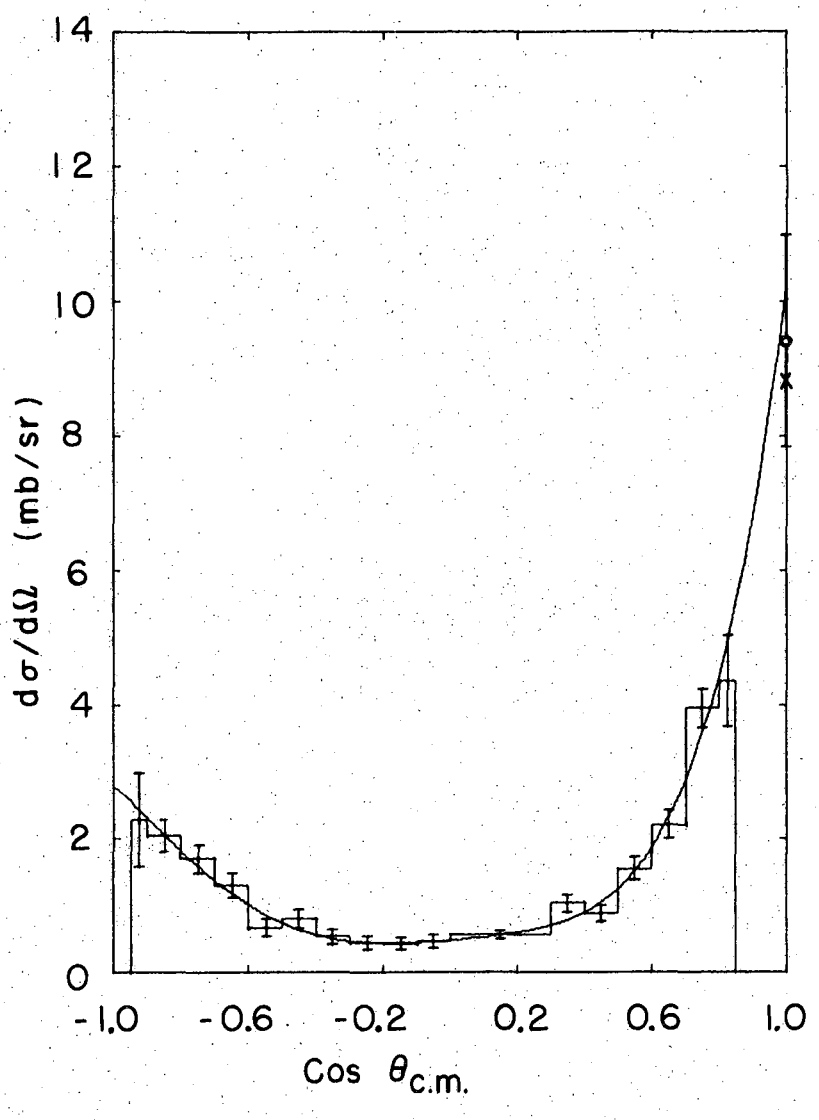

Fig. 25. Differential cross section for elastic K^--p scattering at $P_k = 980 \pm 20$ MeV/c. At $\cos\theta_{c.m.} = 1.0$, the optical theorem limit is indicated by x and the dispersion-relation point by o.

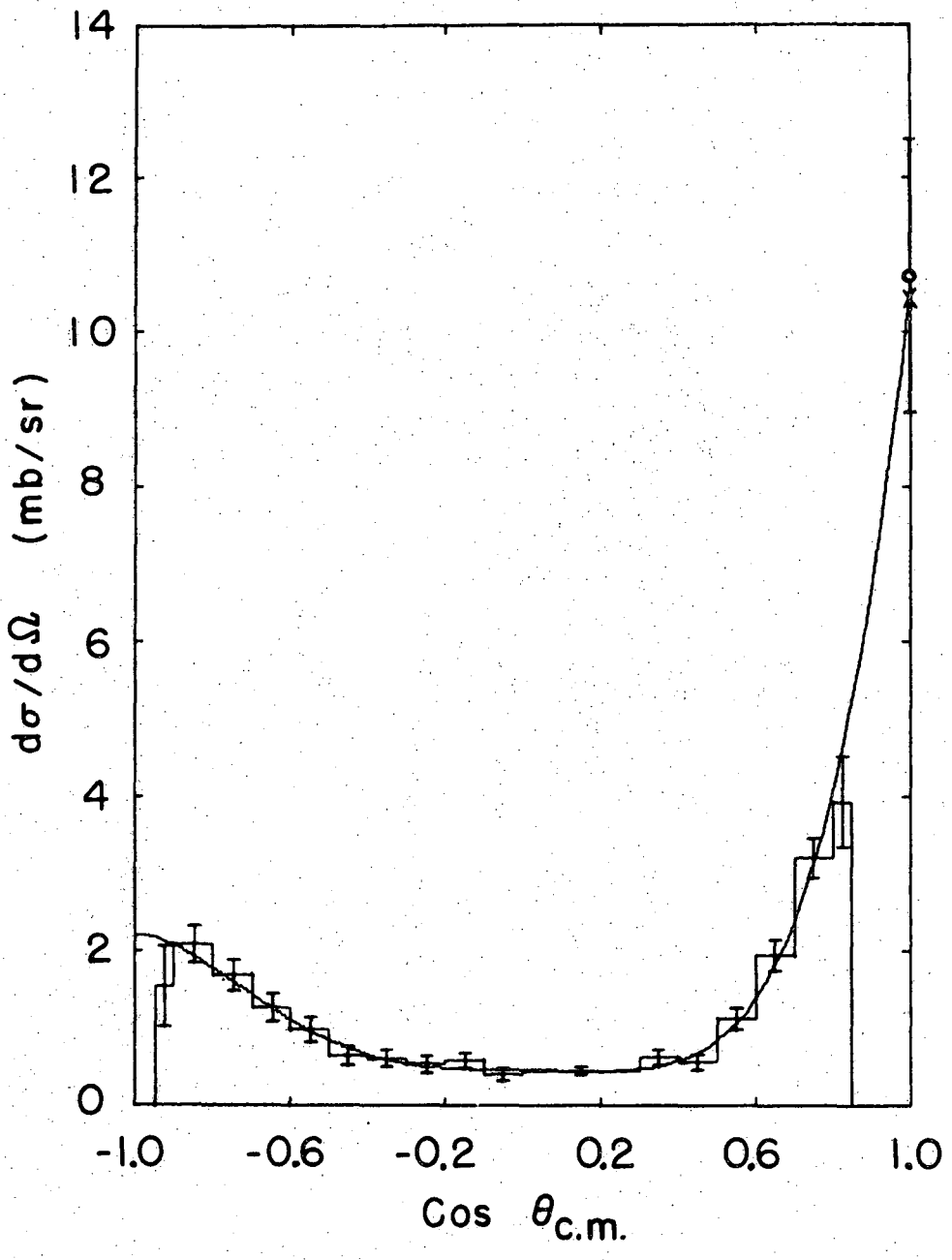

MU-36876

Fig. 26. Differential cross section for elastic K^--p scattering at $P_k = 1020 \pm 20$ MeV/c. At $\cos\theta_{c.m.} = 1.0$, the optical theorem limit is indicated by x and the dispersion-relation point by o.

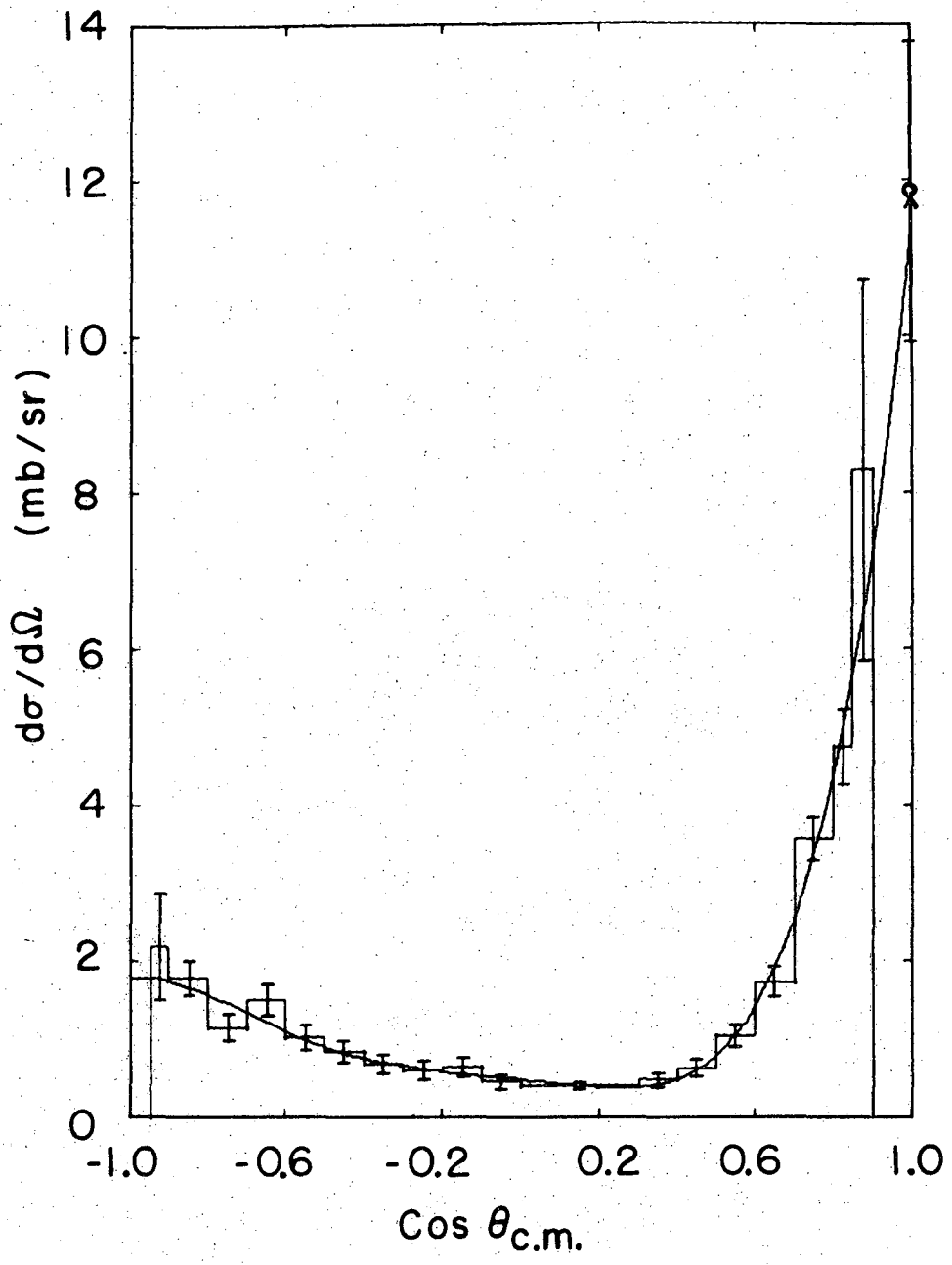

MU-36877

Fig. 27. Differential cross section for elastic K^--p scattering at $P_k = 1060 \pm 20$ MeV/c. At $\cos\theta_{c.m.} = 1.0$, the optical theorem limit is indicated by x and the dispersion-relation point by o.

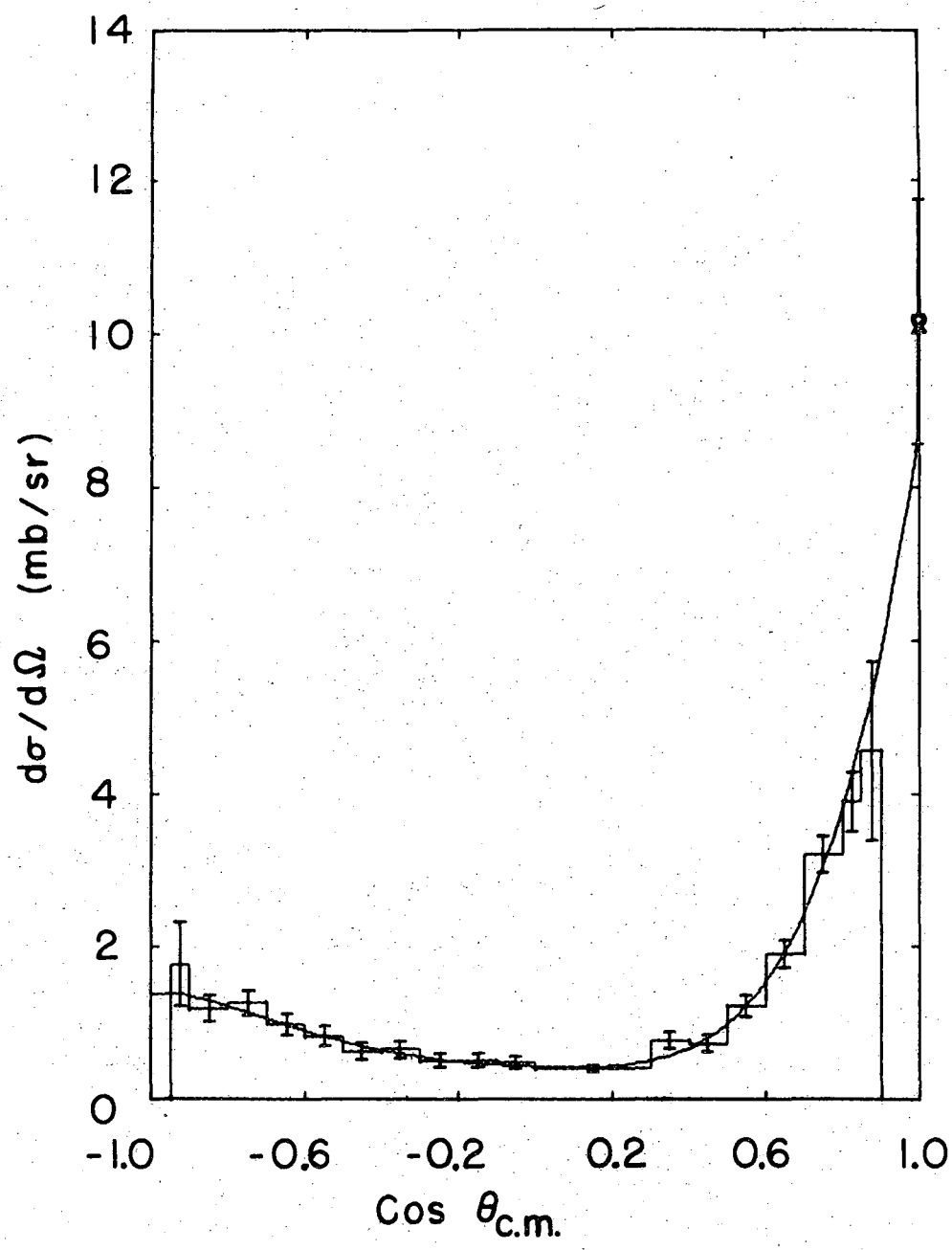

Fig. 28. Differential cross section for elastic K^--p scattering at $P_k = 1100 \pm 20$ MeV/c. At $\cos\theta_{c.m.} = 1.0$, the optical theorem limit is indicated by x and the dispersion-relation point by o.

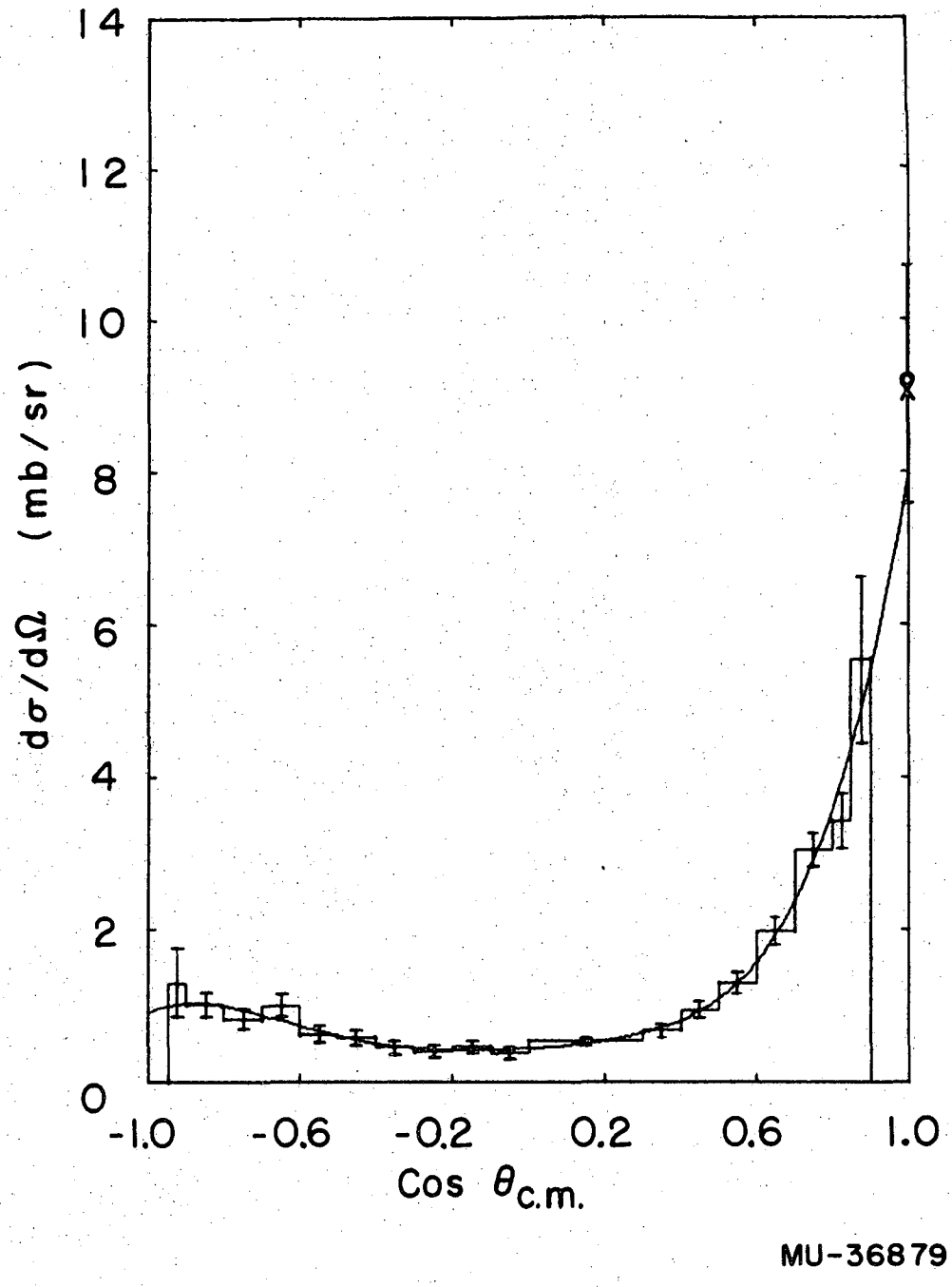

Fig. 29. Differential cross section for elastic K^--p scattering at $P_k = 1140 \pm 20$ MeV/c. At $\cos\theta_{c.m.} = 1.0$, the optical theorem limit is indicated by x and the dispersion-relation point by o.

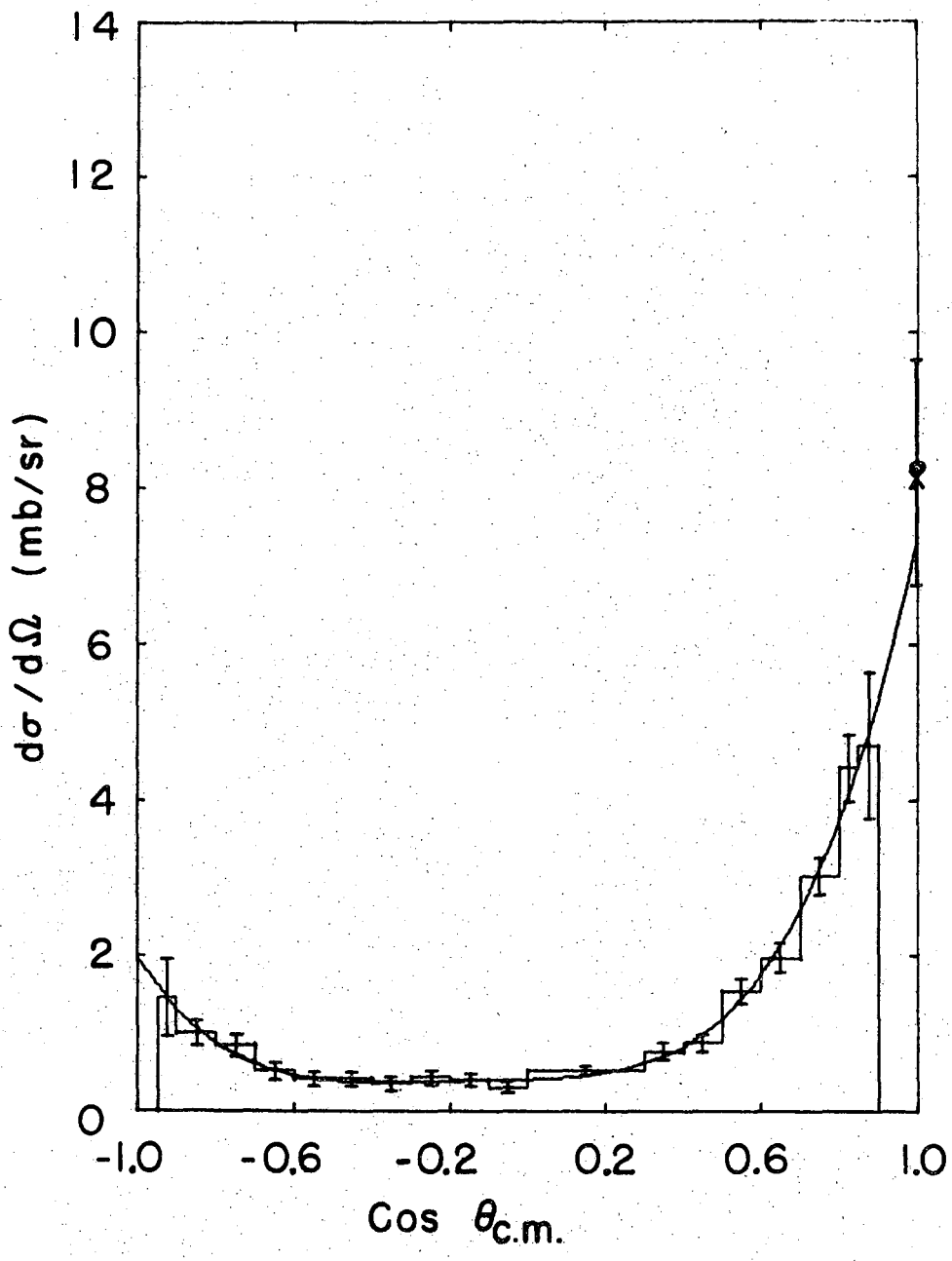

MU-36880

Fig. 30. Differential cross section for elastic K^--p scattering at $P_k = 1180 \pm 20$ MeV/c. At $\cos\theta_{c.m.} = 1.0$, the optical theorem limit is indicated by x and the dispersion-relation point by o.

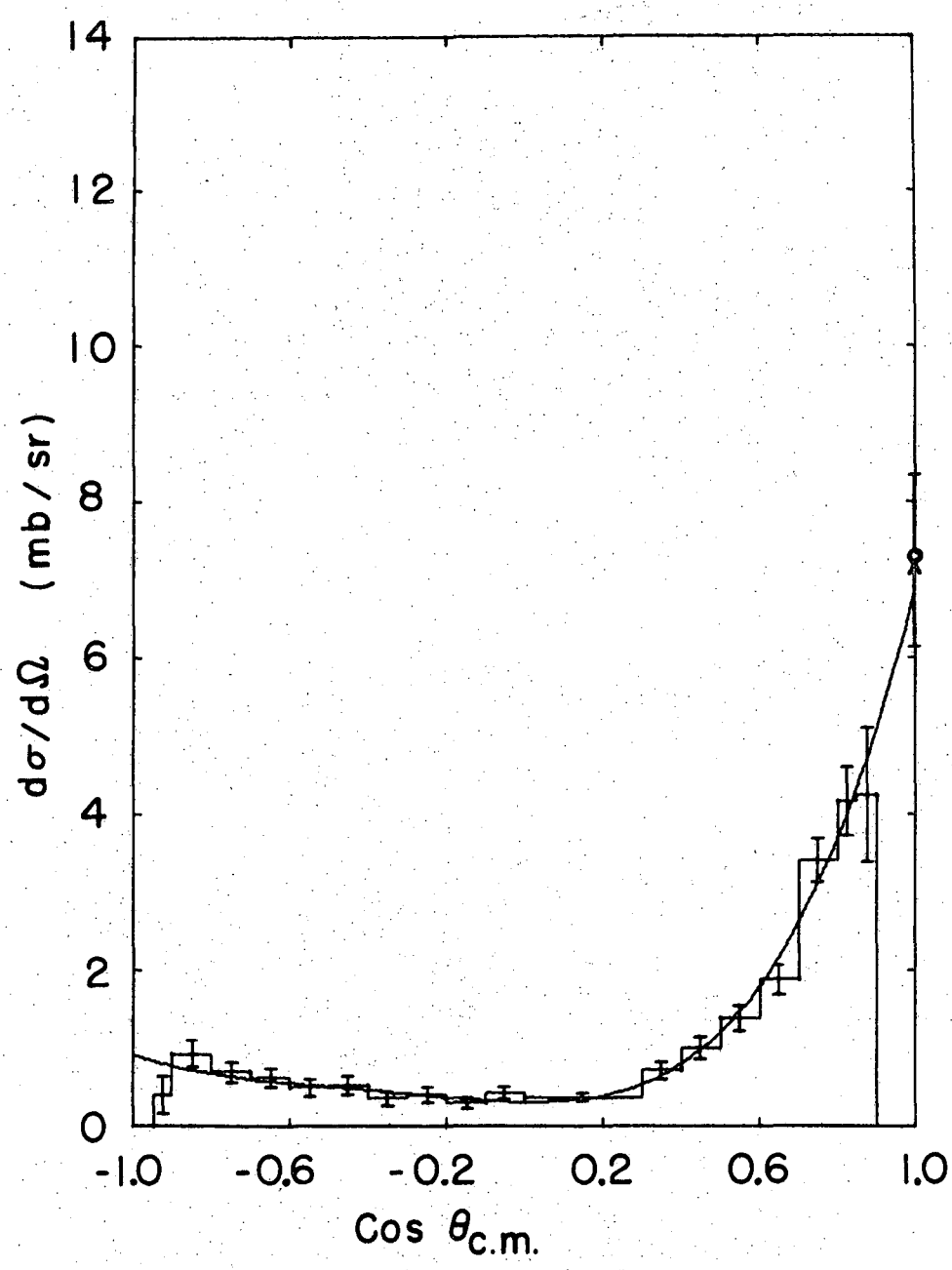

MU-36881

Fig. 31. Differential cross section for elastic K^--p scattering at $P_k = 1220 \pm 20$ MeV/c. At $\cos\theta_{c.m.} = 1.0$, the optical theorem limit is indicated by x and the dispersion-relation point by o.

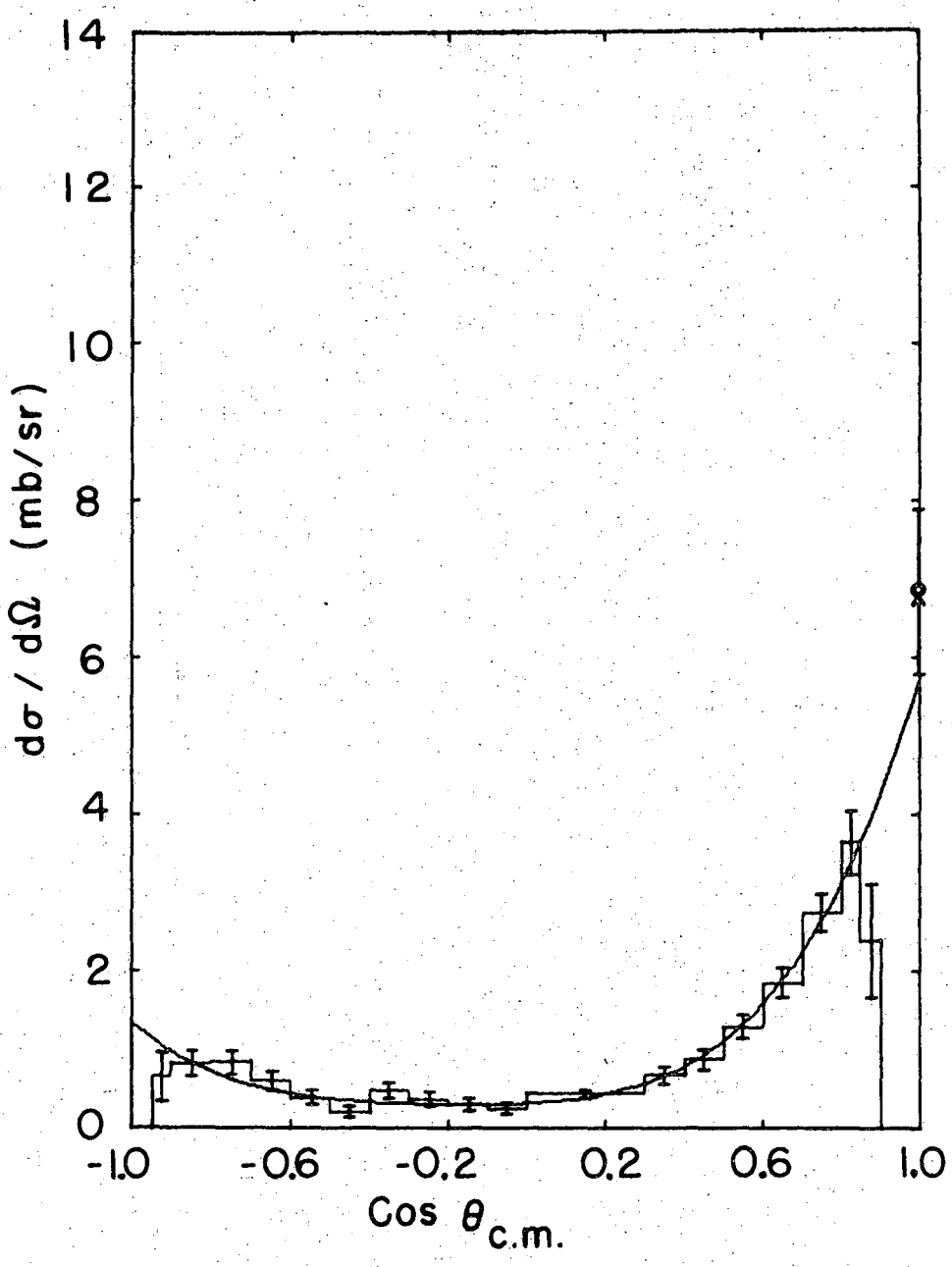

MU-36882

Fig. 32. Differential cross section for elastic K^--p scattering at $P_k = 1260 \pm 20$ MeV/c. At $\cos\theta_{c.m.} = 1.0$, the optical theorem limit is indicated by x and the dispersion-relation point by o.

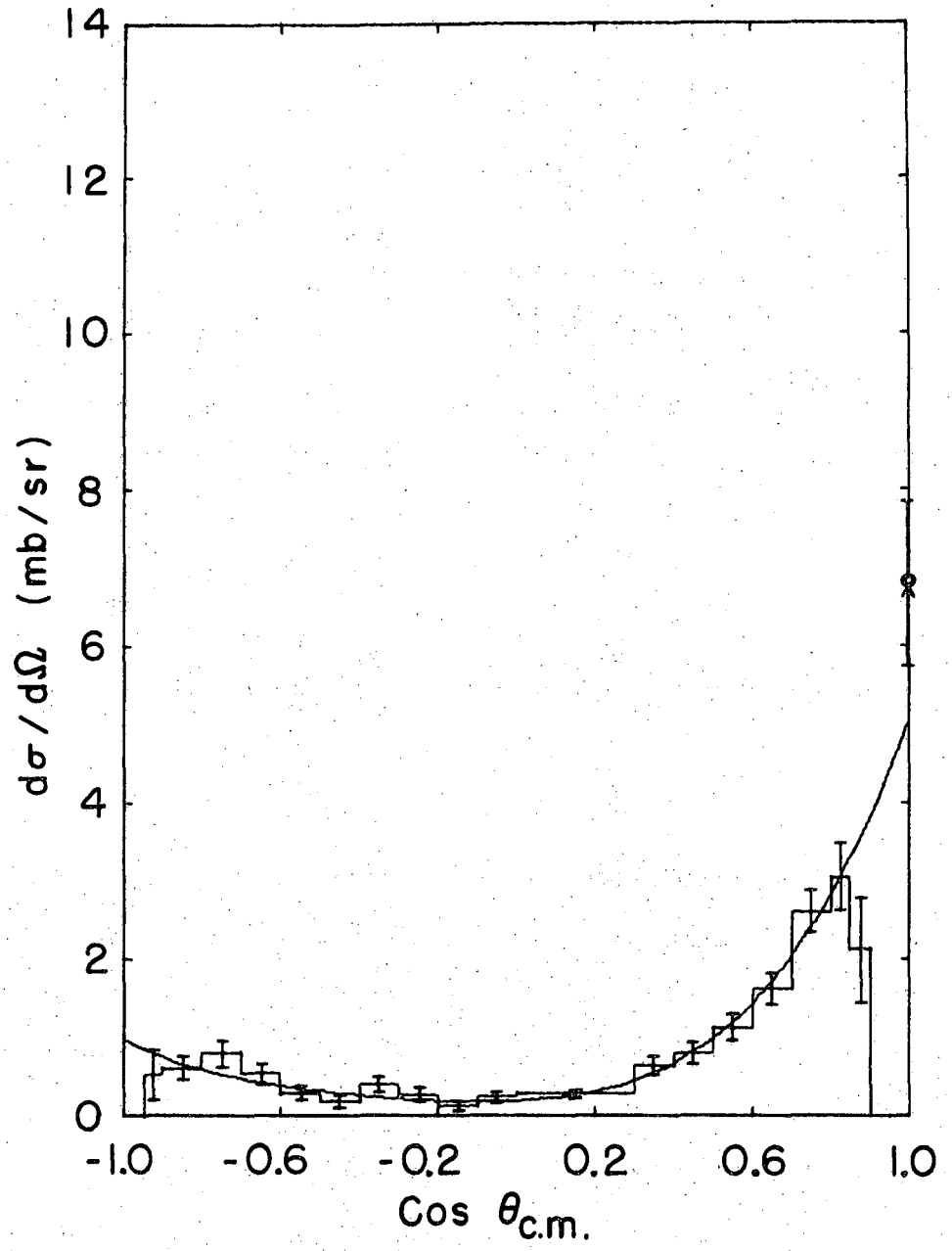

MU-36883

Fig. 33. Differential cross section for elastic K^--p scattering at $P_k = 1300 \pm 20$ MeV/c. At $\cos\theta_{c.m.} = 1.0$, the optical theorem limit is indicated by x and the dispersion-relation point by o.

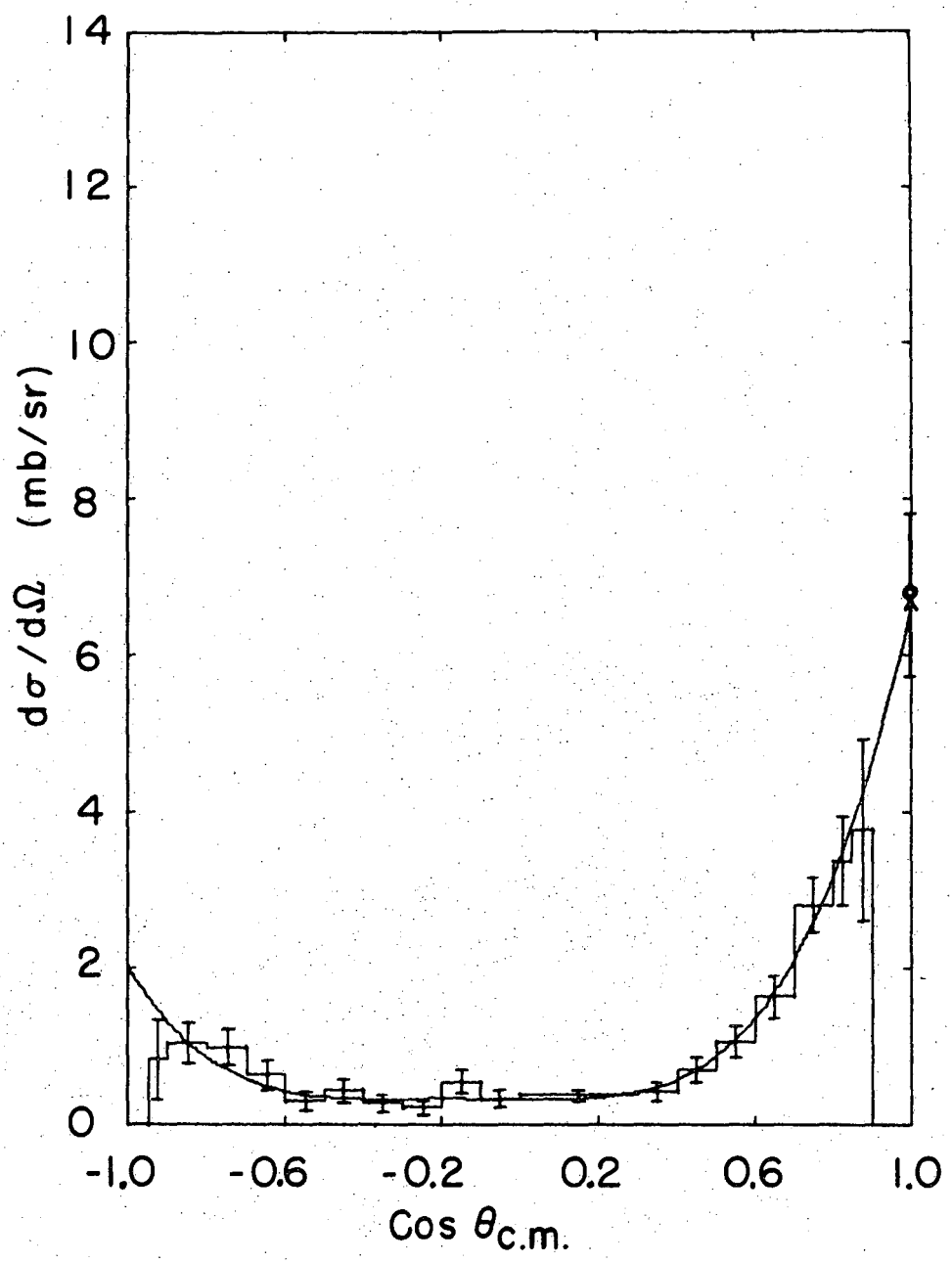

MU-36884

Fig. 34. Differential cross section for elastic K^--p scattering at $P_k = 1340 \pm 20$ MeV/c. At $\cos\theta_{c.m.} = 1.0$, the optical theorem limit is indicated by x and the dispersion-relation point by o.

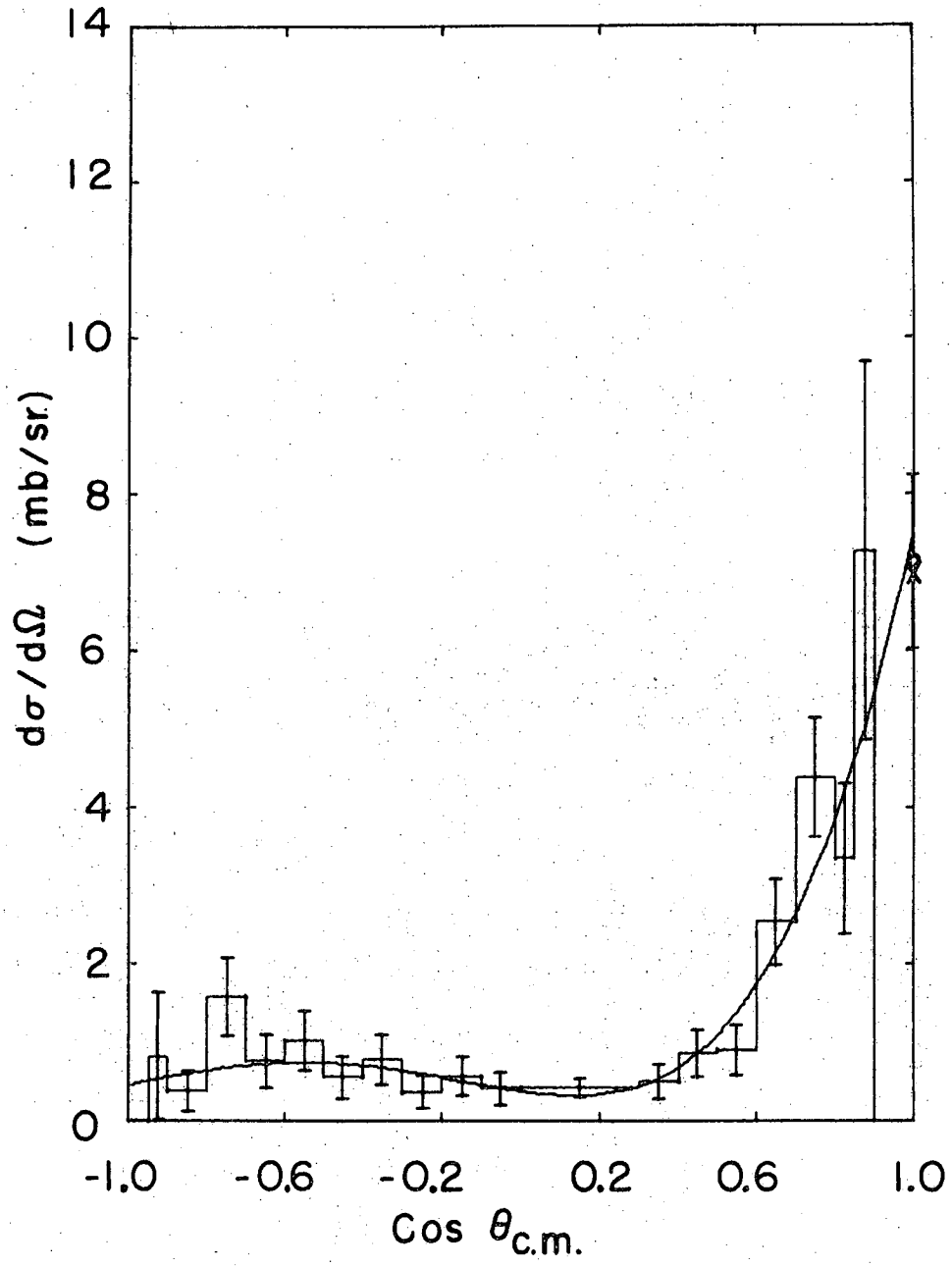

MU-36885

Fig. 35. Differential cross section for elastic K^--p scattering at $P_k = 1380 \pm 20$ MeV/c. At $\cos\theta_{c.m.} = 1.0$, the optical theorem limit is indicated by x and the dispersion-relation point by o.

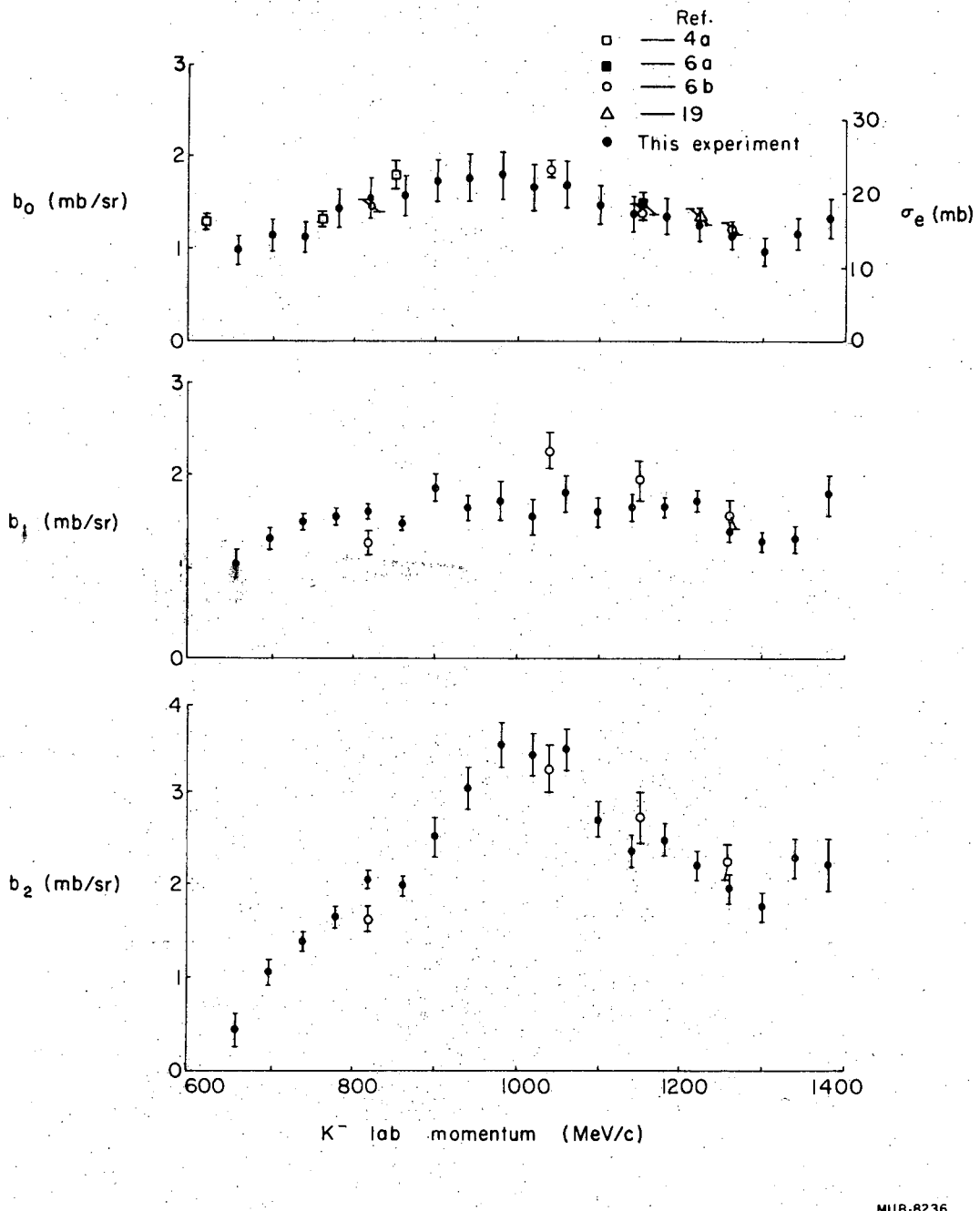

Fig. 36. Legendre-polynomial expansion coefficients b_0 (and $\sigma_e = 4\pi b_0$), b_1, and b_2 for the order fits underlined in Table XVI.

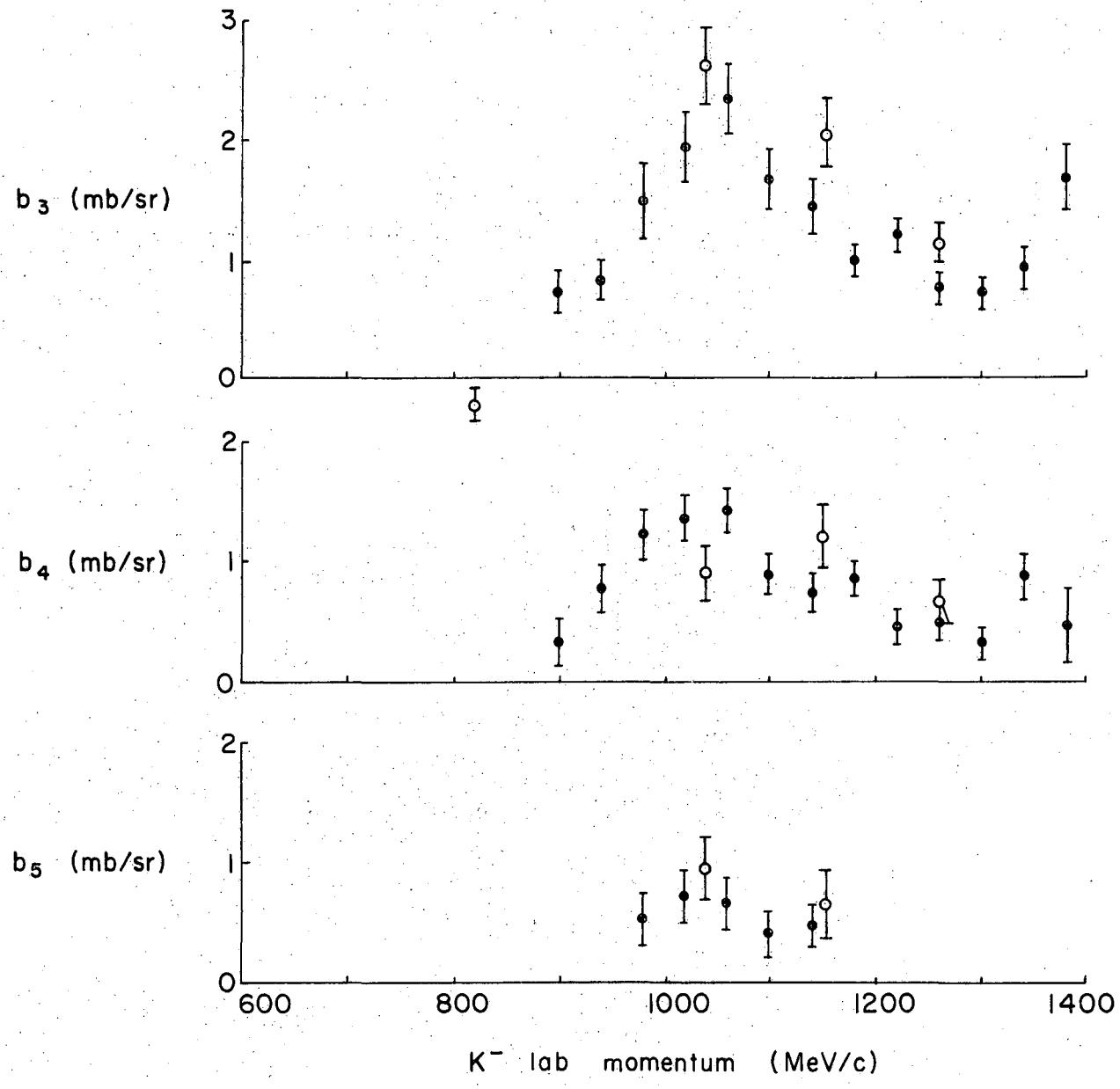

Fig. 37. Legendre-polynomial expansion coefficients b_3, b_4, and b_5 for the order fits underlined in Table XVI. The points indicated by o are from reference 6b.

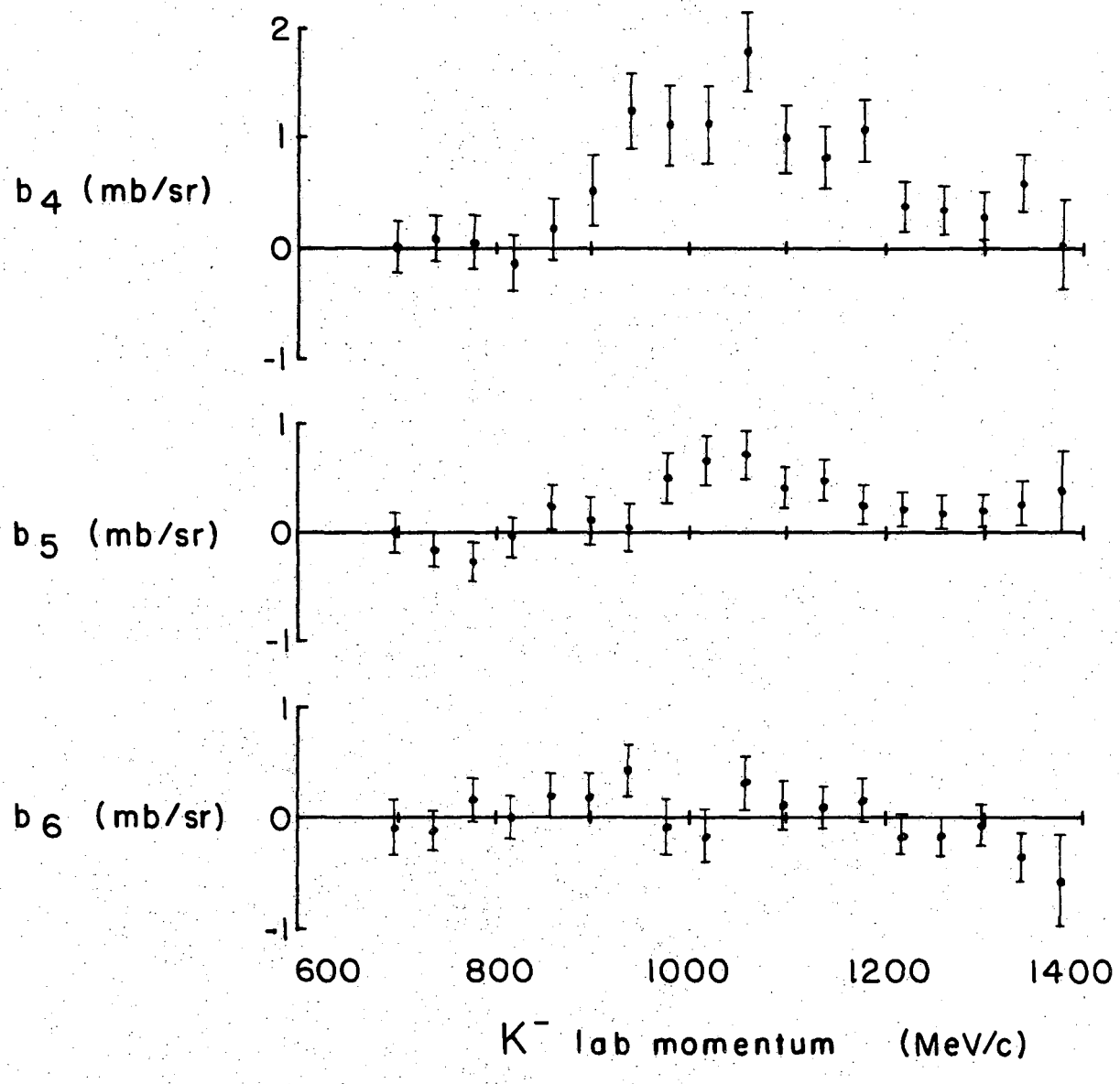

Fig. 38. Legendre-polynomial expansion coefficients b_4, b_5, and b_6 for sixth-order fits.

MUB-8240

V. DISCUSSION

A. Partial Waves

In order to discuss the physical significance of the data it is useful to parameterize the interaction in some way. The most common method is to decompose the differential cross section into partial waves. One can write[20]

$$d\sigma/d\Omega = |f(\theta)|^2 + |g(\theta)|^2,$$

where the non-spin-flip amplitude is given by

$$f(\theta) = \sum_{L=0}^{\infty} \left[(L+1)\, A_{L+} + L A_{L-} \right] P_L(\cos\theta), \qquad (2)$$

and the spin-flip amplitude by

$$g(\theta) = \sum_{L=0}^{\infty} (A_{L+} - A_{L-})\, P_L^1(\cos\theta). \qquad (3)$$

The functions P_L and P_L^1 are, respectively, the Legendre polynomial and first associated Legendre polynomial of order L, and θ is the kaon scattering angle in the c.m. system. The complex partial-wave amplitudes, $A_{L\pm}$, correspond to scattering in states of orbital angular momentum L and total angular momentum $L \pm 1/2$. These amplitudes can be written as

$$A_{L\pm} = \frac{\eta_{L\pm} \exp(2i\,\delta_{L\pm}) - 1}{2i\,k},$$

where $\eta_{L\pm}$ is the (real) absorption parameter ($0 \leq \eta_{L\pm} \leq 1$), $\delta_{L\pm}$ is the real part of the elastic-scattering phase shift, and k is the c.m. wave number. In the more common spectroscopic notation, states of $L = 0, 1, 2, 3 \cdots$ are represented by S, P, D, F... with the total angular momentum J as subscript. For example the state with $L = 3$ and $J = 5/2$ (A_{3-}) corresponds to $F_{5/2}$.

If L_{max} is assumed to be the largest value of orbital angular momentum involved in the interaction, we can cut off the summations in Eqs. (2) and (3) at L_{max} and rearrange the expression to yield

$$\frac{d\sigma}{d\Omega} = \sum_{0}^{2L_{max}} b_n P_n(\cos\theta),$$

where

$$b_n = \sum_{i \leq j}^{L_{max}} C_{ij}^{n} \, \mathrm{Re}(A_i^* A_j).$$

The coefficients C_{ij}^{n} for $L_{max} = 3$ (F waves) are given in Table XIX.

Unfortunately, at high energies and when inelastic channels are open, analysis of scattering in terms of partial waves becomes very complicated. In general, elastic-scattering data alone, in the presence of inelastic scattering, do not contain sufficient information to determine the elastic partial-wave amplitudes.[21] That is, assuming only waves to L_{max} are involved, we can determine $2L_{max} + 1$ real parameters (for example, the b_n) from the angular distribution. However, the interaction is described by two real parameters (η and δ) for each angular-momentum state ($A_{L\pm}$) for a total of $2(2L_{max} + 1)$ independent parameters. Thus $2L_{max} + 1$ additional numbers need to be determined in order to specify completely the partial-wave amplitudes. In principle, these parameters can be obtained from recoil-proton-polarization angular distributions (yielding $2L_{max}$ experimental parameters) and the total cross section (one parameter).

When isotopic spin is taken into account, the situation becomes even more complicated. In terms of $T = 0$ and $T = 1$ amplitudes (indicated by an additional subscript) the K^--p elastic amplitudes may be written

$$A_{L\pm}(K^- p \to K^- p) = 1/2(A_{0L\pm} + A_{1L\pm}). \qquad (4)$$

Table XIX. Coefficients C^n_{ij} for decomposition of Legendre polynomial expansion coefficients, b_n, in terms of partial-wave amplitudes A_i:

$$\frac{d\sigma}{d\Omega} = \sum_{0}^{N} b_n P_n(\cos\theta), \quad b_n = \sum_{i \le j} C^n_{ij} \, \mathrm{Re}\,(A_i^* A_j) .$$

$A_i^* A_j$	n = 0	1	2	3	4	5	6
$S^*_{1/2} S_{1/2} + P^*_{1/2} P_{1/2}$	1						
$S^*_{1/2} P_{1/2}$		2					
$S^*_{1/2} P_{3/2} + P^*_{1/2} D_{3/2}$		4					
$S^*_{1/2} D_{3/2} + P^*_{1/2} P_{3/2}$			4				
$S^*_{1/2} D_{5/2} + P^*_{1/2} F_{5/2}$			6				
$S^*_{1/2} F_{5/2} + P^*_{1/2} D_{5/2}$				6			
$S^*_{1/2} F_{7/2} + P^*_{1/2} G_{7/2}$				8			
$S^*_{1/2} G_{7/2} + P^*_{1/2} F_{7/2}$					8		
$P^*_{3/2} P_{3/2} + D^*_{3/2} D_{3/2}$	2		2				
$P^*_{3/2} D_{3/2}$		4/5		36/5			
$P^*_{3/2} D_{5/2} + D^*_{3/2} F_{5/2}$		36/5		24/5			
$P^*_{3/2} F_{5/2} + D^*_{3/2} D_{5/2}$			12/7		72/7		
$P^*_{3/2} F_{7/2} + D^*_{3/2} G_{7/2}$			72/7		40/7		
$P^*_{3/2} G_{7/2} + D^*_{3/2} F_{7/2}$				8/3		40/3	
$D^*_{5/2} D_{5/2} + F^*_{5/2} F_{5/2}$	3		24/7		18/7		
$D^*_{5/2} F_{5/2}$		18/35		16/5		100/7	
$D^*_{5/2} F_{7/2} + F^*_{5/2} G_{7/2}$		72/7		8		40/7	
$D^*_{5/2} G_{7/2} + F^*_{5/2} F_{7/2}$			8/7		360/77		200/11
$F^*_{7/2} F_{7/2} + G^*_{7/2} G_{7/2}$	4		100/21		324/77		100/33
$F^*_{7/2} G_{7/2}$		8/21		24/11		600/91	

The number of parameters needed to describe the interaction is doubled [equaling $4(2L_{max}+1)$] when isotopic spin is included. For example, with $L_{max} = 3$ (F waves), the number of independent parameters is 28, of which only seven are provided by elastic-scattering information. Additional experimental information such as charge-exchange angular distributions and polarization [$A_{L\pm}(K^- p \rightarrow \bar{K}^0 n) = 1/2(A_{0L\pm} - A_{1L\pm})$] and data from the pure $T = 1$ interaction, K^--neutron elastic scattering, is needed to determine completely the scattering amplitudes.

Thus it is not surprising that the major emphasis in analyzing scattering data has lately centered around attempts to correlate the world's supply of available data by using comprehensive phase-shift fitting programs and large digital computers. Of course, most of the effort has been expended in the analysis of N-N and π-N scattering data;[22, 12] however, at present there is considerable work in progress on a comprehensive phase-shift analysis of $\bar{K}$-N scattering.[23]

In view of the foregoing discussion it is clear that one can hope to do little more than make qualitative observations about the $\bar{K}$-N interaction from the elastic-scattering data of this experiment alone. Some insight may possibly be gained by observing the behavior of the total elastic cross sections and the Legendre-polynomial coefficients as a function of energy and checking the behavior of these quantities for consistency with the existence of various resonances suggested experimentally or predicted theoretically.

B. Total Elastic Cross Sections

We assume that resonances have the usual Breit-Wigner shape.[24] The resonant elastic amplitude is given by

$$k A_R = \frac{1/2\ \Gamma_e}{(E_R - E) - i\,\Gamma/2},$$

where Γ_e is the elastic width, Γ is the total width, E is the total energy in the c.m. system, and E_R is the resonant energy. In terms

of the elasticity $x = \Gamma_e/\Gamma$ and the convenient parameter $\epsilon = 2(E_R - E)/\Gamma$, the amplitude may be written

$$k A_R = \frac{x}{\epsilon - i}.$$

In general, Γ and Γ_e are energy-dependent. Nonrelativistic expressions for the energy dependence of Γ and Γ_e have been given[24] and depend on the interaction radius. Layson has given a modified resonance expression derived from a relativistic Schrödinger equation.[21] In Layson's expression, E is the total energy of the kaon in the c.m. system, and the widths Γ and Γ_e are slightly more complicated functions of energy. In our very rough treatment we use the more common resonance form where E is the total c.m. energy of the system. For simplicity we assume that the widths are constant.

For a resonance with total angular momentum J and in a single isotopic-spin state, we can write the resonance contributions to the K^--p total cross section (σ_t^{res}) and total elastic cross section (σ_e^{res}) as

$$\sigma_t^{res} = 2\pi\lambda^2 (J + 1/2) \frac{x}{\epsilon^2 + 1}$$

and

$$\sigma_e^{res} = \pi\lambda^2 (J + 1/2) \frac{x^2}{\epsilon^2 + 1},$$

where $\lambda = 1/k$ is the c.m. de Broglie wavelength.

In the above formulas, interference effects between the resonant amplitude and the background amplitude in the same partial-wave state have been ignored. It should be noted that even for a purely elastic resonance ($x = 1$), the total elastic resonant cross section furnishes only half the resonance contribution to the total cross section. This is, of course, due to the isotopic-spin composition of the K^--p elastic amplitude [Eq. (4)]. An equal contribution to the total cross section comes from the charge-exchange reaction $K^- p \to \bar{K}^0 n$.

The total cross section measurements (σ_t) of references 5a and 5b in the momentum region 750 to 1350 MeV/c and the total elastic cross sections (σ_e) obtained in this experiment have been fit (by a least-squares method) to expressions of the form

$$\sigma_t = \sigma_t^{nr} + \Sigma\, \sigma_t^{res}$$

and

$$\sigma_e = \sigma_e^{nr} + \Sigma\, \sigma_e^{res} .$$

Here σ_t^{nr} and σ_e^{nr} are background cross sections (assumed constant over the region fitted), and the $\Sigma\, \sigma_{t,\,e}^{res}$ correspond to sums of resonance terms. The results of this analysis for various combinations of suggested resonances are given in Table XX and plotted in Fig. 39.

Although the resonance parameters obtained from these fits should not be taken seriously, it is interesting to note that acceptable fits were obtained for all four combinations tried. However, it should be pointed out that the elasticities required for the $J = 3/2$ resonances are very high. In fact, the best fit for a single $J = 3/2$ resonance actually had $x \approx 1.2$. Fixing the elasticity parameter at 0.95 gave a 30% χ^2 probability as shown in the table, while lowering the elasticity to a more reasonable value of ~ 0.8 decreased the goodness of fit to less than 1%. The strength of this evidence against $J = 3/2$ is weakened, however, by the simplicity of the model used; in particular, the assumption that the background total cross sections are constant may not be valid.

C. Legendre-Polynomial Coefficients

As discussed in Section IV it appears that sixth-order coefficients are not needed to fit the data of this experiment. However, a plot of b_6 (Fig. 38) shows that the limit that can be placed on the magnitude of b_6 is not very good. Because of the large experimental errors, values (either slowly varying background or fluctuations

Table XX. Results of a least-squares fit of the following expressions to the experimental total and total elastic cross sections

$$\sigma_t = \sigma_t^{nr} + 2\pi\lambda^2 \sum_{\ell} (J_\ell + 1/2)\, X_\ell/(\epsilon_\ell^2 + 1)$$

and

$$\sigma_e = \sigma_e^{nr} + \pi\lambda^2 \sum_{\ell} (J_\ell + 1/2)\, X_\ell^2/(\epsilon_\ell^2 + 1)\,,$$

where

$$\epsilon = 2(E - ER)/\Gamma \quad \text{and} \quad X = \Gamma_e/\Gamma\,.$$

J	X	Γ (MeV)	ER (MeV)	σ_t^{nr} (mb)	σ_e^{nr} (mb)	Confidence level (%)
3/2	0.95[a]	109 ± 2	1808 ± 5	30.6 ± .6	13.3 ± 6	30
5/2	0.87 ± .13	154 ± 4	1815 ± 4	26.7 ± 1.0	11.7 ± 1.2	90
5/2	0.38 ± .16	74 ± 9	1768 ± 5	30.3 ± 4	14.0 ± .5	70
3/2	0.95 ± .10	72 ± 3	1825 ± 3			
5/2	0.21 ± .19	43 ± 9	1750 ± 7	29.3 ± .7	13.7 ± .6	80
5/2	0.78 ± .05	101 ± 3	1818 ± 5			

[a] This elasticity parameter, X, was held fixed at the given value rather than being searched by the fitting program.

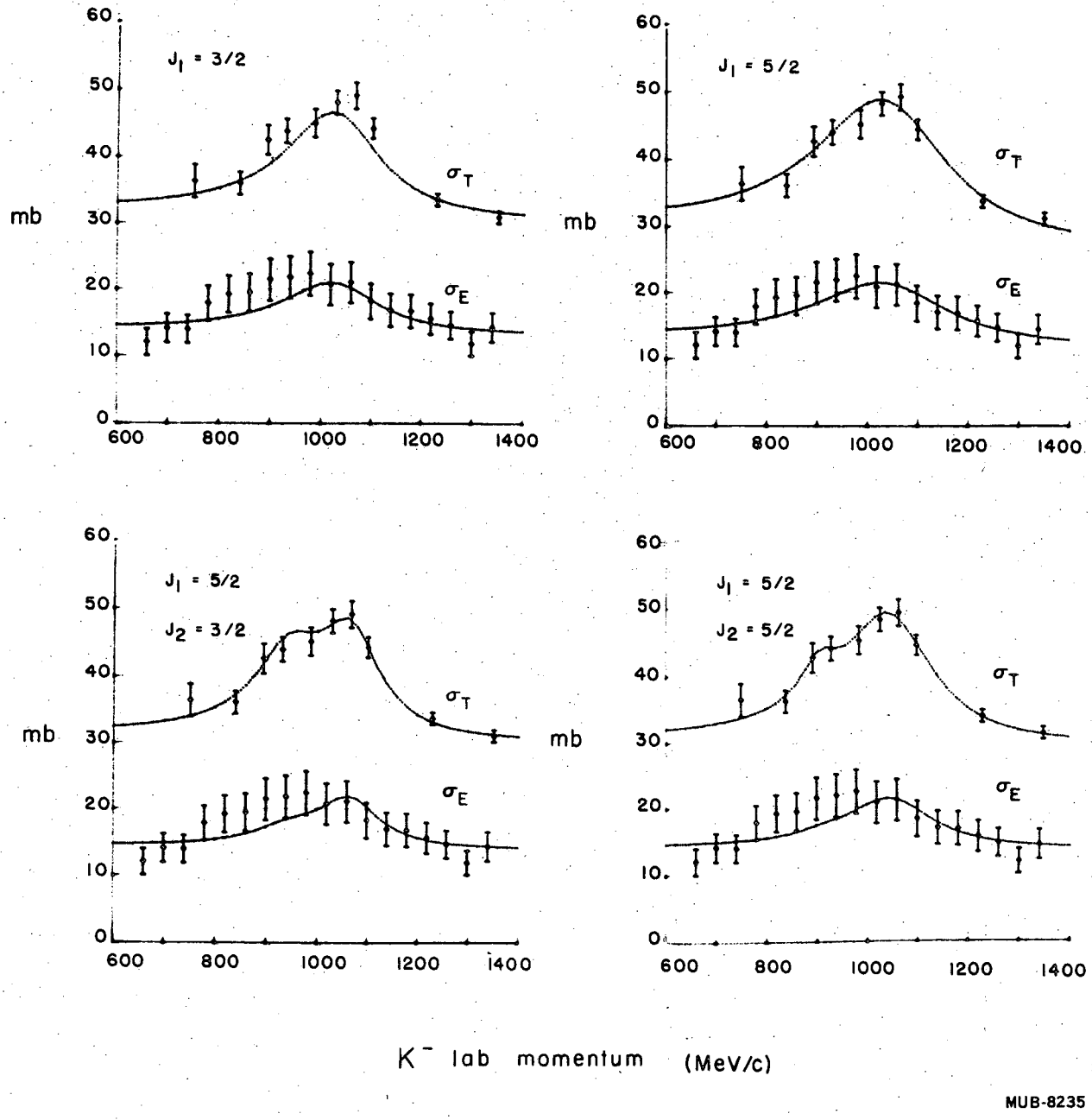

Fig. 39. Plots of the least-squares fits to the total and total elastic cross sections for the four combinations of resonance terms given in Table XX.

indicating structure) of a few tenths of a millibarn would not appear significant.

On the other hand, the fifth-order coefficient has an appreciable bump, of the order of 0.7 mb, in the resonance region. This indicates that the resonance (or resonances) is in one or more of the following states: $D_{3/2}$, $D_{5/2}$, $F_{5/2}$, or $F_{7/2}$. For simplicity we have neglected G waves (L = 4). The absence of a large bump in b_6 would seem to rule out $F_{7/2}$ as the resonant state.

If we assume for the moment that terms in b_5 involving $F_{7/2}$ can be neglected, we have left only the interference term between the $F_{5/2}$ and $D_{5/2}$ states, i.e., $b_5 \approx (100/7)\mathrm{Re}(D^*_{5/2} F_{5/2})$. In this case the large bump in b_5 would be consistent with a single resonance in either the $D_{5/2}$ or $F_{5/2}$ state interfering with a small nonresonant background amplitude in the other state. The bump could also be caused by the existence of two resonances, one in each partial-wave state, interfering with each other.

Note that if we relax the assumption $F_{7/2} = 0$ we can also "explain" the b_5 bump as arising from the interference between a $D_{3/2}$ resonant amplitude (as suggested by Ball and Frazer) and a small $F_{7/2}$ amplitude. If such a $D_{3/2}$ resonance were very highly elastic ($x \sim 0.9$) as is required to yield the total and total elastic cross-section enhancements, an $F_{7/2}$ amplitude of magnitude $|k F_{7/2}| \sim 0.07$ would be sufficient to produce the structure in b_5. Such a small $F_{7/2}$ term is certainly not excluded by the limit on the size of the b_6 coefficients obtained in this experiment. In fact it has recently been suggested[19, 25] that there is a resonance in the $F_{7/2}$ $T = 0$ amplitude at a c.m. energy of 2065 MeV with a width of approximately 180 MeV. This broad resonance, if it exists, could furnish practically all the $F_{7/2}$ amplitude needed to produce the b_5 enhancement at 1815 MeV.

Measurements of the angular distributions of the elastic charge-exchange reaction, $K^- + p \to \bar{K}^0 + n$, in the momentum region near 1000 MeV/c have been reported by several groups.[9, 25, 26] Expansions of the charge-exchange differential cross sections in Legendre-

polynomial series yield negative b_5 coefficients and a large positive bump in the b_4 coefficients peaked near 1050 MeV/c.

This behavior (and that of the corresponding elastic-scattering coefficients) is consistent with resonances in the $D_{5/2}$ and $F_{5/2}$ states. The fact that the enhancement in the b_5 coefficients for elastic and charge-exchange scattering are of opposite sign indicates that the interfering amplitudes responsible for the enhancements are in different isotopic spin states.[6]

On the other hand, if the $Y_0^*(1815)$ were $D_{3/2}$, the large positive b_4 coefficients in both the elastic and charge-exchange channels [coming, presumably, from the interference term $72/7\ \mathrm{Re}(D^*_{3/2}\ D_{5/2})$] would imply that the $D_{5/2}$ amplitude is predominantly in the $T=0$ state. In such case, the $Y_1^*(1765)$, if it exists and has $J=5/2$, would have to be in an $F_{5/2}$ angular-momentum state. An $F_{5/2}$ resonance at 1765 MeV would then imply a bump in the elastic b_1 coefficient due to the term $36/5\ \mathrm{Re}(D^*_{3/2}\ F_{5/2})$; however, the b_1 coefficients obtained in the experiment do not show indications of significant structure near 1000 MeV/c. This evidence against a $D_{3/2}\ Y_0^*(1815)$ is mitigated, however, by the fact that many terms contribute to b_1 (see Table XIX).

D. Conclusions

In summary, the elastic-scattering angular distributions measured in this experiment indicate the presence of a rather highly elastic resonance near 1815 MeV. The data are consistent with, but do not require, the existence of an additional enhancement near 1765 MeV. Evidence is presented against a $D_{3/2}$ assignment for the $Y_0^*(1815)$, but a $D_{3/2}$ resonance at 1815 MeV cannot be completely ruled out on the basis of our qualitative arguments.

ACKNOWLEDGMENTS

It is a pleasure to acknowledge the guidance and encouragement of Professor L. T. Kerth during the author's graduate career. Thanks are due Drs. Edgar F. Beall, Denis Keefe, John J. Thresher, C. L. Wang, and William A. Wenzel, who, along with Professor Kerth, participated in this experiment. The author has also benefitted greatly from association with Drs. Victor Cook and Bruce Cork.

The author is indebted to the many technicians who assisted with the setup and operation of the experiment and to the scanners for their careful and accurate scanning and measuring of the film. Special thanks are due Wilson Blake for invaluable assistance in data processing and computer programing. The cooperation of the Bevatron staff and operating crew, under the direction of Dr. Edward Lofgren, is gratefully acknowledged.

This work was done under the auspices of the U. S. Atomic Energy Commission.

APPENDIX

DERIVATION OF THE EXPRESSION FOR Z IN THE CYLINDRICAL CHAMBER

A diagram of a typical cylindrical-chamber track and its reflected image is shown in Fig. 40. The axis of rotation of one of the mirror segments is also indicated.

The optical system is such that only those light rays from a spark and those reflected from a mirror segment which are parallel to the cylindrical chamber axis are focused by the field lens onto the camera lens. An observer (camera) located at the focal point of the field lens sees a spark and its virtual image (located on the opposite side of the mirror) displaced in a direction normal to the axis of rotation of the mirror.

The relation between the height Z of the spark above the mirror and the displacement S of the image measured perpendicular to the mirror axis is particularly simple. From inspection of Fig. 40b (noting that the angle between the incident and reflected ray is 2θ), we have

$$S/Z = \tan 2\theta, \tag{5}$$

where θ is the tilt angle of the mirror about an axis normal to the paper in Fig. 40b.

In Fig. 40a, d is defined as the separation between the spark track and its image measured normal to the reflected track image, and β is the angle between the image and the mirror axis. Hence β is also the angle between d and S, and we see that

$$d = S \cos\beta . \tag{6}$$

Combining Eqs. (5) and (6) yields the desired expression

$$Z = \frac{d}{\cos\beta \tan 2\theta} . \tag{1}$$

Angle β depends on the location and direction of the track in the cylindrical chamber and is calculated in the geometrical reconstruction program for each measured track. For all possible

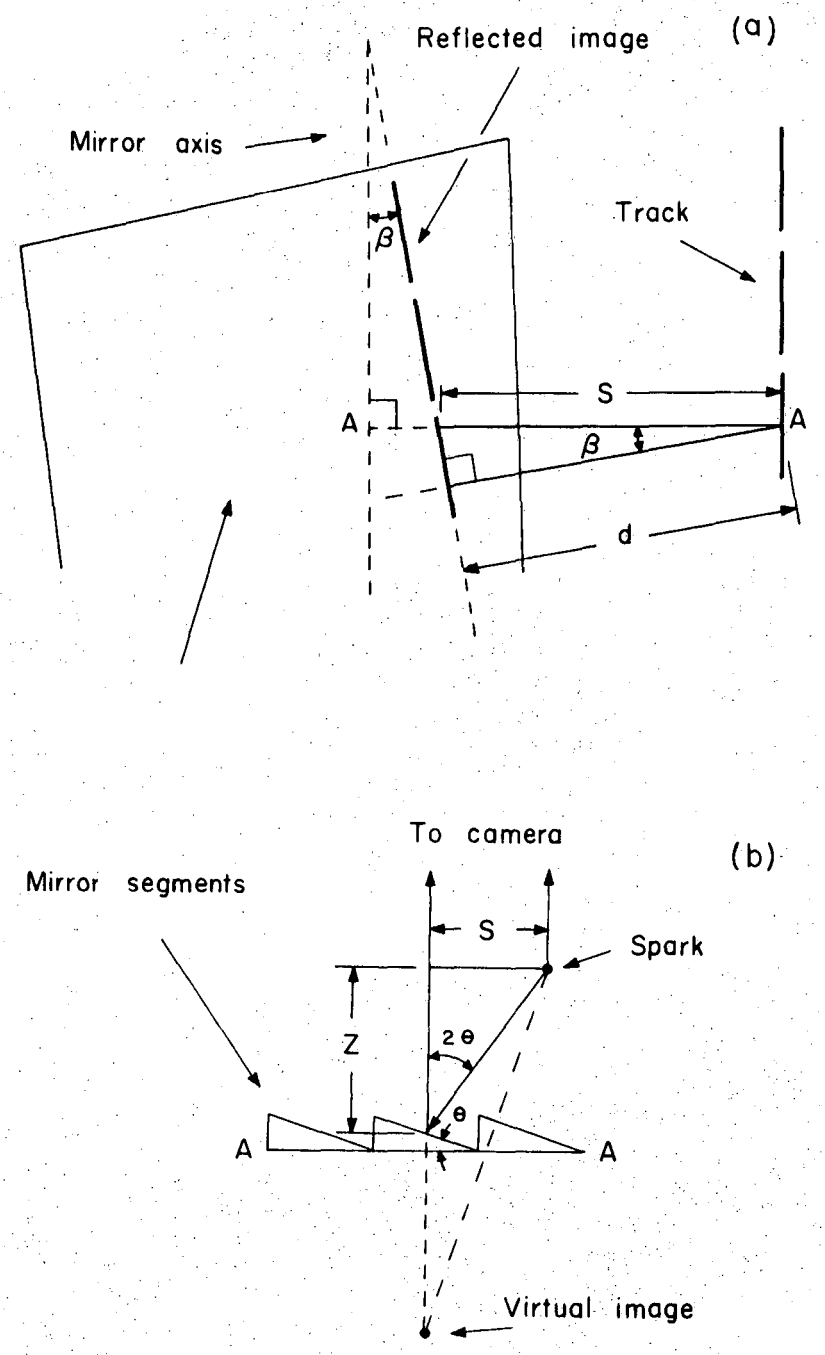

Fig. 40. Schematic diagrams of cylindrical chamber track and reflected image. (a) View of track and image as seen by camera. (b) Section AA of view (a). Note that scale is not the same for both diagrams.

orientations of tracks from elastic scatterings that originate in the hydrogen target, however, β is reasonably small ($\beta \lesssim 10$ deg), and therefore $\cos\beta$ approximately equals 1. Since $\tan 2\theta$ is approximately 0.2 ($\theta = 5.7$ deg), we have the approximate expression

$$Z \approx 5d.$$

The dip angle λ (angle between the track and the x-y plane) is given by an equation similar to Eq. (1),

$$\tan\lambda = \frac{\sin\alpha}{\cos\beta \tan 2\theta},$$

where α is the angle (in the x-y plane) between the track and its stereo image. For small dip angles we have

$$\lambda \approx 5\alpha,$$

Since the depth and dip angle calculations depend on the differences of <u>two</u> position and angle measurements, i.e., the track and its reflected image, errors in Z and λ include a factor of $\sqrt{2}$ in addition to the factor of five inherent in the small stereo angle. Thus uncertainties in Z and λ are approximately seven times as large as the corresponding uncertainties in the x-y plane.

REFERENCES

1. For a compilation of references of early total-cross-section measurements see, for example, T. F. Kycia, L. T. Kerth, and R. G. Baender, Phys. Rev. 118, 553 (1960).
2. (a) R. H. Dalitz and S. F. Tuan, Ann. Phys. 8, 100 (1959). See also:
   (b) R. H. Dalitz and S. F. Tuan, Ann. Phys. 10, 307 (1960).
   (c) W. E. Humphrey and R. R. Ross, Phys. Rev. 127, 1305 (1962).
3. M. B. Watson, M. Ferro-Luzzi, and R. D. Tripp, Phys. Rev. 131, 2248 (1963).
4. (a) P. Bastien and J. P. Berge, Phys. Rev. Letters 10, 188 (1963).
   (b) M. Taher-Zadeh, D. J. Prowse, P. E. Schlein, W. E. Slater, D. H. Stork, and H. K. Ticho, Phys. Rev. Letters 11, 470 (1963).
   (c) D. Berley, P. L. Connolly, E. L. Hart, D. C. Rahm, D. L. Stonehill, B. Thevenet, W. J. Willis, and S. S. Yamamoto, presented at the International Conference on High Energy Physics, Dubna (1964).
   (d) A. Leveque, M. Ville, P. J. Negus, W. M. Blair, A. L. Grant, I. S. Hughes, R. M. Turnbull, A. A. Z. Ahmad, S. Baker, L. Celnikier, S. Misbahuddin, I. O. Skillicorn, J. G. Loken, R. L. Sekulin, J. H. Mulvey, A. R. Atherton, G. B. Chadwick, W. T. Davies, J. H. Field, P. M. D. Gray, D. E. Lawrence, L. Lyons, A. Oxley, C. A. Wilkinson, C. M. Fisher, E. Pickup, L. K. Rangan, J. M. Scarr, and A. M. Segar, Physics Letters 18, 69 (1965).
5. (a) V. Cook, B. Cork, T. F. Hoang, D. Keefe, L. T. Kerth, W. A. Wenzel, and T. F. Zipf, Phys. Rev. 123, 320 (1961).
   (b) O. Chamberlain, K. M. Crowe, D. Keefe, L. T. Kerth, A. Lemonick, Tin Maung, and T. F. Zipf, Phys. Rev. 125, 1696 (1962).

6. (a) W. Graziano and S. G. Wojcicki, Phys. Rev. 128, 1868 (1962).
(b) L. Sodickson, I. Mannelli, D. Frisch, and M. Wahlig, Phys. Rev. 133, B757 (1964).
(c) E. F. Beall, W. R. Holley, D. Keefe, L. T. Kerth, J. J. Thresher, C. L. Wang, and W. A. Wenzel, in Proceedings of the International Conference on High Energy Physics, CERN, 1962 (CERN Scientific Information Service, Geneva 23, Switzerland), p. 368.
7. C. Wohl, M. H. Alston, G. R. Kalbfleisch, D. H. Miller, and S. G. Wojcicki, Bull. Am. Phys. Soc. 8, 340 (1963).
8. A. Barbaro-Galtieri, A. Hussain, and R. D. Tripp, Physics Letters 6, 296 (1963).
9. R. W. Birge, R. P. Ely, G. E. Kalmus, A. Kernan, J. Louie, J. S. Sahouria, and W. M. Smart, The Spin and Parity of the Y_0^* (1815) and the Y_1^* (1765), UCRL-16252, June 1965.
10. S. L. Glashow and A. Rosenfeld, Phys. Rev. Letters 10, 192 (1963).
11. J. S. Ball and W. R. Frazer, Phys. Rev. Letters 7, 204 (1961).
12. P. Auvil, C. Lovelace, A. Donnachie, and A. T. Lea, Physics Letters 12, 76 (1964).
13. E. F. Beall, W. Holley, D. Keefe, L. T. Kerth, J. J. Thresher, C. L. Wang, and W. A. Wenzel, Nucl. Instr. Methods 20, 205 (1963).
14. B. Cork, D. Keefe, and W. A. Wenzel, A Coincidence-Anticoincidence Gas Cerenkov Counter, in Proceedings of an International Conference on Instrumentation for High Energy Physics (Interscience Publishers, New York, 1960), p. 84.
15. Richard L. Crolius, A Measurement of the Polarization of Sigma-Zero Hyperons Produced by Pi-Minus Mesons on Hydrogen Near 1.3 BeV/c (Ph. D. Thesis), UCRL-16089, May 1965.

16. J. C. Hodges, D. Keefe, L. T. Kerth, J. J. Thresher, and W. A. Wenzel, Digitized Measuring Projector for the Analysis of Spark-Chamber Photographs, UCRL-10251, May 1962.

17. V. Cook, D. Keefe, L. T. Kerth, P. G. Murphy, W. A. Wenzel, and T. F. Zipf, Phys. Rev. 129, 2743 (1963).

18. J. Schwartz and P. Bastien, DJINN-A General Least Squares Analysis Program or Subroutine, Programmers' Memo P-58, Alvarez Physics Group, Lawrence Radiation Laboratory Report, May 1960 (unpublished).

19. John H. Munson, K^-p Elastic Scattering at 1.22 BeV/c (Ph. D. Thesis, Part II), UCRL-11155, December 1963.

20. J. Hamilton, The Theory of Elementary Particles (Oxford University Press, Amen House, London, 1959), p. 322.

21. William M. Layson, Nuovo Cimento 27, 724 (1963).

22. (a) G. Breit, M. H. Hull, Jr., K. E. Lassila, and K. D. Pyatt, Jr., Phys. Rev. 120, 2227 (1960).

(b) H. P. Stapp, H. P. Noyes, and M. J. Moravcsik, in Proceedings of the International Conference on High Energy Physics, CERN, 1962 (CERN Scientific Information Service, Geneva 23, Switzerland), p. 131.

(c) L. D. Roper, R. M. Wright, and B. T. Feld, Phys. Rev. 138, B190 (1965).

(d) M. H. Hull, Jr. and F. C. Lin, Phys. Rev. 139, B630 (1965).

(e) B. H. Bransden, P. J. O'Donnell, and R. G. Moorhouse, Physics Letters 11, 339 (1964).

23. (a) David S. Bailey, Bull. Am. Phys. Soc. II, 10, 736 (1965).

(b) C. L. Wang, E. F. Beall, W. R. Holley, D. Keefe, L. T. Kerth, J. J. Thresher, and W. A. Wenzel, Bull. Am. Phys. Soc. II, 10, 679 (1965).

(c) C. L. Wang, Recoil-Proton Polarization in Negative Kaon-Proton Elastic Scattering Between 700 and 1400 MeV/c Incident Kaon Momenta (Ph. D. Thesis), UCRL-11881, April 1965.

24. J. M. Blatt and V. F. Weisskopf, Theoretical Nuclear Physics (John Wiley and Sons, Inc., New York, 1952), Chap. VIII.

25. Charles G. Wohl, K^-p Charge-Exchange Scattering from 1200 to 1700 MeV/c (Ph. D. Thesis), UCRL-16288, July 1965.

26. (a) G. R. Charlton, P. E. Condon, R. P. Uhlig, M. C. Whatley, G. B. Yodh, A. H. Actken, R. G. Glasser, and A. J. Herz, Bull. Am. Phys. Soc. 9, 642 (1964).

(b) R. P. Ely, Jr., Bull. Am. Phys. Soc. 9, 703 (1964).

(c) R. L. Setti, R. Armenteros, M. Ferro-Luzzi, D. W. G. Leith, A. Minten, H. Schneider, R. D. Tripp, H. Filthuth, A. Fridman, E. Kluge, V. Hepp, R. Barloutaud, P. Grannet, J. Meyer, and J. P. Porte, Bull. Am. Phys. Soc. 9, 723 (1964).

(d) R. P. Uhlig, G. R. Charlton, P. E. Condon, M. C. Whatley, G. B. Yodh, A. H. Aitken, R. G. Glasser, and A. J. Herz, Bull. Am. Phys. Soc. 9, 723 (1964).